QUANTIFICATION OF BIOMOLECULE DYNAMICS AND INTERACTIONS IN LIVING ZEBRAFISH EMBRYOS BY FLUORESCENCE CORRELATION SPECTROSCOPY

SHI XIANKE

(B. Sc., USTC, P. R. CHINA)

A THESIS SUBMITTED

FOR THE DEGREE OF DOCTOR OF PHILOSOPHY

DEARTMENT OF CHEMISTRY

NATIONAL UNIVERSITY OF SINGAPORE

2009

This work is a result of collaboration between the Biophysical Fluorescence Laboratory at Department of Chemistry, National University of Singapore (NUS) and the Fish Development Biology Laboratory at Institute of Molecular and Cell Biology (IMCB), under the supervision of Associate Professor Thorsten Wohland (NUS) and Associate Professor Vladimir Korzh (IMCB), between July 2004 and November 2008.

The results have been partly published in:

Shi, X., Teo, L. S., Pan, X., Chong, S. W., Kraut, R., Korzh, V., & Wohland, T., 2009, Probing events with single molecule sensitivity in zebrafish and *Drosophila* embryos by fluorescence correlation spectroscopy, *Dev. Dyn.*, 238 (12), 3156-67

Shi, X., Foo, Y. H., Sudhaharan, T., Chong, S. W., Korzh, V., Ahmed, S., & Wohland, T., 2009, Determination of dissociation constants in living zebrafish embryos with single wavelength fluorescence cross-correlation spectroscopy, *Biophys. J.*, (97) 678-686

Shi. X., and Wohland, T., Fluorescence correlation spectroscopy, 2010, in *Nanoscopy and Multidimensional Fluorescence Microscopy*, edited by Diaspro, A., Taylor and Francis

Pan, X., Shi, X., Korzh, V., Yu, H., & Wohland, T., 2009, Line scan fluorescence correlation spectroscopy for 3D microfluidic flow velocity measurements, J. Biome. Opt., (14) 024049

Pan, X., Yu, H., Shi, X., Korzh, V., & Wohland, T., 2007, Characterization of flow direction in microchannels and zebrafish blood vessels by scanning fluorescence correlation spectroscopy" *J. Biome. Opt.*, (12) 014034

Acknowledgements

As a foreign student, I can still vividly remember the feeling of loneliness and helplessness when I first came to Singapore and NUS. Without the help of many people, a life would be difficult for the past five years, let alone a doctoral thesis. Taking this opportunity, I would like to express my deepest gratitude to them all.

I am heartily thankful to my supervisor Associate Professor Thorsten Wohland for introducing me this exciting research project and guiding me all the way with great patience. His passion for scientific research deeply inspired me and his German-style seriousness towards work gradually influenced me. This thesis would not be possible without his enlightening advices and heartening encouragements.

I would like to thank my co-supervisor Associate Professor Vladimir Korzh for offering me the opportunity to join his family-like research group and showing me the exciting world of developmental biology. His kind support was always available through these years and his profound knowledge of zebrafish research provided numerous new ideas to this cross-disciplinary project.

I would like to show my gratitude to Associate Professor Sohail Ahmed and Associate Professor Rachel Kraut for the great collaboration. Their warm help and support made crucial contribution to this work.

I am grateful to all my colleagues from the Biophysical Fluorescence Laboratory in NUS: Liu Ping for helping me with the biological sample handling and FCS measurements in cell cultures; Pan Xiaotao for helping me with the FCS alignments and the two photon excitation instrument setup; Guo Lin and Foo Yong Hwee for helpful discussions and collaboration; Yu Lanlan, Hwang Ling Chin, Liu Jun, Har Jar Yi, Kannan Balakrishnan, Manna Manoj Kumar, Teo Lin Shin and Jagadish Sankaran for their friendships and support.

I am also grateful to all my colleagues from the Fish Development Biology Laboratory in IMCB: in particular, Chong Shang-Wei for guidance of basic biology and zebrafish research; Cathleen Teh, Poon Kar Lai and William Go for technical assistance, helpful discussion and their friendships.

Last but not least, I would like to thank my parents for their unconditional love and care. I would like to thank my beautiful wife Zhang Guifeng for her continuous support, love and the happiest moments she brings to my life.

Table of Contents

Summary

Fluorescence correlation spectroscopy (FCS) and fluorescence cross-correlation spectroscopy (FCCS) are widely used biophysical techniques to determine biomolecule concentrations, photophysical dynamics of fluorophores, diffusion coefficients of DNAs and proteins, and dissociation constants of interacting particles. In this work, we extended the application of FCS and single wavelength fluorescence cross-correlation spectroscopy (SW-FCCS), a variant of FCCS developed in our lab, to a multicellular living organism. We chose zebrafish embryo for this purpose as its transparent tissue aided the investigations of cells deep beneath skin. We first examined how and to what extent zebrafish embryos can be studied using FCS. Then the applicability of FCS to study molecular processes in embryo was demonstrated by the determination of blood flow velocities with high spatial resolution and the determination of diffusion coefficients of cytoplasmic and membrane-bound enhanced green fluorescence protein (EGFP) labeled proteins in different subcellular compartments as well as in different cell types. Lastly, we show that protein-protein interactions can be directly quantified in muscle fiber cells in living zebrafish embryo with SW-FCCS. This thesis is organized in the following chapters:

1. Chapter 1 introduces the motivation to study protein dynamics and interactions in living organisms. It provides a literature review on the history and development of FCS/SW-FCCS, as well as the application of FCS/SW-FCCS in studying biomolecule dynamics and interactions.
2. Chapter 2 describes the theories and experimental setups of FCS and SW-FCCS. The preparation of biological samples and the preparation of zebrafish embryo for imaging and FCS measurement are also illustrated and discussed in this chapter.
3. Chapter 3 examines how and to what extent zebrafish embryo can be used as a model for the study of molecular processes. Firstly, the approaches to express foreign genes in zebrafish embryos are discussed and compared with that in cell cultures. Secondly, the autofluorescence in living zebrafish embryos, in particular the autofluorescence distribution and emission spectra, is examined in order to minimize background interference. Lastly, the working distance of FCS measurements in zebrafish tissues is studied with both one photon excitation and two photon excitation.

4. Chapter 4 presents the studies of molecular processes in living zebrafish embryos with FCS. We first show that systolic and diastolic blood flow velocities can be noninvasively determined with high spatial resolution even in the absence of red blood cells. We then show that diffusion coefficients of cytoplasmic and membrane-bound proteins can be accurately determined. We measure the diffusion coefficients of EGFP in cytoplasm and nucleoplasm, as well as in motor neuron cells and muscle fiber cells. We also determine the diffusion coefficients of Cxcr4b-EGFP, an EGFP labeled G protein coupled receptor (GPCR), on the plasma membrane of the muscle fiber cells. We finally analyze the FCS data with the anomalous subdiffusion model and study the molecular crowdedness of cells in living embryos.
5. Chapter 5 describes the direct quantification of protein-protein interactions in living zebrafish embryos with SW-FCCS. The SW-FCCS instrument is calibrated using Rhodamine 6G and the effective volume is calculated accordingly. Positive (mRFP-EGFP tandem construct) and negative (individually expressed mRFP and EGFP) controls are measured first to probe the upper and lower limits of SW-FCCS measurements in embryos. Then the interactions of Cdc42, a small Rho-GTPase, and IQGAP1, an actin-binding scaffolding protein, are studied and the dissociation constants are determined. Finally, the results obtained in zebrafish embryos are compared to that in Chinese hamster ovary cell cultures.
6. Chapter 6 concludes the finding in this work and envisions the future development of FCS/SW-FCCS in embryos.

List of Tables

List of Figures

List of Symbols and Acronyms

α	anomality factor
η	medium viscosity
τ	correlation time
τ_d	diffusion time
τ_f	flow time for a molecule through the observation volume
τ_{trip}	triplet state relaxation time
ω_0	the radial distance where the excitation intensity reaches $1/e^2$ of its value at the center of the observation volume
χ^2	Chi square, used to describe goodness-of-fit
ACF	autocorrelation function
APD	avalanche photodiode
C	Concentration
CCD	charge-coupled device
CCF	cross-correlation function
Cdc42	cell division cycle 42
CHD	Calponin homology domain
CHO	Chinese hamster ovary
CLSM	confocal laser scanning microscopy
CMV	Cytomegalovirus
cps	count rate per molecule per second
Cxcr4a/b	chemokine (C-X-C motif) receptor 4a/b
D	diffusion coefficient
DNA	deoxyribonucleic acid
dpf	days post fertilization
EGFP	enhanced green fluorescence protein
EGFR	epidermal growth factor receptor

EMCCD	electron multiplying charge-coupled device
EtBr	ethidium bromide
F(t)	fluorescence intensity at time t
FCM	fluorescence correlation microscopy
FCS	fluorescence correlation spectroscopy
FCCS	fluorescence cross-correlation spectroscopy
FLIM	fluorescence lifetime imaging microscopy
Flu	Fluorescein
FP	fluorescence protein
FRAP	fluorescence recovery after photobleaching
FRET	fluorescence resonance energy transfer
F_{trip}	the fraction of the particles that have entered the triplet state
g_x, g_y, g_z	basic term of correlation function in each dimension
$G(0)$	correlation function amplitude
$G(\tau)$	correlation function
G_∞	the convergence value of $G(\tau)$ for infinite time
GDP	guanosine diphosphate
GEF	guanine nucleotide exchange factor
GPCR	G-protein coupled receptor
GRD	GAP-related domain
GTP	guanosine triphosphate
IQGAP1	IQ motif containing GTPase activating protein 1
K	Boltzmann's constant
K	geometric ratio of axial to radial distance of the observatoion volume, where $K = z_0 / \omega_0$
K_D	dissociation constant
hpf	hours post fertilization
M	molecular mass
MO	morpholino oligos
mRFP	monomeric red fluorescence protein
N	number of molecules

N_A	Avogadro's number
NA	numerical aperture
NIR	near infrared
N-WASP	neural-Wiskott-Aldrich syndrome protein
OPE	one-photon excitation
PBS	phosphate buffer solution
PCH	photon counting histogram
PCR	polymerase chain reaction
PIV	particle imaging velocity
PMT	photomultiplier tubes
PSF	point spread function
PTU	0.003% 1-phenyl-2-thiourea in 10% Hank's saline
QD	quantum dots
R6G	rhodamine 6G
SD	standard deviation
SW-FCCS	single wavelength fluorescence cross-correlation spectroscopy
SPT	single particle tracking
T	absolute temperature
TIR	total internal reflection
TMR	tetramethylrhodamine
TPE	two-photon excitation
UV	Ultraviolet
V_{eff}	effective observation volume
z_0	the axial distance where the excitation intensity reaches $1/e^2$ of its value at the center of the observation volume

Chapter 1

Introduction

The end of the 20th and the beginning of the 21st century witnessed exciting developments in the life sciences and the emergence of novel questions within the field. In particular, the advances in molecular and cell biology brought the need to understand cell behavior based on very fundamental molecular processes. However, conventional ensemble or bulk measurements cannot address this issue as single molecule parameters and their distribution are masked by the ensemble averages and standard deviations. Under ensemble measurement, questions whether there is one or multiple molecular species, e.g. proteins of multiple conformations, cannot be answered. Thus new tools and strategies that can detect single molecules and distinguish a single molecule among heterogeneous populations are needed. The first single molecule detection was achieved in 1976 using fluorescence microscopy (Hirschfeld, 1976). Fluorescence-based techniques are advantageous in terms of specificity, sensitivity and versatility. They are non-destructive to the samples and thus can be applied to living cells in real-time. By labelling the object of interest with a fluorophore and illuminating a small observation volume with a tightly focused laser beam, single molecule detection can be achieved even in the presence of

cellular autofluorescence (Yu et al, 2006). In addition, fluorescence intensity is directly proportional to the number of fluorophores, providing the basis for quantitative analysis. Consequently, the field of fluorescence microscopy and spectroscopy grew at an accelerating pace and is still growing strongly with an ever increasing number of new techniques and methods being published (Haustein & Schwille, 2007; Hwang & Wohland, 2007; Kolin & Wiseman, 2007; Liu et al, 2008a; Thompson et al, 2002).

Florescence correlation spectroscopy (FCS), one group of the fluorescence methods, analyzes fluorescence intensity fluctuations from a confined observation volume with single molecule sensitivity but at the same time based on fast statistical treatment of the recorded data. Any process within the volume which causes variations in the fluorescence intensity and happens on a time scale slower than the recording speed will leave characteristic fluctuations in the intensity trace. By performing either a Fourier transformation or an autocorrelation analysis, parameters such as local concentrations, molecular mobility and photophysical dynamics can be determined for the fluorescently labeled molecules. FCS was first introduced by Magde, Elson and Webb in the 1970s (Elson & Magde, 1974; Magde et al, 1972). In its first appearance, Magde and others successfully monitored the binding reaction between ethidium bromide (EtBr) and double stranded DNA using FCS. The selection of EtBr and DNA simplified the situation as the fluorescence quantum yield of EtBr increases 20 times upon insertion into the DNA. However, the early FCS measurements suffered from poor signal-to-noise ratio due to technical limitations and the applicability of FCS was quite limited. In the following two decades, FCS was held back in favour of photobleaching methods for diffusion

coefficient measurements. The renaissance of FCS came in 1993, when Rigler et al. introduced a confocal illumination scheme to improve the signal-to-noise ratio of FCS measurements (Rigler et al, 1993b). The use of a tightly focused laser beam and a small pinhole in this setup generated a very small observation volume on the range of one femtoliter (10^{-15} L). This ensured that a minimum number of molecules were detected, and thus the fluctuations caused by single molecules can be easily distinguished, which in return guaranteed good signal-to-noise ratio. Since then, FCS became an increasingly popular technique to study molecular dynamics and the applicability was extended. In the following years, FCS has been used to measure translational diffusion (Rigler et al, 1993b), singlet-triplet interactions of fluorophores (Widengren & Rigler, 1995), photophysical properties of chemical dyes (Widengren & Schwilles, 2000) and fluorescent proteins (Haupts et al, 1998; Maeder et al, 2007; Schwille et al, 2000), chemical reactions (Widengren & Rigler, 1998), pH values in subcellular compartments (Llopis et al, 1998), hydrodynamic flow profile in microchannel structures (Gosch et al, 2000) with more applications coming as I write.

FCS can also be used to measure inter-molecular binding, e.g. receptor-ligand interactions (Rauer et al, 1996; Van Craenenbroeck & Engelborghs, 1999; Wohland et al, 1999; Wruss et al, 2007; Zemanova et al, 2004). It is based on the theory that relative changes in mass upon binding lead to a reduction in the diffusion coefficient. However, in order to distinguish two components (before and after binding) in FCS, their diffusion coefficients must differ by at least a factor of 1.6 (Meseth et al, 1999). Based on the Stokes-Einstein relation ($D^{-1} \sim M^{1/3}$), the mass must differ by at least a factor of 4. Dimerization is therefore difficult to resolve. In addition, FCS cannot

resolve specific binding in a multi-component system, and protein-protein interactions in living cells are generally not assessable due to the complex environment and a large number of potentially interacting components. Therefore in 1994, the concept of multiple colors fluorescence cross-correlation spectroscopy (FCCS) was introduced to specifically study molecular binding (Eigen & Rigler, 1994). In dual-color FCCS, both binding partners of interest are labelled with distinct fluorescent dyes. The two labels are simultaneously excited and fluorescence signals are collected in separate channels. Aside from the autocorrelation of signals from each channel, the signals from both channels are cross-correlated. The binding induced concurrent movement of the two labels therefore produces a positive signal in the cross-correlation analysis. Dual-color FCCS was first experimentally realized by Schwille et al. to measure nucleic acid hybridizations (Schwille et al, 1997), and the potential of FCCS to effectively measure biomolecular interactions was demonstrated in the following years both *in vitro* (Camacho et al, 2004; Foldes-Papp & Rigler, 2001; Kettling et al, 1998; Korn et al, 2003) and *in vivo* (Bacia et al, 2002; Baudendistel et al, 2005; Muto et al, 2006; Saito et al, 2004). Since this technique is independent of distance and orientation of the fluorophore, FCCS represents an attractive alternative to Fluorescence Resonance Energy Transfer (FRET) measurements which are typically used to study molecular interactions (Liu et al, 2008a).

In the realm of biological research, biochemical techniques were firstly employed, which allowed the separation and purification of cellular components. Isolated components or proteins can thereby be used in *in vitro* experiments to model biochemical reactions and molecular interactions. This information was then

combined and interweaved to reproduce the complex cellular processes involving multiple components and structures. Biochemical experiments provide a simplified and controllable platform, but it is also crucial to be able to observe and quantify biological processes directly in living cells, as the subcellular localization, subcellular compartmentalization and local concentration also play important roles in defining biological processes. Fluorescence-based biophysical methods, also known as F-techniques, i.e. FRAP, FRET, FLIM, and FCS/FCCS, thereby came to the forefront in this research. FCS and FCCS are well suited for intracellular applications. They are non-invasive in nature and highly sensitive. The spatial resolution of FCS/FCCS is defined by the size of the confocal volume, usually less than one micrometer in dimension and can be further reduced to the nanometer scale (Eggeling et al, 2009). In typical biological samples, biomolecular concentrations range from 1 nM to 1 µM, which results in about 1 – 1000 particles in the observation volume, a range just measurable by FCS. Therefore, FCS can be directly used to study protein dynamics at their physiological expression levels. At the same time, FCS provides a wide range of temporal information from microseconds to seconds. This allows measurement of a broader spectrum of biomolecules, whose diffusion behaviour can be extremely diverse in living biological samples. Furthermore, new instrumentations that combine FCS with imaging techniques, e. g. confocal laser scanning microscopy (CLSM), also expand the applicability of FCS in biological samples. The combination, also known as fluorescence correlation microscopy (FCM, Brock & Jovin, 1998; Pan et al, 2007a; Terry et al, 1995), allows the user to obtain an image of the sample first before identifying a position on the image where subsequent FCS measurements can be performed. This is especially useful in intracellular

applications. The typical volume of a eukaryotic cell is 10^{-12} L, which is three orders of magnitude larger than the observation volume of FCS. Using FCM, protein dynamics can be specifically investigated in subcellular compartments. Owing to those advantages, the solution-based technique saw more and more applications in the field of cell biology (Bacia et al, 2006; Hwang & Wohland, 2007; Kim et al, 2007; Liu et al, 2008b; Schwille, 2001).

However, up to now, most intracellular measurements using FCS and FCCS are performed in Petri dish-based cell culture systems. Cell cultures are engineered as isolated individual cells that can be artificially cultivated. Since their introduction, 2D cell cultures have greatly enhanced our understanding of cellular behaviour and molecular actions and interactions. The commonly used 2D cell cultures have the advantage of easy genetic manipulation and direct accessibility to biochemical and biophysical analysis. The highly controlled and simplified cellular environment has made possible single molecule detection within the complex matrix of cells. Nowadays, Petri-dish based cell culture systems have become a standard tool of research in cell and molecular biology, and cell culture based drug screening is regularly performed in the pharmaceutical industry. Nevertheless, 2D cell cultures cannot fully reflect the natural environment of cells present in living organisms. The flat glass substrate and the artificial medium buffer are significantly different from a real physiological environment. The absence of extracellular matrix and various cell-cell communication functions also makes the information harvested not predictive in drug development. Numerous studies have pointed out the insufficiency of 2D cell culture as a biological research model. Mooney et al. showed that even genetically normal primary cells placed in cell culture quickly lose their

differentiated gene expression pattern and phenotype (Mooney et al, 1992). By culturing cells in a 3D structure, Weaver et al. demonstrated that malignant breast tumour cells can revert to their original state when an antibody against β-integrin is added to the system (Weaver et al, 1997), while this result cannot be reproduced in 2D cell culture. In another report by Anders et al., a receptor responsible for cell infection was found to have similar and high level of expression in both normal and malignant cells in 2D cell culture, but in 3D only malignant cells carried large number of the receptors (Anders et al, 2003). All these findings suggest that the physiological relevance of findings made in 2D culture remains unclear and questions of developmental biology cannot be addressed in this simplified and biased model. Therefore, it is desirable to extend FCS and FCCS measurements into optically accessible small living organisms, e.g. nematodes (*Caenorhabditis elegans*), fruit flies (*Drosophila melanogaster*), medaka (*Oryzias latipes*) and zebrafish (*Danio rerio*) to gather physiologically relevant data.

Up till now, FCS application in living animals is still limited due to the thick tissue induced light scatterings. In one example, Nagao and others reported diffusion coefficient measurements of GFP labeled granules in medaka primordial germ cells using FCS and fluorescence recovery after photobleaching (FRAP) (Nagao et al, 2008). To avoid the deep tissue penetration, the medaka embryos were dissected and cells of interest were revealed. In contrast, working with much smaller animals Petrasek and others applied scanning FCS to study the localization and redistribution of GFP labelled NMY-2 and PAR-2 proteins during the asymmetric first division of *C. elegans* embryos (Petrasek et al, 2008). Working with transparent animals helps to alleviate this problem too. We have recently shown that FCS can be

used efficiently to measure blood flow velocities in livimg zebrafish embryos (Korzh et al, 2008; Pan et al, 2007b).

In this thesis, the applicability of FCS and FCCS is studied in detail in living zebrafish embryo. Zebrafish, as a model of vertebrate development, has been introduced only relatively recently. But it is fast catching up as many methodologies developed in *Drosophila* and other models are transferred to zebrafish research (Chakrabarti et al, 1983; Streisinger et al, 1981; Stuart et al, 1988). As a model species it is more complex, evolutionarily closer to humans and amenable to standard genetic and molecular tools. Numerous human diseases, both genetic and acquired, can be introduced and studied in zebrafish, which made it a model vertebrate of choice for drug discovery and large-scale studies of genetics, development and regeneration (Fetcho et al, 2008; Korzh, 2007; Lieschke & Currie, 2007; Strahle & Korzh, 2004). In addition, zebrafish are small, easy to grow and sexually reproductive within three months after fertilization. Zebrafish embryos are fertilized and develop externally and the embryos and early larva are optically transparent, allowing investigation of cell-biological events deep within the tissue.In this work, we explore the limitation of FCS and FCCS and their use in zebrafish embryos and demonstrate several applications of FCS in living zebrafish embryos, showing that single molecule-based studies in living organism are possible:

1. The autofluorescence expression pattern of zebrafish embryo was studied first to minimize background interference. The autofluorescence distribution was examined in the embryo body, and the autofluorescence spectrum and intensity was investigated.

2. The penetration depth of FCS in the embryo tissue was explored with both one-photon excitation (OPE) and two-photon excitation (TPE).
3. The blood flow velocities in different vessels were measured.
4. The diffusion coefficients of cytoplasmic and membrane-bound EGFP and EGFP labelled proteins were measured in different subcellular compartments and different cell types.
5. The dissociation constants (K_D) of the interacting protein pair of Cdc42 and IQGAP1 was determined using single wavelength fluorescence cross-correlation spectroscopy (SW-FCCS).

Chapter 2

Theory and Methods

2.1 Fluorescence Correlation Spectroscopy

2.1.1 The Autocorrelation Analysis

A correlation between two variables *a* and *b* describes the dependence of these two variables. In practical terms this means that if we know the value of *a* or *b* we can make some prediction of the value of *b* or *a*, respectively. The concept of correlation is very useful since it allows some predictions about the second variable from the observation of the first one. Now if we have two variables *a* and *b* which are correlated, then the values of the two variables will change with a similar pattern. Consequently, we expect that a multiplication of the two variables with each other will reinforce this pattern. If we calculate now the average values of *a*, *b* and the product of *a*·*b*, we expect (Berne & Pecora, 2000):

$$\langle a \cdot b \rangle > \langle a \rangle \langle b \rangle \tag{2.1}$$

where $\langle\ \rangle$ denotes the average value. We can simplify the description of correlations by normalizing $\langle a \cdot b \rangle$ with $\langle a \rangle \langle b \rangle$:

$$g = \frac{\langle a \cdot b \rangle}{\langle a \rangle \langle b \rangle} \tag{2.2}$$

The value of *g* is now 1 for uncorrelated variables and >1 for correlated variables.

If we have one variable *a* whose values change over a duration of time, and we correlate the values of the same variable at different time point, e.g. $a(t)$ and $a(t+\tau)$, where τ describes the difference in time, we then have a so called "autocorrelation" analysis. The correlation between $a(t)$ and $a(t+\tau)$ will only be found if the value of the variable persists longer than the time τ, i.e. $a(t)$ changes on a time scale larger than τ. The autocorrelation function (ACF) is written as:

$$G(\tau) = \frac{\langle a(t) \cdot a(t+\tau) \rangle}{\langle a(t) \rangle \langle a(t+\tau) \rangle} \tag{2.3}$$

It describes the self-similarity of a signal (values of the variable) in time. Therefore, the ACF is an indication in how far we can make predictions into the future of the values of a variable. If the variable has long correlation in time we can make predictions far ahead; if the correlation time is short we can predict the future only over short time spans. If the correlation is strong we can make good predictions; if the correlation is weak our prediction will be less accurate.

In FCS measurements, the fluorescence intensities over time $F(t)$ are measured in a confined observation volume where fluorescent probes undergo different

processes, e.g. chemical reactions, enzymatic reactions, translational and rotational diffusion and photophysical transitions. Any fluorescent probe, which is within the observation volume and undergoes one of these processes, will create fluctuation in the fluorescence intensity. Here, a fluctuation means a transient deviation of the fluorescence intensity from its average value:

$$\delta F(t) = F(t) - \langle F \rangle \tag{2.4}$$

These fluctuations contain information about the characteristic time of the process and of the frequency of occurrence. By measuring the fluorescence signal and subjecting it to an autocorrelation analysis we can find out in how far a signal which is found a time τ in the future is related to the signal at present. The ACF in this case is written as:

$$G(\tau) = \frac{\langle F(t) \cdot F(t+\tau) \rangle}{\langle F(t) \rangle \langle F(t+\tau) \rangle} = \frac{\langle F(t) \cdot F(t+\tau) \rangle}{\langle F(t) \rangle^2} \tag{2.5}$$

For the derivation of the right hand side we assume that the processes under investigation are stationary, i.e. the statistical properties of the processes are invariant to a shift in time so:

$$\langle F(t+\tau) \rangle = \langle F(t) \rangle \tag{2.6}$$

For times smaller than the characteristic duration of a molecular process, τ_p, one expects that the fluctuations are dependent on each other. But for times much longer than τ_p there should be no dependence anymore between the fluctuations. For times similar to τ_p, there will be a transition from correlation to non-correlation.

In general, the correlation of the signal $F(t)$ is largest if compared at the same time, i.e. the time shift is zero:

$$\tau = 0: \quad G(0) = \frac{\langle F(t)^2 \rangle}{\langle F(t) \rangle^2} \geq G(\tau) \tag{2.7}$$

Assuming the processes under investigation have a finite duration, therefore the signal $F(t)$ is uncorrelated when the time shift is infinite:

$$\tau = \infty: \quad G(\infty) = 1 \tag{2.8}$$

Now if we incorporate Eq. (2.4) into Eq. (2.5), we have:

$$\begin{aligned} G(\tau) &= \frac{\langle F(t+\tau)F(t) \rangle}{\langle F(t) \rangle^2} = \frac{\langle (\delta F(t+\tau) + \langle F \rangle)(\delta F(t) + \langle F \rangle) \rangle}{\langle (\delta F(t) + \langle F \rangle) \rangle^2} \\ &= \frac{\langle \delta F(t+\tau)\delta F(t) \rangle + \langle F \rangle^2}{\langle F \rangle^2} = \frac{\langle \delta F(t+\tau)\delta F(t) \rangle}{\langle F(t) \rangle^2} + 1 \end{aligned} \tag{2.9}$$

Here we have used the property that the average of the fluctuations over time is 0, i.e. $\langle \delta F(t) \rangle = 0$. We can define now the fluorescence signal $F(t)$ and its fluctuations $\delta F(t)$ of a sample measured with an instrument over space ($\vec{r} = (x, y, z)$):

$$F(t) = \kappa \int I(\vec{r}) \cdot CEF(\vec{r}) \cdot C(\vec{r}, t)\, d\vec{r} \tag{2.10}$$

$$\delta F(t) = \kappa \int I(\vec{r}) \cdot CEF(\vec{r}) \cdot \delta C(\vec{r}, t)\, d\vec{r} \tag{2.11}$$

where κ is a product of the fluorophore absorption cross section, its quantum yield and the overall system detection efficiency, $I(\vec{r})$ is the illumination intensity profile, and $CEF(\vec{r})$ is the normalized collection efficiency function of the system for different points in the sample, and $C(\vec{r}, t)$ and $\delta C(\vec{r}, t)$ are functions describing the concentration of particles and their fluctuations, respectively, within the sample. As

mentioned above, the fluctuation $\delta C(\vec{r},t)$ can be induced by the fluorescent probes undergo various processes. By inserting Eq. (2.10) and Eq. (2.11) into Eq. (2.9), the correlation function can then be written as

$$G(\tau)=\frac{\iint I(\vec{r})I(\vec{r}')\cdot CEF(\vec{r})CEF(\vec{r}')\cdot\langle\delta C(\vec{r}',t+\tau)\delta C(\vec{r},t)\rangle d\vec{r}d\vec{r}'}{\langle C\rangle^2\left(\int I(\vec{r})\cdot CEF(\vec{r})d\vec{r}\right)^2}+1 \qquad (2.12)$$

where $\langle C\rangle$ is the mean concentration of the molecules. This equation can be analytically or numerically solved for different illumination profiles, collection efficiency functions, and functions describing the fluctuation in fluorescent particles (e.g. diffusion, flow, fluorophore blinking, or chemical reactions).

2.1.2 Translational Diffusion

In a typical confocal FCS setup, the illumination profiles is given by a laser beam which is focused into a small diffraction limited spot. The spatial intensity distribution of the focused laser beam is approximated as a Gaussian-Gaussian-Lorentzian profile (Saleh & Teich, 1991). Then the pinhole in the confocal setup removes out-of-focus light by reducing the collection efficiency along the z-axis the further the emission happens from the focal plane. The two effects together can be approximated by a simple rotationally symmetric function which is Gaussian in all three dimensions (Rigler et al, 1993a)

$$W(\vec{r}) = I(\vec{r}) \cdot CEF(\vec{r}) = I_0 e^{-2x^2/w_0^2} e^{-2y^2/w_0^2} e^{-2z^2/z_0^2} \tag{2.13}$$

where $I_0 = \frac{2P}{\pi\omega_0}$ is the excitation intensity at the center of the laser beam with laser power *P*. ω_0 and z_0 are the radial and axial distances at which the laser beam has decreased to *1/e²* of the intensity maximum at the center of the beam.

In the case of single component translational diffusion, the correlation of concentration fluctuation can be described by the so-called diffusion propagator (Weidemann et al, 2002):

$$\langle \delta C(\vec{r}', t+\tau) \delta C(\vec{r}, t) \rangle = \langle C \rangle \frac{e^{-\frac{(r-r')^2}{4D\tau}}}{8(\pi D\tau)^{3/2}} \tag{2.14}$$

where *D* is the diffusion coefficient of the single component. Putting this information together we get:

$$\begin{aligned} G(\tau) &= \frac{\iint W(\vec{r}) W(\vec{r}') \cdot \langle \delta C(\vec{r}', t+\tau) \delta C(\vec{r}, t) \rangle d\vec{r} d\vec{r}'}{\langle C \rangle^2 \left(\int W(\vec{r}) d\vec{r} \right)^2} + 1 \\ &= \frac{\iint e^{-2(x^2-x'^2)/w_0^2} e^{-2(y^2-y'^2)/w_0^2} e^{-2(z^2-z'^2)/z_0^2} \cdot \frac{e^{-\frac{(r-r')^2}{4D\tau}}}{8(\pi D\tau)^{3/2}} d\vec{r} d\vec{r}'}{\langle C \rangle \left(\int e^{-2x^2/w_0^2} e^{-2y^2/w_0^2} e^{-2z^2/z_0^2} d\vec{r} \right)^2} + 1 \end{aligned} \tag{2.15}$$

The integration gives the following solution:

$$G(\tau) = \frac{1}{\langle C \rangle \pi^{3/2} w_0^2 z_0} \left(1 + \frac{4D\tau}{w_0^2} \right)^{-1/2} \left(1 + \frac{4D\tau}{w_0^2} \right)^{-1/2} \left(1 + \frac{4D\tau}{z_0^2} \right)^{-1/2} + 1 \tag{2.16}$$

where $\pi^{3/2} w_0^2 z_0$ can be defined as the effective volume V_{eff} that is valid for the 3D Gaussian profile given in Eq. (2.13), and is in general a constant depending on the actual observation volume, $W(\vec{r})$. For practical purposes the function is often written as:

$$G(\tau) = \frac{1}{N}\left(1+\frac{\tau}{\tau_d}\right)^{-1}\left(1+\frac{\tau}{K^2\tau_d}\right)^{-1/2} + G_\infty \tag{2.17}$$

with:

$$N = \langle C \rangle \pi^{2/3} w_0^2 z_0 = \langle C \rangle \cdot V_{eff} \tag{2.18}$$

$$\tau_d = \frac{\omega_0^{\,2}}{4D} \tag{2.19}$$

N is defined as the apparent number of particles in the confocal volume (observation volume). τ_d is defined as the diffusion time required for one fluorophore to diffuse through the confocal volume. As the confocal volume is elongated in the direction z_0, $K = z_0/\omega_0$ is then the geometric ratio of axial to radial dimensions of the confocal volume. G_∞, the convergence value, is introduced as a free parameter. The value of G_∞, which is 1 for an infinite measurement time, can differ slightly from 1 for finite measurement times. In general, the parameter G_∞ will deviate from 1 by less than 1% in solution measurements. If G_∞ deviates strongly from 1 it can be an indication of photobleaching (Dittrich & Schwille, 2001), i.e. the fluorescence signal decays exponentially during the measurement owing to

the destruction of fluorescent molecules. Other problems in its value can originate from instabilities of the setup or a moving sample.

The basic term for the correlation function is a hyperbolic function for each dimension: $g_x = g_y = \left(1+\frac{\tau}{\tau_d}\right)^{-1/2}$ and $g_z = \left(1+\frac{\tau}{K^2\tau_d}\right)^{-1/2}$. In case of 3D translational diffusion: $G(\tau) = \frac{1}{N}\cdot g_x \cdot g_y \cdot g_z + G_\infty$, which is essentially Eq. (2.17). If translational diffusion occurs only in 2D such as on a cell membrane, then the ACF only has the portion of g_x and g_y:

$$G(\tau) = \frac{1}{N}\cdot g_x \cdot g_y + G_\infty = \frac{1}{N}\left(1+\frac{\tau}{\tau_d}\right)^{-1} + G_\infty \tag{2.20}$$

In both 2D and 3D translational diffusion, the amplitude of the ACF ($G(0)$) is inversely proportional to the number of particles in the confocal volume (Fig. 2.1D):

$$G(0) = \frac{1}{N} + G_\infty \tag{2.21}$$

However, the absolute concentration of a sample is not directly calculated from the number of particles N and the theoretical observation volume size V_{eff} using Eq. (2.18) but are rather determined by using a standard dye solution of a fixed known concentration against which all other concentrations are calibrated. In this case an N_{calib} is determined for the standard solution of concentration C_{calib} and the concentration of any other sample x is then:

$$C_x = \frac{N_x \cdot C_{calib}}{N_{calib}} \tag{2.22}$$

In analogy, the diffusion coefficient *D* is not directly calculated from diffusion time τ_d and the radial distance of the confocal volume ω_0 in Eq. (2.19) but determined by using calibration dye solution with known diffusion coefficient:

$$D_x = \frac{\tau_{d\,calib} \cdot D_{calib}}{\tau_{d\,x}} \tag{2.23}$$

Up till now, all of the above discussion deals with single component system. In the case of multiple component translation diffusion in 3D, a general solution for confocal FCS can also be obtained (Thompson, 1991; Yu et al, 2005):

$$G(\tau) = \frac{1}{N} \frac{\sum_i \beta_i^2 F_i g_{3D_i}}{\left(\sum_i \beta_i F_i\right)} + G_\infty \tag{2.24}$$

where $g_{3D} = g_x \cdot g_y \cdot g_z = \left(1+\frac{\tau}{\tau_d}\right)^{-1}\left(1+\frac{\tau}{K^2\tau_d}\right)^{-1/2}$ (if multiple component diffuse in 2D, $g_{2D} = g_x \cdot g_y = \left(1+\frac{\tau}{\tau_d}\right)^{-1}$ will be used here instead). β_i is the fluorescence yield of particle *i* compared to the fluorescence yield of particle 1. F_i is the mole fraction of component *i* in the overall sample (Fig. 2.1F).

In addition to translational diffusion of fluorophores through the confocal volume, triplet state build-up can also induce fluorescence fluctuation. At high excitation laser power, the excited singlet state can become highly populated and a proportion of them nonradiatively transit to a triplet state through intersystem crossing. This transition from triplet state to ground state happens at a time range of microsecond which can be distinguished from the translational diffusion time of

dye molecules, usually on the millisecond range (Fig. 2.1). A function that describes triplet state kinetic can thus be multiplied with the basic correlation functions (Widengren et al, 1995; Widengren et al, 1994):

$$g_{trip} = 1 + \left(\frac{F_{trip}}{1 - F_{trip}} \right) \cdot \exp\left(-\tau / \tau_{trip} \right) \tag{2.25}$$

where F_{trip} is the fraction of the particles that have entered the triplet state; τ_{trip} is the triplet state relaxation time (Fig. 2.1G). For one example, if one fluorophore diffuses in 3D and possesses one triplet state, the ACF can be written as:

$$\begin{aligned} G(\tau) &= \frac{1}{N} \cdot g_{trip} \cdot g_{3D} + G_{\infty} \\ &= \frac{1}{N} \cdot \left[1 + \left(\frac{F_{trip}}{1 - F_{trip}} \right) \cdot \exp\left(-\tau / \tau_{trip} \right) \right] \cdot \left[\left(1 + \frac{\tau}{\tau_d} \right)^{-1} \left(1 + \frac{\tau}{K^2 \tau_d} \right)^{-1/2} \right] + G_{\infty} \end{aligned} \tag{2.26}$$

For another example, two particles with different diffusion coefficients diffuse in a confined 2D plane. Considering the fluorophore possesses one triplet state, the ACF can be written as:

$$\begin{aligned} G(\tau) &= \frac{1}{N} \cdot g_{trip} \cdot \frac{\sum_{i=2} F_i g_{2D_i}}{\left(\sum_{i=2} F_i \right)} + G_{\infty} \\ &= \frac{1}{N} \cdot \left[1 + \left(\frac{F_{trip}}{1 - F_{trip}} \right) \cdot \exp\left(-\tau / \tau_{trip} \right) \right] \cdot \left[(1 - F_2) \times \left(1 + \frac{\tau}{\tau_{d1}} \right)^{-1} + F_2 \times \left(1 + \frac{\tau}{\tau_{d2}} \right)^{-1} \right] + G_{\infty} \end{aligned} \tag{2.27}$$

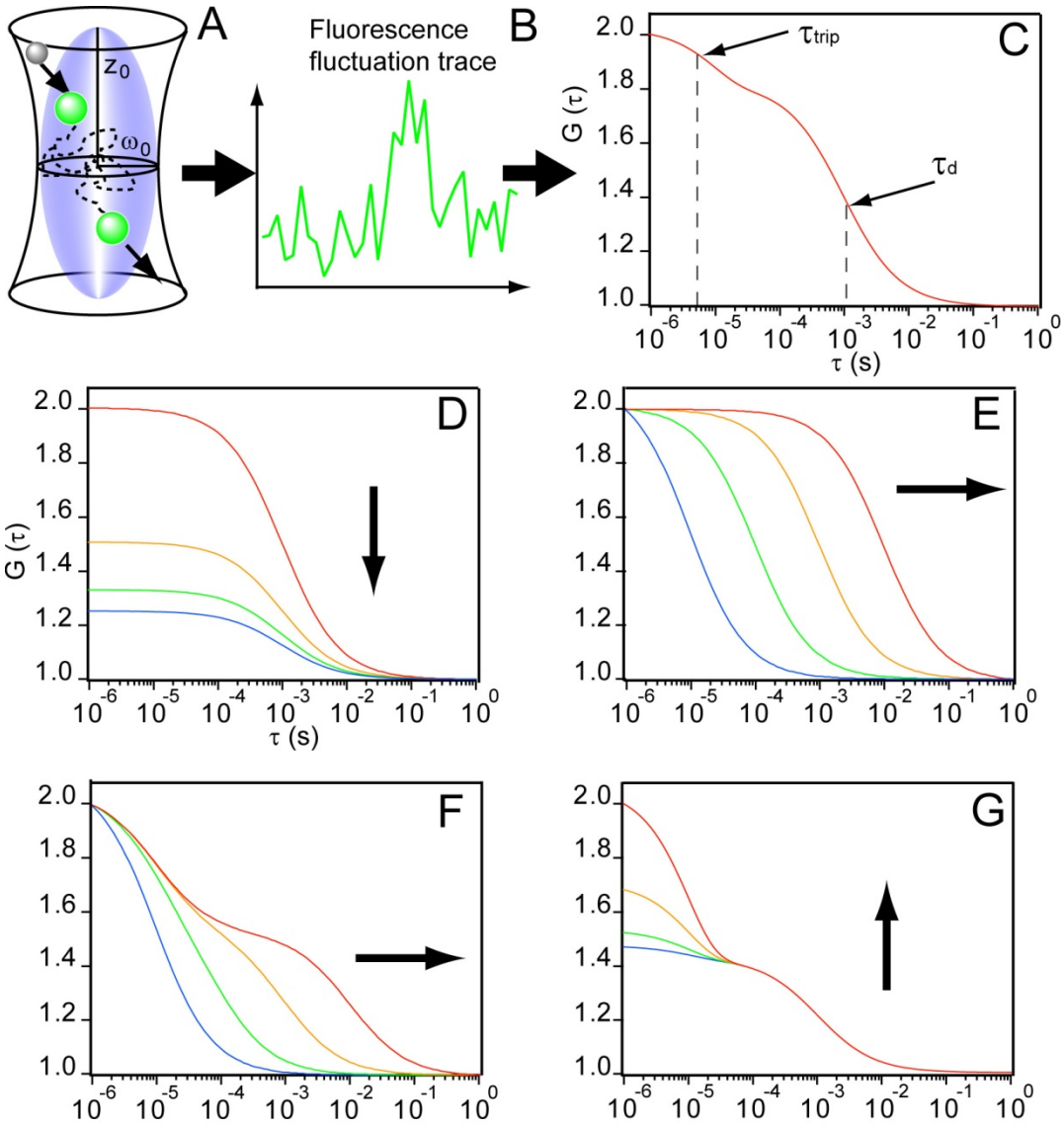

Fig. 2.1: Characteristics of fluorescence correlation functions. A) Particles diffusion through the confocal volume with half axis ω_0 and z_0 give rise to B) fluorescence intensity fluctuations. C) This graph shows a typical fluorescence correlation function with 2 different parts: transitions to the triplet state, which represents a forbidden transition and thus has a long lifetime typically in the microsecond range; and diffusion of fluorescent molecules through the confocal volume. D) The change in an ACF due to changes in concentration; the arrow indicates increasing concentration. E) Changes in an ACF for different diffusion times; the arrow indicates increasing diffusion time. F) ACFs if two different particles are present in equal amounts, and the diffusion time of first particle is set at a lower value; the arrow indicates increasing diffusion time of the second particle. G) Influence of the number of particles found in the triplet state on an ACF; the arrow indicates increasing fraction of triplet state.

2.1.3 FCS instrumentation

The instrumentation for FCS is nowadays widely commercially available. Nevertheless, new setups are being created in fast succession to allow researchers to customize their instruments to particular scientific questions or to allow the performance of novel experiments not possible with the less flexible commercial instruments (Bacia & Schwille, 2007; Hwang & Wohland, 2007; Liu et al, 2008a). In this work, a standard confocal FCS setup (Fig. 2.2) is used for all measurement and will be discussed in this section.

A FCS setup is essentially composed of four parts: the light source, the excitation, the detection and the data processing (Fig. 2.2). Firstly, the main light sources for FCS are lasers. Since FCS usually requires relatively little power (~100 μW or less for the confocal setup), almost all commercially available laser sources can be used and the choice of laser is mainly governed by required wavelength, beam quality, and cost. For two-photon excitation pulsed infrared lasers are necessary. The most common type is the Ti-Sapphire laser (Schwille et al, 1999a). These lasers are more costly but have the advantage of using IR light which allows much deeper penetration into tissues than lasers with wavelength in the visible range (Helmchen & Denk, 2005). Secondly, for confocal excitation, the laser beam is coupled into a microscope and focused by an objective into a diffraction-limited spot. A pinhole in the setup then acts as a spatial filter to reject out-of-focus light before detection. In this way a small confocal volume element less than one femtoliter is created. The confocal excitation scheme is versatile, gives 3D resolution and, when scanning the laser beam, can be used to image the sample and subsequently park the laser at any

spot to collect correlation functions at any desired point (Pan et al, 2007a). Thirdly, on the detection part, two types of detectors can be used for FCS: the photomultiplier tubes (PMT) and avalanche photodiodes (APD). Those detectors count the incoming photons and convert them into electric current. While PMTs can have faster response times than APDs, APDs have the higher quantum efficiency. As sensitivity is essential for biological application, APD detector is used for all measurements in this work. Lastly for data processing, the correlator counts the photons in increasing time lags and calculates the autocorrelation function in a semi-logarithmic timescale. Compared to linear correlation timescale, semi-logarithmic timescale reduces computation time to allow online calculation of ACFs, while reducing the noise for long correlation times (Schatzel et al, 1988). Since this scheme requires great speed they have been mainly realized by hardware correlators.

In the experimental realization, a commercial confocal laser scanning microscope FV300 (Olympus, Tokyo, Japan) was modified and combined with a custom-built FCS attachment. The laser beam from an air-cooled Argon ion laser (488 nm, Melle Griot, NM, USA) was controlled by an acousto-optic tunable filter. A laser power of 30 μW was used for most measurements in zebrafish embryos. The excitation light was reflected by an excitation dichroic mirror (488/543/633) and delivered into the scanning mirrors (G120DT, GSI Lumonics). A water immersion objective (UPLSAPO 60×, NA1.2, Olympus) then focused the laser beam into the sample (a water immersion objective is more suitable for biological applications, as the refractive index of biological tissue is usually 1.39 to 1.41 (Bolin et al, 1989), compared to 1.33

of water and 1.52 of immersion oil). The emitted fluorescence light was imaged over a 3× magnification stage onto a 150 µm pinhole, which results in a pinhole size of 50 µm. A custom-built slider then allowed one to direct the light to either the FV300 photomultipliers for imaging, or to the APD detector (SPCM-AQR-14-FC, Pacer, Berkshire, UK) for FCS analysis. The use of a single pinhole for both imaging and spectroscopy guaranteed the accurate positioning of the FCS observation volume in the sample after confocal imaging acquisition (Pan et al, 2007a). In the FCS detection part, an Achromatic lens (f=60 mm, Thorlabs, Newton, NJ) focused the fluorescence through band-pass filters (510AF23, Omega Optical, Brattleboro, VT for EGFP and 595AF60 for mRFP) onto the APD detector. Autocorrelation was computed online by a hardware correlator (Flex02-01D, Correlator.com, Bridgewater, NJ).

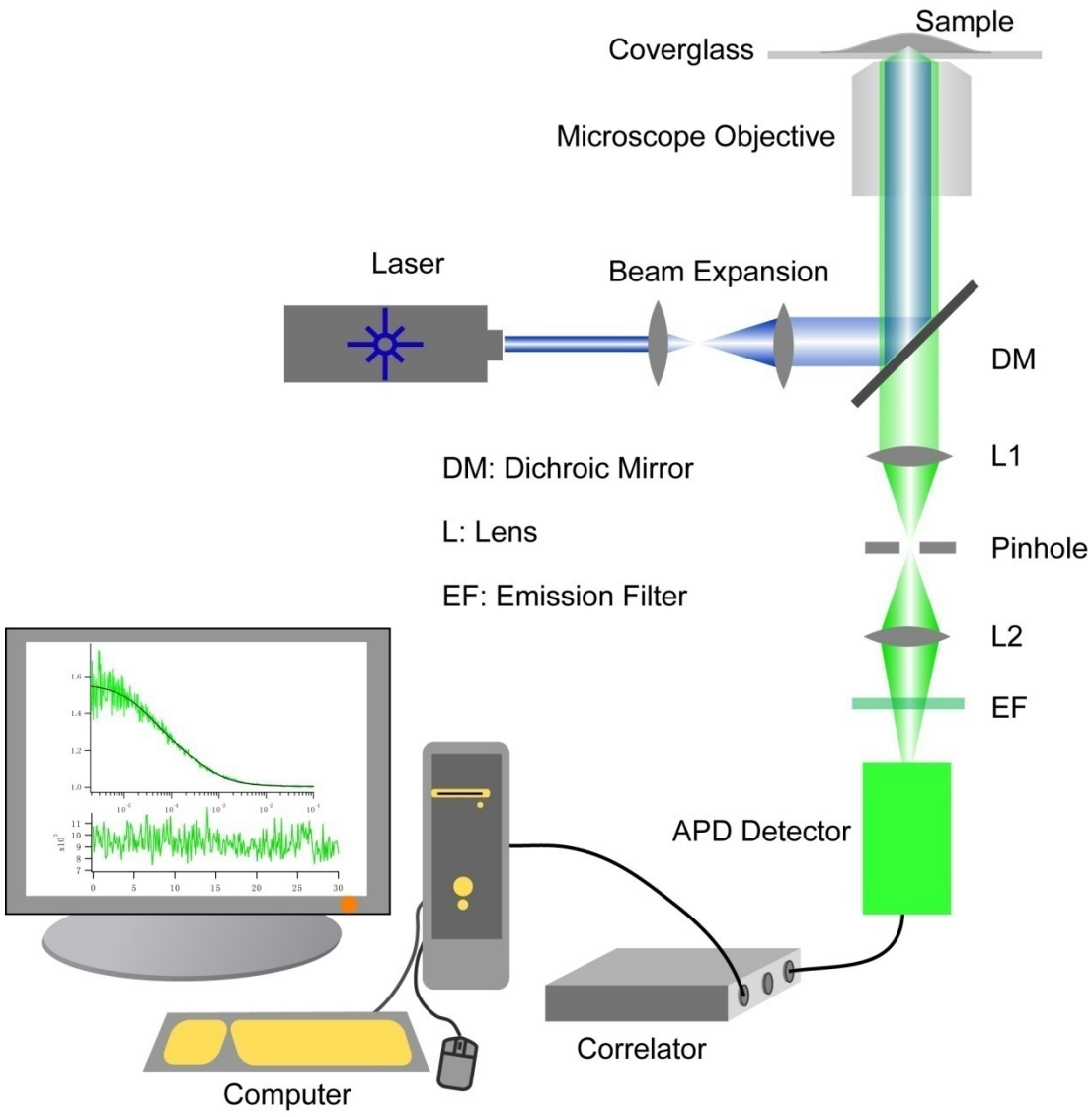

Fig. 2.2: A typical optical setup of confocal FCS. A laser beam is expanded and focused by a microscope objective into a fluorescent sample. The red-shifted fluorescence light is collected by the same objective and passes through the dichroic mirror. A pinhole at the conjugate plane then acts as a spatial filter to reject out-of-focus light. The fluorescence light passes through an emission filter and is finally focused onto an avalanche photodiode (APD) detector that counts the incoming photons. The autocorrelation function is then calculated online using a hardware correlator and the results are displayed on the computer.

2.1.4 Data Fitting

FCS data fitting is critical for extracting meaningful quantitative parameters. The raw autocorrelation data from experiments are analyzed by fitting with a defined correlation function models, such as one component, 3D diffusion model (Eq. 2.17) or two component, 2D diffusion with one triplet model (Eq. 2.27). New fitting models in FCS are constantly derived for a range of different situations giving researchers a much wider base with which to test their experimental curves. However, intracellular data usually cannot be described by a simple one component 3D or 2D diffusion, as fluorescence proteins (FPs) used for live cell labelling possess poor photophysical properties compared to organic dyes and the protein of interest can interact with a wide range of effectors when present at different physiological environments. Therefore a function describing the photodynamics of the fluorophore (Widengren et al, 1995) is usually introduced into the fitting function and a multi-component model or an anomalous diffusion model (Schwille et al, 1999b; Weiss et al, 2004) is used instead, e.g. Eq.2.27 for 2 dimension 2 particle 1 triplet model and Eq.4.1 for 3 dimensional 1 particle 1 triplet anomalous diffusion model. It should be noted that the addition of extra components into the fitting function usually yields a better fit because of the larger number of free parameters, but that does not necessarily provide more accurate data evaluation or more insight into the biological meaning of the data(Kim et al, 2007).

In this work, the raw data was fitted using the software Igor Pro (Wavemetrics Inc., Portland, OR) that performs an iterative procedure by the Levenberg-Marquardt algorithm to minimize the χ^2. The χ^2 measures the summation of all differences

between the fitted function y against the raw data y_i and is weighted by its standard deviation σ_i (Bevington & Robinson, 1992),:

$$\chi^2 = \sum_i \left[\frac{(y - y_i)}{\sigma_i} \right]^2 \tag{2.28}$$

In addition, global fitting can also be used for better parameter estimation (Skakun et al, 2005), and recently a new fitting algorithm, which improves data fitting and parameter accuracy, has been introduced (Rao et al, 2006).

2.2 Single Wavelength Fluorescence Cross-Correlation Spectroscopy

2.2.1 Introduction

As mentioned in Chapter 1, fluorescence cross-correlation spectroscopy (FCCS) can be used to specifically study protein-protein interactions. In FCCS two distinct fluorescently labelled molecules are excited by different lasers and detected separately by different detectors. By comparing the signal intensities between the two detectors in time via cross-correlation one can determine whether molecules move together in time and interact (Fig. 2.4). The first experimental realization of FCCS utilized two lasers to excite two different fluorophores (Schwille et al, 1997). This setup achieved high molecular brightness (also known as count rate per molecule per second (*cps*) and *cps* will be used in the following text) as each fluorophore is excited with a laser matching its absorption maximum. Fluorophores can also be selected to have widely separated emission maxima to minimize cross-talk. One limitation of dual laser excitation FCCS is the experimental difficulty of aligning and maintaining two laser beams to the same focal volume. This is complicated by chromatic aberrations and the differences of the focal spot size resulting from different wavelengths. The situation is even worse when applied in biological samples as cell comprises different subcellular compartments and macromolecules which make itself optically inhomogeneous (Cheong et al, 1990).

Laser misalignment in this case will cause reduced cross-correlation amplitudes and a shift towards slower decays (Weidemann et al, 2002), and this makes quantification almost impossible.

Single wavelength FCCS (SW-FCCS) uses one instead of two lasers to excite the different fluorophores by one-photon excitation (OPE). As one laser line is used to excite two fluorophores, system alignment is simplified and instrument stability is dramatically improved. Ricka and Binkert have reported for the first time excitation of one fluorescent and one scattering polystyrene beads with single wavelength to obtain auto- and cross-correlations (Rika & Binkert, 1989), and the first SW-FCCS was reported by Hwang and Wohland in 2004 (Hwang & Wohland, 2004). The experiment of single wavelength excitation is only feasible with fluorophores that possess similar excitation maxima but largely different Stokes shifts. In Hwang and Wohland's report, a ligand-receptor interaction was successfully monitored using OPE SW-FCCS, with particles labeled either with fluorescein or tandem dyes/Quantum Dots. The fluorophore pairs of fluorescein and QDs excited by 488 nm laser generate reasonable *cps* for FCCS analysis. The resolution of SW-FCCS was investigated with spectrally similar dyes (Hwang & Wohland, 2005) and contributions of sample concentration, impurities, labeling ratios, and spectral cross-talk to the results were discussed. Recently, *in vivo* SW-FCCS applications were presented in cell cultures (Liu et al, 2007; Sudhaharan et al, 2009) using fluorescent protein pairs of EGFP and mRFP (see Fig. 2.3 for excitation and emission spectra of EGFP and mRFP), and triple-color detection was achieved *in vitro* to probe higher order interactions (Hwang et al, 2006a). SW-FCCS simplifies the setup of dual laser

excitation FCCS with affordable and commercially available instruments and eliminates the potential artifacts that arise from laser misalignment.

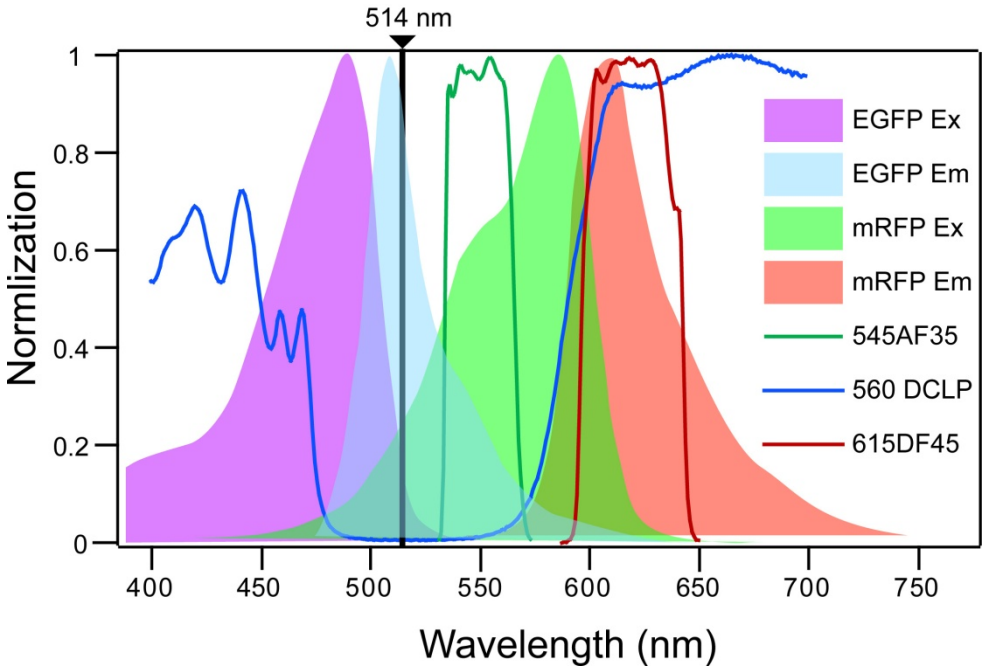

Fig. 2.3: Excitation and emission spectra of EGFP and mRFP, showing together with dichroic mirror and emission filters. It is feasible to excite both EGFP and mRFP at 514 nm and separately collect fluorescence signals at 545 nm for EGFP and 615 nm for mRFP.

2.2.2 Theory of SW-FCCS

In SW-FCCS, the binding partner are labelled with spectrally separated fluorophores and simultaneously excited by a single wavelength with OPE. Each label is separately detected, i.e. in green channel and red channel. Autocorrelation analysis is performed in each channel and yields information about the concentration and

the diffusion coefficient of each particle, while cross-correlation is carried out between the two channels (Fig.2.4). The normalized cross-correlation function (CCF) is written as

$$G_x(\tau) = \frac{\langle F_g(t) \cdot F_r(t+\tau) \rangle}{\langle F_g(t) \rangle \langle F_r(t) \rangle} \tag{2.29}$$

where $G_x(\tau)$ represents the cross-correlation of signals between green and red channel, $F_g(t)$ and $F_r(t)$ represent the fluorescence intensities in the green and red channel, respectively. As described previously in **2.2.1**, a $G_x(\tau)$ >1 therefore indicates that two particles are correlated. In FCCS, this means that the two particles are bound to each other, thus possess concurrent movement. FCCS therefore determines molecular binding based on the amplitude of the cross-correlation curve independent of mass (Fig. 2.4).

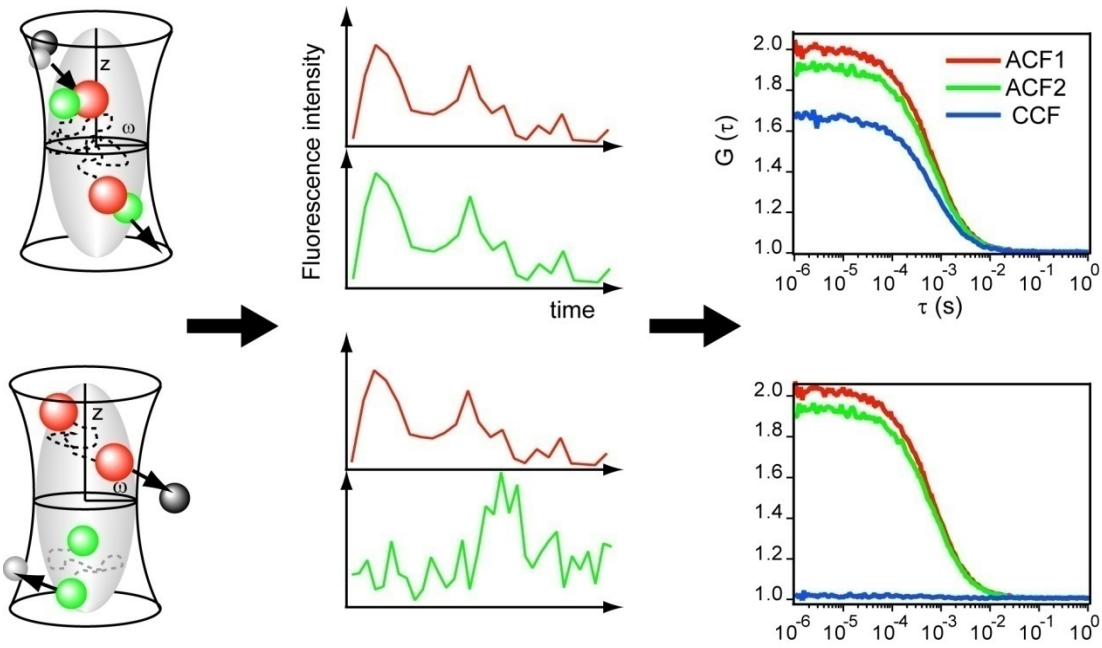

Fig. 2.4: Theory of FCCS. A typical FCCS measurement yields three correlation functions, two ACFs, one for each channel, and one cross correlation function (CCF). A) If the two differently labeled particles do interact, then the ACFs give the concentration of the two species and the CCF gives the concentration of interaction particles. B) If the two differently labeled particles are not interacting, then the ACFs give the concentrations and diffusion coefficients of the two species, but the CCF is flat. In addition, the ACFs will contain the diffusion coefficient of free and interactions particles, while the CCF will give the diffusion coefficient of the interacting particles.

Assuming a 1:1 binding stoichiometry, the molecular reaction is described as:

$$G + R \rightleftharpoons GR \tag{2.30}$$

where the *G*, *R* and *GR* represent the green particle, the red particle and the green-red complex, respectively. The fluorescence intensity in the green and red channel can thus be described as the product of the *cps* of each particle times the number of particle in the effective volume ($\eta \cdot N_A \cdot V_{eff} \cdot C$):

$$F_g = N_A V_{eff}\left[\eta_g^g C_g + \eta_r^g C_r + \left(\eta_g^g + \eta_r^g\right) C_{gr}\right] \tag{2.31}$$

$$F_r = N_A V_{eff}\left[\eta_r^r C_r + \eta_g^r C_g + \left(\eta_r^r + \eta_g^r\right) C_{gr}\right] \tag{2.32}$$

where C_g, C_r and C_{gr} are the concentrations of the free green, free red and the complex particles respectively; η_g^g and η_r^g are the *cps* of green and red particles in the green channel respectively; η_g^r and η_r^r are the *cps* of green and red particles in the red channel respectively; N_A is the Avogadro's number; V_{eff} is the effective observation volume.

The amplitude of the ACFs and CCF can thus be expressed as a function of the *cps* and the concentration of the particle involved (Hwang & Wohland, 2005; Liu et al, 2007):

$$G_g(0) = \frac{(\eta_g^g)^2 C_g + (\eta_r^g)^2 C_r + (q_g\eta_g^g + q_r\eta_r^g)^2 C_{gr}}{N_A V_{eff}[\eta_g^g C_g + \eta_r^g C_r + (q_g\eta_g^g + q_r\eta_r^g) C_{gr} + \beta^g/(N_A V_{eff})]^2} \tag{2.33}$$

$$G_r(0) = \frac{(\eta_g^r)^2 C_g + (\eta_r^r)^2 C_r + (q_g\eta_g^r + q_r\eta_r^r)^2 C_{gr}}{N_A V_{eff}[\eta_g^r C_g + \eta_r^r C_r + (q_g\eta_g^r + q_r\eta_r^r) C_{gr} + \beta^r/(N_A V_{eff})]^2} \tag{2.34}$$

$$\begin{aligned} G_x(0) = {} & \frac{\eta_g^g\eta_g^r C_g + \eta_r^g\eta_r^r C_r + (q_g\eta_g^g + q_r\eta_r^g)(q_g\eta_g^r + q_r\eta_r^r) C_{gr}}{N_A V_{eff}[\eta_g^g C_g + \eta_r^g C_r + (q_g\eta_g^g + q_r\eta_r^g) C_{gr} + \beta^g/(N_A V_{eff})]} \\ & \times[\eta_g^r C_g + \eta_r^r C_r + (q_g\eta_g^r + q_r\eta_r^r) C_{gr} + \beta^r/(N_A V_{eff})]^{-1} \end{aligned} \tag{2.35}$$

where $G_g(0)$ and $G_r(0)$ are the amplitudes of the ACF in the green and red channel respectively, and $G_x(0)$ is the amplitude of the CCF; β^g and β^r are the uncorrelated background count rate in the green and red channels respectively; q_g and q_r are correction factors that account for changes in fluorescence yields upon binding via

processes such as quenching or fluorescence energy transfer for the green and red particles respectively;

The value of $G_g(0)$, $G_r(0)$ and $G_x(0)$ can be obtained directly from fitting the two ACFs and the CCF of the SW-FCCS measurement. The *cps* of each particle, the uncorrelated background count rate, and the correction factors can also be obtained through calibration of the system. Thus there are only three unknown parameters (C_g, C_r and C_{gr}) in Eq. 2.31, Eq. 2.32 and Eq. 2.33 and it is possible to numerically solve the equations and obtain the value of C_g, C_r and C_{gr}.

2.2.3 Binding Quantification

In intracellular experiments, the relative expression levels between the green and red tagged proteins are difficult to control precisely. Hence the percentage of bound molecules is expressed as a function of the total concentration of either the total green or total red molecules as defined:

$$\frac{C_{gr}}{C_g + C_{gr}} \times 100 \text{ or } \frac{C_{gr}}{C_r + C_{gr}} \times 100 \tag{2.36}$$

For example, in a measurement where the green tagged molecules are less than the red tagged molecules, the first form will be used and vice versa since the molecule of lower concentration limits the number of possible complexes. In measurements, it is also wise to pick cells with expression levels which differ by no more than a

factor of 2 for both proteins. When a significant difference in the complex percentage is observed between the experiment and a negative control (co-expression of two nonbinding fluoropores), an interaction is thought to be present. The value of this complex percentage gives a general idea of the strength of interaction of the molecules when compared with a positive control (a tandem construct where two fluorophores are bound together), which gives the upper limit of the complex percentage. A better and more exact measure is the dissociation constant K_D defined as:

$$K_D = \frac{C_g \times C_r}{C_{gr}} \tag{2.37}$$

The dissociation constant K_D at equilibrium is not affected by the relative concentration of the two interacting particles.

2.2.4 SW-FCCS Instrumentation

In experimental realization, the instrumentation of SW-FCCS is essentially the same as FCS described in **2.1.3**, except that in the detection part, two detectors were set up for the detection of two fluorescence emissions (Fig. 2.5). The laser excitation is also the same as that of FCS setup since only one laser line was chosen to excite two fluorophores. The 514 nm laser line from an argon ion laser (Spectra-Physics, Mountain View, CA) was used to excite the combination of EGFP and mRFP (Fig. 2.3).

The dichroic mirror to reflect the laser beam was 525DRLP (Omega Optical, Brattleboro, VT). After the pinhole a second dichroic mirror, 560DCLP (Omega Optical), was placed to separate the fluorescence emissions of the two FPs. Accordingly, two bandpass filters, 545AF35 (Omega Optical) and 615DF45 (Omega Optical), were placed in front of the two APDs (SPCM-AQR-14-FC, Pacer, Berkshire, UK) as emission filters. The autocorrelations and the cross-correlation were all performed by the same hardware correlator (Flex-02-12D, correlator.com, Zhejiang, China), and the curves fitting were performed using Igor Pro software (Wavemetrics Inc. Portland, OR).

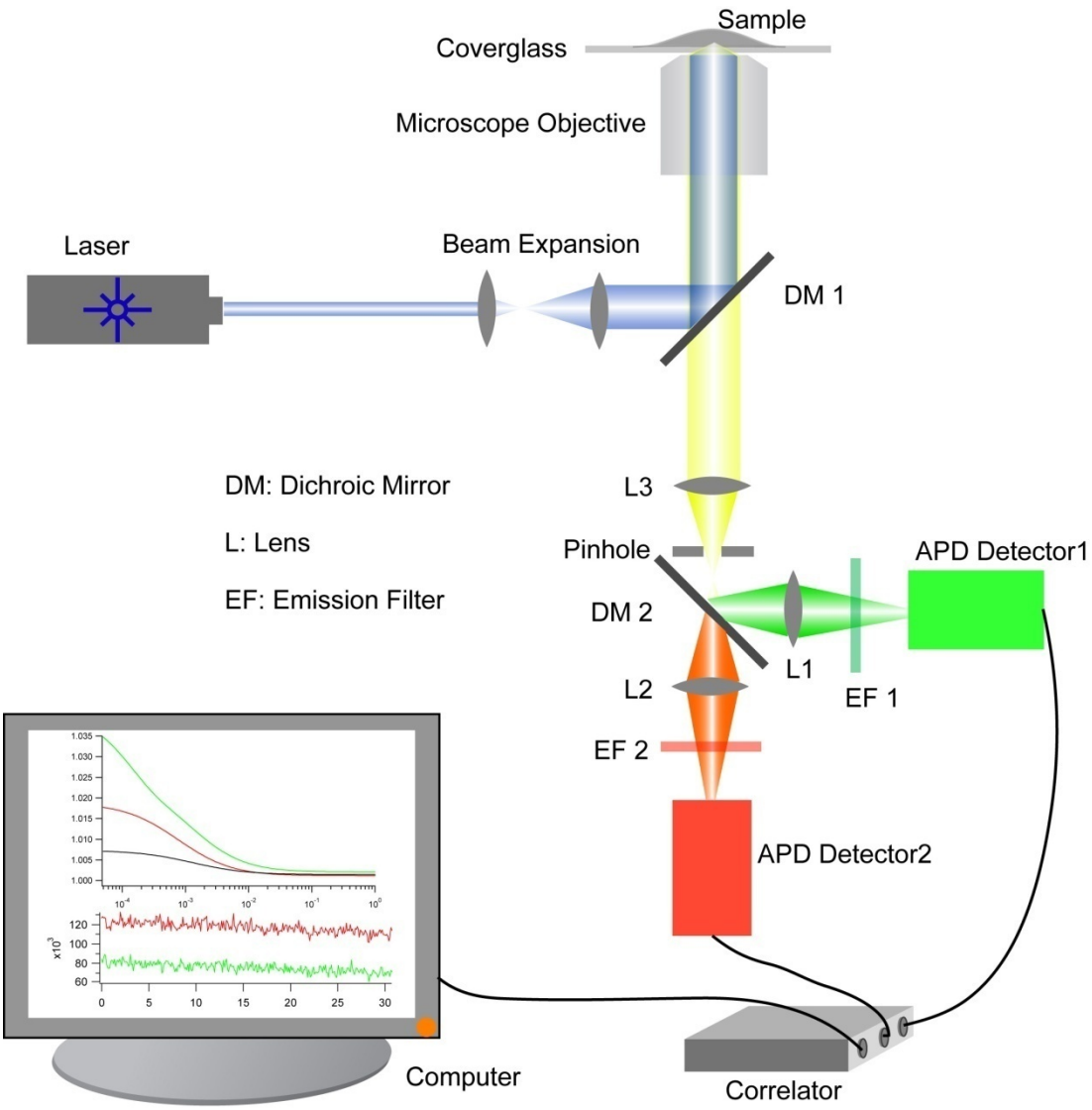

Fig. 2.5: A typical optical setup of SW-FCCS. A single wavelength laser is expanded and focused by a microscope objective onto a fluorescent sample. The fluorescence light is collected by the same objective and passes through the dichroic mirror. A pinhole at the conjugate plane then acts as a spatial filter to reject out-of-focus light. A second dichroic mirror is placed after the pinhole to separate the signals into green and red channels. The green and red fluorescence signals pass through two emission filters and are finally focused onto two APD detectors that count the incoming photons. The autocorrelation and cross-correlation functions are then calculated online using the same hardware correlator and the results are displayed on the computer.

2.3 Preparation of Zebrafish Embryos for Imaging and SW-FCCS Measurements

2.3.1 Zebrafish Embryo Preparation

Zebrafish were maintained at 28.5 °C according to the zebrafish book (Westerfield, 2000), the IACUC regulations and rules of the IMCB zebrafish facility. Zebrafish are photoperiodic in their breeding, and produce embryos every morning. In general, a pair of adult AB zebrafish were well fed and separated by a plastic slider at day 1 afternoon (the zebrafish AB line was use as a wild type fish). The slider was removed at day 2 morning and embryos were produced. One-cell stage zebrafish embryos were collected and kept in egg water. Dechorination was performed using two sharp needles and the dechorinated embryos were transferred to a Petri dish with moulded agarose injection holder (Fig. 2.6). The orientation of the zebrafish embryos was adjusted using a glass dropper so that the animal poles were on top. Extreme care should be taken as embryos at this stage are fragile. 100 pL of designated DNA plasmid (100 ng/μL) was injected into a single blastomere at 16-cell stage using a manual injection machine (nanoinjector, WPI, USA) and a stereomicroscope (Olympus, Japan). The embryos were then incubated in egg water at 28.5°C for optimal development, and PTU (0.003% 1-phenyl-2-thiourea in 10% Hank's saline, Invitrogen, Singapore) was added day 3 at 18 hours post fertilization (hpf) to prevent pigmentation. (Suppression of pigmentation is very important for fluorescence based observations, as melanin, the pigment found in the epidermal layer of skin, has a large scattering coefficient in the ultraviolet (UV) region, which

protects the skin from damaging UV radiation from the sun, and a significant absorption coefficient in the NIR region (Meglinski & Matcher, 2002).) Fluorescence expression was examined at 48 to 72 hpf under a UV dissecting microscope and embryos with normal development and low expression level in proper cell lines were selected for FCS measurements. Selected embryos were anaesthetized using Tricaine (ethyl-3-aminoboenzoate, Sigma, Singapore) and mounted in 0.5% low-melting-temperature agarose (Invitrogen) in a glass bottom Petri dish (GW-3512, WillCo-Wells, Amsterdam, Netherlands). The Petri Dish containing the zebrafish embryo was then mounted in the fluorescence correlation microscope (FCM) for confocal imaging and FCS/SW-FCCS measurements.

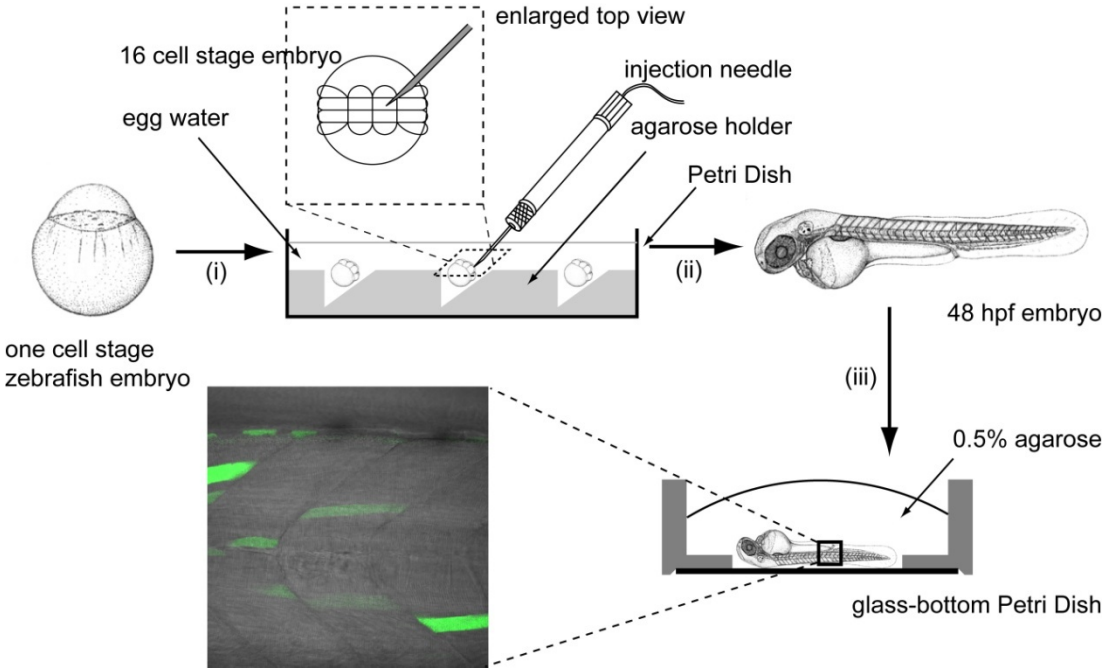

Fig. 2.6: Zebrafish embryo preparation (i) one-cell stage embryos were collected and dechorionated. The embryos were aligned onto the agar holder in a Petri Dish and the orientation of the embryo was adjusted such that the animal pole was on top. The Petri Dish was filled with egg water and the embryos were allowed to develop to the 16 cells stage. (ii) The DNA plasmid was microinjected into one of the four central blastomeres. The embryos were then incubated in egg water at 28.5 °C to develop to 3 dpf. (iii) Selected embryos were anaesthetized and mounted into 0.5% low-melting-temperature agar in a glass bottom Petri dish. The embryo body was pushed close to the surface of cover glass and the orientation of the embryo was adjusted with a needle. The specimen was then mounted in the microscope stage for subsequent confocal imaging and FCS measurements.

2.3.2 Imaging and FCS/SW-FCCS Measurements of Zebrafish Embryos

The custom-built FCM allows one to obtain an image of the sample first before identifying a position on the image where subsequent FCS measurements could be performed. The single pinhole design (Fig. 2.5) for both imaging and spectroscopy guarantees the accurate positioning of the FCS observation volume after confocal image acquisition (Pan et al, 2007a). In general, a 10× objective (UPLSAPO, NA=0.40, Olympus, Japan) was used to obtain an overview of the FPs expression. Region of interest was selected based on the overview and a 60× objective (UPLSAPO, water immersion, NA=1.20, Olympus) was then used to focus on single cell. A 4 to 8 times digital zoom usually is required for small cells such as motor neurons (Fig. 2.7). It should be noted that FCS has a limited working distance inside the embryo tissue (discussed at section **3.4**), so cells of interest are usually chosen within 50 µm from embryo body surface. When a cell of interest is in focus, a single spot is then chosen inside the cell for point scanning and the custom-built slider then switches the system for FCS measurements.

In FCS measurements, the standard deviation of the ACF is proportional to the square root of the total measurement time (Kask et al, 1997; Wohland et al, 2001). Thus longer measurement times will improve the quality of the measurement, e.g. a 4 times longer measurement will decrease the standard deviation by a factor of 2. However, in biological samples, fluorescence proteins (FPs) are usually used to genetically label proteins (Campbell et al, 2002a; Shaner et al, 2004; Tsien, 1998),

and FPs have in general poor photophysical properties compared to organic dyes and are prone to photobleaching upon long periods of laser excitation. Considering these factors, a measurement time of 30 seconds was used for all measurements in zebrafish embryos.

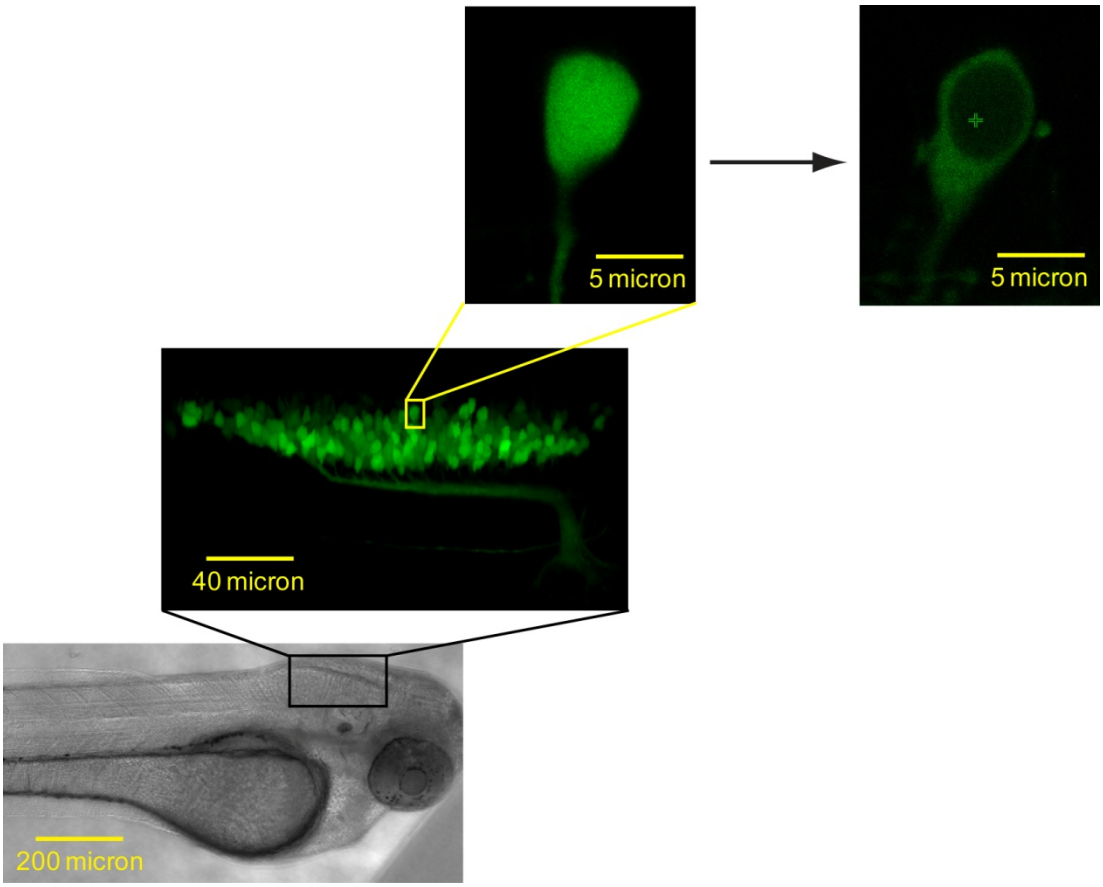

Fig. 2.7: Identification of a single cell and subcellular compartment in zebrafish embryo. At the bottom is a 48 hpf *islet-1*-EGFP zebrafish embryo, transmission channel, dorsal view. A population of vagal motor neurons can be viewed in the fluorescence channel as shown in the middle picture. A single motor neuron cell can be selected from the population by a 60× objective with another 4 to 8 times zoom. Subcellular compartments such as the nucleus can be identified by performing a point photobleaching. As the EGFP molecules cannot diffuse fast enough through the nuclear envelop, a point photobleaching thus results in the formation of a boundary between cytoplasm and nucleus.

2.4 Preparation of biological samples

Four protein constructs were used in this work: Cxcr4b-EGFP, mRFP-Cdc42, EGFP-IQGAP1, and mRFP-EGFP.

Cxcr4b is a chemokine receptor of the G-Protein Coupled Receptor (GPCR) gene family (Chong et al, 2001; 2009; 2007). These seven transmembrane domain receptors play an important role in defining directionality of cell migration of germ cells, lateral line, and somites during embryogenesis (Doitsidou et al, 2002; Gilmour et al, 2004; Hollway et al, 2007). In our experiments, the Cxcr4b (TAG to GGG) gene without stop codon was previously cloned in a pPCR-Script vector (Clontech, CA, USA) at the *SrfI* restriction enzyme site (Chong et al, 2007). The Cxcr4b fragment was released using *SacII* and *XhoI* (New England Biolabs, Ipswich, MA) and then subcloned into pEGFP-N1 (Clontech) vector digested with the same enzymes. The Cxcr4b-EGFP construct was sequenced and membrane expression in zebrafish embryo was confirmed by confocal imaging.

Cdc42 is a small GTPase that belongs to the Rho/Rac subfamily and it regulates various cellular responses including the assembly and disassembly of the actin cytoskeleton (Heasman & Ridley, 2008). It interacts with over 20 target proteins identified to date, including IQGAP1 (Erickson et al, 1997), a multidomain scaffolding protein that modulates cross-talk among diverse pathways. Two Cdc42 mutants were used in this study: the constitutively active $Cdc42^{G12V}$ which is in a predominantly GTP-bound form and the dominant-negative GDP-bound $Cdc42^{T17N}$. The Cdc42 related plasmid construct was made by my colleague Foo Yong Hwee.

The constitutively active mutant $Cdc42^{G12V}$ and the dominant-negative mutant $Cdc42^{T17N}$ of Cdc42 were sub-cloned into an mRFP1-pXJ40 vector at the C-terminal of mRFP1 between the *BamHI* and *NotI* sites. The pEGFP-C2-IQGAP1 vector was a gift from Prof. Kozo Kaibuchi (Nagoya University Graduate School of Medicine, Nagoya, Japan).

The tandem construct of mRFP-EGFP served as a positive control. The EGFP from a pEGFP-C3 vector (Clontech, CA) was sub-cloned into the mRFP1-pXJ40 vector at the C-terminus of mRFP1 between the *BamHI* and *NotI* sites bridged by a 7 amino-acid linker (-GSRMGTG-) to form the positive control.

Chapter 3

Zebrafish embryo as a model for FCS measurements

3.1 Introduction

The zebrafish, *Danio rerio*, as a vertebrate model is widely used in the study of development and genetics. Zebrafish has previously been a popular tropical fish pet for decades, and its use for scientific research came only very recently, following the demonstration that it is the first vertebrate animal model amenable to large-scale forward genetic screens (Eisen, 1996). Using zebrafish, it is possible to take a forward genetic approach to study vertebrate-specific processes that affect development and disease. The whole zebrafish genome has been sequenced, and gene function can be specifically studied using antisense techniques (Heasman, 2002; Nasevicius & Ekker, 2000). These tools and others have made zebrafish the organism of choice for many areas of research (Berghmans et al, 2005; Pyati et al,

2007; Shin & Fishman, 2002; Zon & Peterson, 2005). In particular, people are aware that zebrafish can also be a vertebrate model for cell biological-based research (Beis & Stainier, 2006). This is facilitated by the optical transparency of the zebrafish embryos and early larvae, which makes possible direct visualization of cells and organs deep within body. The transparent zebrafish embryo body means less light blockage by the tissue in the spectrum visible to human eyes, which is in the 380 to 750 nm wavelength range. This wavelength range covers the excitation and emission spectra of most commonly used fluorophores, aiding the application of fluorescence microscopy and spectroscopy. In this work, we investigated the feasibility of studying molecular dynamics in living zebrafish embryos using FCS/SW-FCCS. Compared to Petri dish-based cell culture, which is conventionally used for cell biology research, zebrafish embryo is advantageous (see discussion in **Chapter 1**) and provides a platform to investigate a wider spectrum of biological questions. However, the experimental realization of applying FCS/SW-FCCS in living zebrafish embryo is practically challenging due to intricate sample handling, uneven distribution of autofluorescence and thick tissue penetration. Consequently, the application of FCS is restricted to limited embryonic stages, areas and penetration depth. In this chapter, these factors are investigated, providing a guideline for further experiments.

3.2 Gene Expression in Zebrafish Embryos

One could use stable zebrafish transgenic lines to perform FCS measurements. However, those transgenic lines are usually made to express green or red FPs in certain tissues for the purpose of visualization only. FCS probes protein dynamics on the molecular level thus measurement of the transgenic line gives only the parameters of the green or red FPs. To introduce a protein-of-interest into the embryo body, microinjection of mRNA or DNA constructs is required. The mRNA has the advantages of early expression and more precise control of expression levels. However, mRNA is short lived and cannot sustain protein expression to late embryonic stages. As we focused FCS measurements on motor neuron cells and muscle fiber cells in 2 to 3 days old zebrafish embryos in this work, DNA constructs were used instead of mRNA. It should be noted that using DNA constructs EGFP can only be stably expressed in zebrafish embryos after 24 hpf, and this sets the earliest time point that FCS can be performed (New GFP variants with faster maturation time became available recently: http://www.clontech.com). On the other hand, FCS measurements can be performed up to 5 dpf and after that, increased pigmentation hinders any light based application.

In this work, the controlled amount of DNA plasmid was microinjected into one blastomere at 16-cell stage zebrafish embryos (Fig. 2.6). This practice provides a general control when protein needs to be expressed in different cell types within the embryos. Furthermore, injection at 16-cell stage reduces the number of cells

that express the foreign gene, which could be cytotoxic to the embryo. In general, the protein expression level should always be kept low, especially for those physiological functional ones. In one example, we injected the DNA encoding *the* epidermal growth factor receptor (EGFR) gene, and all embryos were dead within one day even with half than the usual injection amount. The transfection of the same plasmid in Chinese hamster ovary (CHO) cells show no such effects (Liu et al, 2007). This reinforces the concept that the 2D cell culture could survive more stringent environment but the information obtained at this condition may be less physiologically relevant. In order to express physiologically functional proteins in zebrafish embryos, one could further reduce the injected DNA amount, inject mRNA instead, or use a tissue specific promoter to drive protein expression.

In the following experiments, muscle fiber cells were chosen for FCS/SW-FCCS measurements as they are abundant within the embryo and are easy to identify. The mosaic expression pattern of injected plasmid in the embryo body also provides cells with different protein expression level to choose from. Based on confocal images, muscle fiber cells that express injected plasmids at physiological levels (nanomolar range) were selected for FCS/SW-FCCS measurements.

Compared to cell culture, gene expression in zebrafish embryos requires more manual work. But each successfully microinjected embryo provides dozens to hundreds of cells for observation. No CO_2 incubator is required and each cell is maintained in a genuine physiological environment. In addition, DNA delivery in zebrafish embryo using electroporation has been developed (Teh et al, 2003), so that protein activity can be directly studied at specific embryonic stages while

leaving earlier functions intact. Thus zebrafish is well suited for cell-biological based protein dynamic studies and it provides a platform to investigate a wider spectrum of biological questions.

3.3 Autofluorescence Study

3.3.1 Introduction

One advantage of FCS is the extreme sensitivity down to the single molecule level (Rigler et al, 1993b). This requires high signal to noise ratio of the sample and minimal background interference. However, autofluorescence in live cells and tissues is inevitable (Andersson et al, 1998) and it is generally considered as one of the major problems encountered in ultrasensitive FCS applications. As shown by Koppel (Koppel, 1974), the signal to noise ratio of FCS measurements is governed by the number of photons collected per fluorophore per sampling period (*cps*). In experiments, one would like to minimize the *cps* of the autofluorescence while maximizing the *cps* of the fluorophore-of-interest. Therefore, it is necessary to study the distribution and the emission spectrum of the autofluorescence in the embryo body, aiming to choose region of less autofluorescence and select proper filter sets fit for FCS application.

In principle, a fluorescence background from immobile autoflurescence will give no autocorrelation. In this case, the steady background introduces a constant error factor at all time scales in the autocorrelation curve which leads to decreased amplitude value. This causes overestimation of the concentration of the fluorophore-of-interest but does not affect the temporal information. However, it has been shown that autofluorescence in various cell lines, including A431 human

epidermoid carcinoma cells and HeLa cells, produce autocorrelation amplitudes (Brock et al, 1998; Schwille et al, 1999a), which may rise from mobile native fluorophores stable enough to be correlated themselves. Known intrinsic biological autofluorescent molecules include flavoproteins, collagen, NADH, lipofusion, and elastin (Schwille et al, 1999a). Therefore, it is necessary to examine whether autofluroescence in zebrafish embryo gives autocorrelation amplitude.

3.3.2 Autofluorescence distribution in embryo body

We first examined the autofluorescence distribution in the living zebafish embryos. As EGFP and mRFP were the main fluorophores used in this work, laser lines of 488 nm and 543 nm were chosen to excite autofluorescence of a wild type AB zebraifsh embryo, respectively. We focused on embryos around 3 days post fertilization (dpf) and subsequent FCS measurements were performed at the same stage. An LSM 510 Meta (Carl Zeiss, Germany) confocal microscope was used for all autofluorescence studies. To obtain an overview of the autofluorescence distribution in the green channel, a 10× objective (Plan-Neofluar/NA=0.3, Carl Zeiss) and Long-Pass 505 emission filter were chosen to record fluorescence images excited by 488 nm laser line (100 µW) as shown in Fig. 3.1A. It is clear that the autofluorescence in the green channel was mainly concentrated in the yolk to yolk extension (arrow 2), and was also relatively strong in the region around the eyes (arrow 1). In comparison,

autofluorescence at the trunk region (arrow 3) is much lower (Fig.3.1B). The same embryo was then excited by 100 µW 543 nm laser and the image was recorded using a Long-Pass 560 emission filter as shown in Fig. 3.1C. The image suggests that autofluorescence in the red channel is equally strong in the yolk to yolk extension (arrow 2) and region around the eyes (arrow 1), while autofluorescence in the trunk region (arrow 3) is much lower (Fig 3.1D). To minimize the influence of autofluorescence in both green and red channels, the subsequent FCS measurements were conducted in the trunk region posterior to midbrain, where the main tissues are the epidermis, muscle, vascular and neuronal system. In addition, the result suggests that the overall autofluorescence intensity is slightly stronger in the red channel than the green channel. Therefore for single color application, EGFP was used as the fluorescence marker.

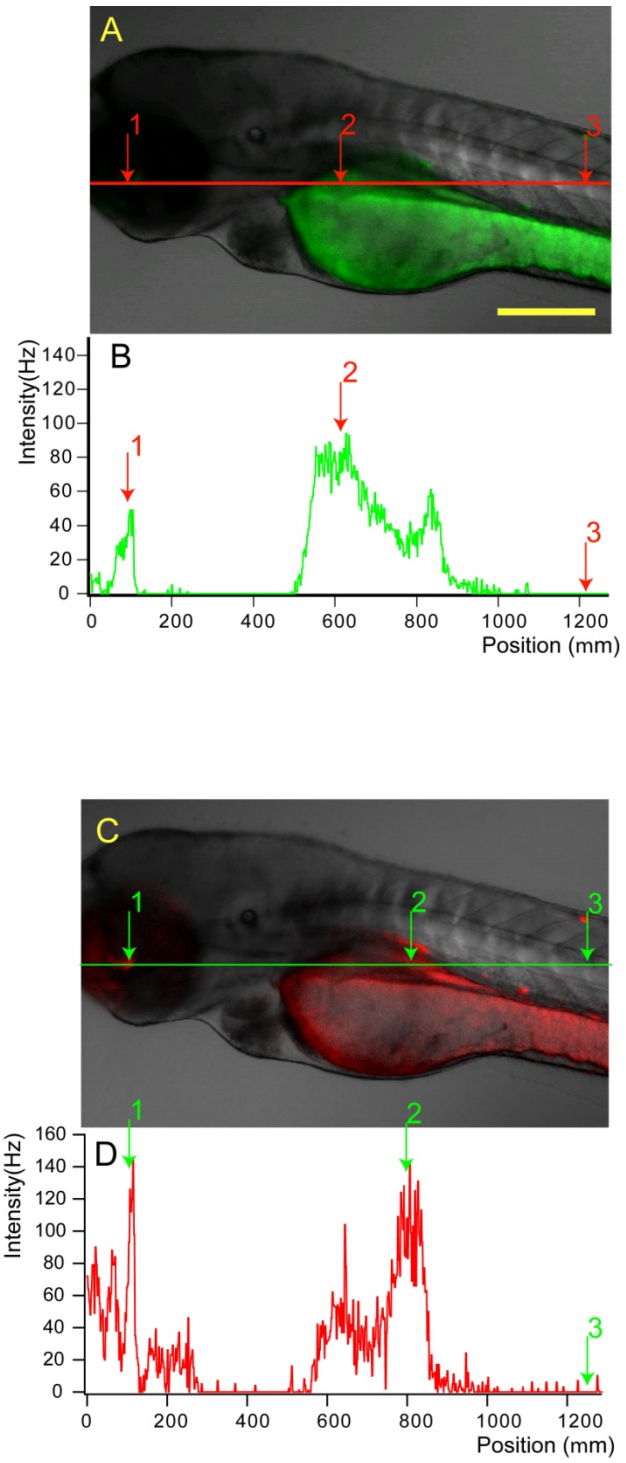

Fig. 3.1: Autofluorescence distribution in zebrafish embryo body. A) Overview of autofluorescence expression in lateral view 3 dpf AB wild type embryo, excited with 100 µW 488 nm laser, long-pass 505 as emission filter. Overlay of transmission and fluorescence channel. Embryo was treated with PTU at 18 hpf to prevent pigmentation. Scale bar = 200 µm. B) Fluorescence intensity trace of the red line in A). C) Overview of autofluorescence expression of the same embryo, excited with 100 µW 543 nm laser line, long-pass 560 as emission filter. D) Fluorescence intensity trace of the green line in C).

3.3.3 Autofluorescence Spectrum

The Zeiss LSM 510 Meta system has a 32 PMT array detector for parallel acquisition. Using it together with a diffractive element, one could capture the fluorescence emission spectrum of the sample. Here, we studied the autofluorescence emission spectrum excited with 100 µW 488 nm laser in a muscle fiber cell at the trunk region. A 40× objective (Plan-Neofluar/NA=0.75, Carl Zeiss) was used for this purpose and the spectrum was recorded from 505 nm to 719 nm in minimum steps of 10.7 nm (22 PMT elements were used in this case). Fig. 3.2 shows the normalized autofluorescence spectrum together with the EGFP spectrum and the 510AF23 emission filter (Omega Optical, Brattleboro, USA) used for FCS measurements. The autofluorescence peaked at 570 nm and 630 nm which is distinct from EGFP (maximum at 509 nm). Thus the 510AF23 emission filter can efficiently block most of the autofluorescence signal and pass the EGFP signal.

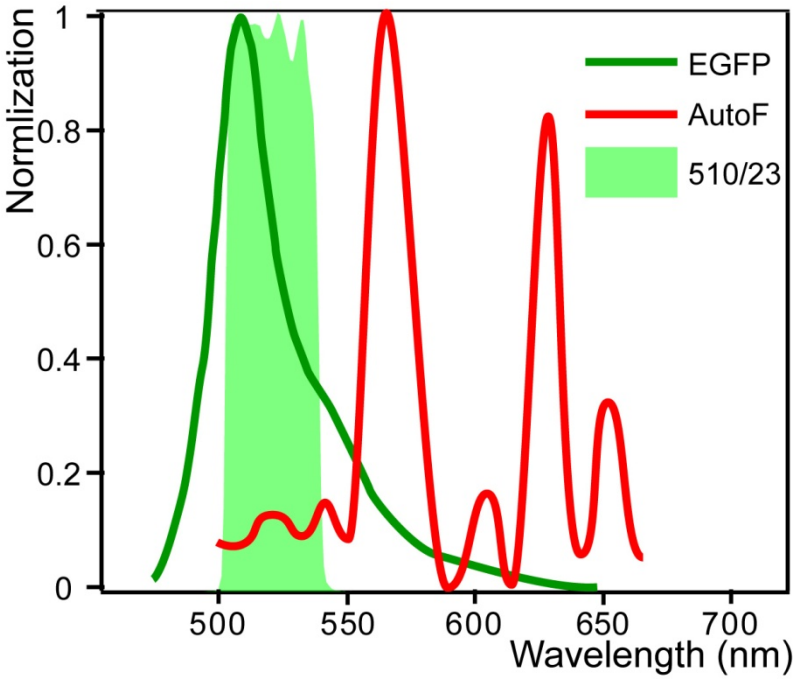

Fig. 3.2: Autofluorescence spectrum. Normalized autofluorescence spectrum taken in a muscle fiber cell in the trunk region, excited with 100 µW 488 nm laser. The autofluorescence spectrum is shown together with the EGFP emission spectrum and 510AF23 emission filter.

3.3.4 Autoflurescence Intensity

We finally performed FCS measurements with autofluorescence alone in zebrafish embryos. The observation volume was positioned in both the muscle fiber cell at trunk region and the motor neuron cell at hindbrain, and no autocorrelation was observed with autofluorescence alone in both cases. In contrast, FCS measurements in EGFP expressing muscle fiber cell and motor neuron cell generate robust autocorrelations with *cps* values around 6 kHz at the same laser excitation power of 30 µW. Autofluorescence (excluding region from blood vessel fluid and skin) did not

generate any autocorrelations and thus contributes only as background noise. The background signal adds to the overall fluorescence intensity of the FCS measurements and thus decrease the ACF amplitude *G(0)* as discussed in **2.1.1**. This leads to an overestimation of the concentration of the target molecules, but it does not affect the width of the autocorrelation function and thus the temporal information. At a point excited with 30 µW at 488 nm, the autofluorescence intensity (defined as count rate per second) recorded by the avalanche photodiode detector was 0.6 - 1 kHz in the zebrafish embryo trunk region (excluding skin and vascular system), compared to 0.2 – 0.6 kHz in buffer solutions in our calibration. This value was considerably smaller than that in the cell cultures (Brock et al, 1998; Schwille et al, 1999a). Nevertheless, in order to discriminate against autofluorescence background but still allow reliable fluctuation analysis, one should still optimize the excitation laser power and choose cells with proper fluorescent probe concentration.

High laser power is known to cause saturation and photobleaching of fluorophores (Dittrich & Schwille, 2001; Petrasek & Schwille, 2008a), especially for FPs, and sometimes even cause visible damage to the cell. Therefore, the intensity level in intracellular FCS applications should be kept far below the values commonly used in aqueous samples. In the following experiments, a 30 µW of laser power was used as an upper limit for one photon excitation FCS.

When selecting cells with different EGPF expression levels for FCS measurements, it has been suggested to use at least ten-fold higher probe concentrations in order to discriminate against autofluorescence (Schwille et al, 1999a; 1999b). Therefore

considering 1 kHz of autofluorescence intensity and accepting 10% of contribution of autofluorescence to the overall fluorescence intensity, EGFP-expressing cells with fluorescence intensity larger than 10 kHz were chosen for FCS measurements, which corresponds to 2 to 5 nM EGFP concentration depending on the *cps* of EGFP in the above mention experimental condition (*cps* value varies at different tissue depth penetration, see section **3.4.3** for detail). As an ultrasensitive tool, FCS works better with low probe concentration and an upper limit of probe concentration is usually 1 µM in solution (Thompson, 1991) and 100 nM in intracellular applications (Schwille et al, 1999a). Taking all these into consideration, EGFP-expressed cells with fluorescence intensity of 10 to 200 kHz were chosen for FCS measurements when excited with 30 µW 488 nm laser power.

Unlike cell cultures which are usually engineered from opaque tissues, the optically transparent zebrafish embryo is advantageous in terms of autofluorescence interference. We noticed that all strong autofluorescence observed in the zebrafish embryo arose from the less transparent regions, including eyes and yolk. By choosing for measurements the more transparent trunk region, the influence of autofluorescence was minimized and experiments can be done *in vivo* leaving the embryo intact at the end of measurements. Therefore working with larvae of fish strains where pigmentation is suppressed genetically (e.g. *albino*) or by chemicals (PTU), such measurements could be repeated during development of the same animal several times.

3.4 Penetration Depth Study

3.4.1 Introduction

Although the optical transparency aids FCS applications, the thick tissue still limits the working distance within the embryo at which the measurements could be performed efficiently due to the strong and multiple light scattering. In biological tissues, light absorption is generally negligible compared to light scattering (Helmchen & Denk, 2005), with one exception of melanin, the pigment in the epidermal layer of skin which has a significant absorption coefficient in NIR region (Meglinski & Matcher, 2002). Light scattering describes the deflection of a light ray from its original direction. Light scattering in biological tissue, also known as elastic scattering as the photon energy stay unchanged after deflection, is caused by the heterogeneities of cells, as cells comprise different sub-compartments and macro-molecules with varying molecular polarizabilities. The scattering arises from the refractive index mismatch at the boundaries between two media or structures, i.e. between the ECM and cell, or between the plasma membrane and cytoplasm. On the cellular level, previous studies of mammalian cell suspension have shown that approximately 55% of light scattering from cell at angles greater than 40 degree was due to the internal cellular structures. In particular, the nucleus and its substructures are responsible for about 40 % of scattering at any angle (2000; Mourant et al, 1998). In embryonic tissues with multiple cell layers, light scattering from each cell layer is added and working distance of any light-based technique is thus limited. In addition, light scattering is also wavelength dependent and short

wavelengths (excitation light) are more prone to be scattered than longer wavelengths (fluorescence emission light). In this section, the working distance of FCS is investigated with both one photon excitation (OPE) and two photon excitation (TPE).

3.4.2 Penetration depth of confocal microscopy

We first examined the penetration depth of confocal microscopy in living zebrafish embryo. As FCS also utilizes the confocal scheme as discussed in section **2.1.3**, this gives a general idea how photon collection efficiency is affected by different penetration depth. It has been suggested that confocal microscopy can work at most 100 µm within biological tissues using OPE (Denk et al, 1990). Considering the transparent tissue of zebrafish embryo, this value could be larger but still varies depending on the instrumentation. Here we used an *Islet-1*-EGFP transgenic line to test our FCM setup. In this transgenic line, the neural-specific *Islet-1* promoter/enhancer drives EGFP expression in primary neurons, including a subset of sensory neurons and motor neurons (Higashijima et al, 2000). Fig. 3.3A shows a confocal image of a population of vagal motor neurons from a 3 dpf *Islet-1*-EGFP embryo (indicated by the yellow dashed ellipse). The fluorescence intensity of each motor neuron cell is measured by drawing a region of interest (ROI) along the cell body and calculating average intensity. The obtained fluorescence intensity of each cell is plotted against its tissue depth as shown in Fig. 3.3B. Theoretically, each

motor neuron cells should have equal amount of EGFP concentration and intensities. However, the figure showed that fluorescence intensities of motor neuron cells drops to only 15% as the image plane progresses from a surface 20 µm to 120 µm within the embryo body, although a constant laser power was applied for image acquisition. The result suggests that light collection efficiency is significantly influenced by deep tissue penetration.

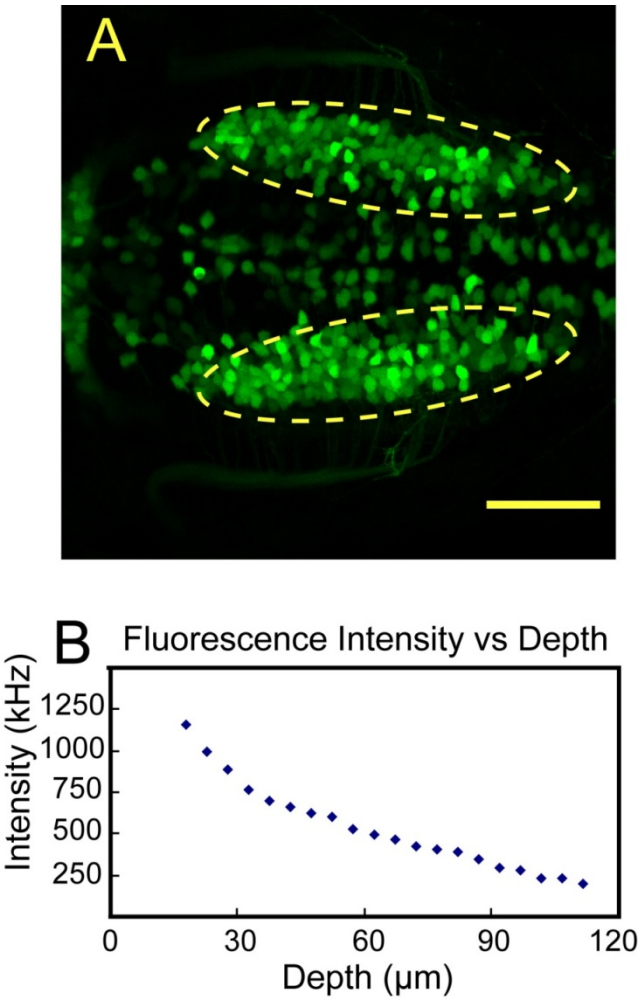

Fig.3.3: Fluorescence intensity changes against depth in confocal microscopy. (A) Dorsal view of vagal motor neurons of 3 dpf embryo of *islet-1*-GFP transgenic line as indicated in the dashed ellipse. Scale bar = 50 µm. (B) Fluorescence intensity measurements of EGFP-expressing motor neurons at different depth.

3.4.3 Penetration depth of FCS using OPE

To examine the working distance of FCS, we measured the diffusion time τ_d of cytosoplasmic EGPF in zebrafish motor neurons at different cell depths and compared the measurement accuracy. The cell depth was determined by a z-scan from the FCS measurement point towards the bottom skin of the embryo, indicated by a fluorescence intensity change when the focus shifts from the epidermis to agarose. Due to the high EGFP expression level, the motor neurons were pre-photobleached for 10 seconds with 1 mW 488 nm laser. To confirm that photobleaching does not change the diffusion time, we photobleached the same cell for 5, 10, and 15 seconds and obtained the same diffusion time (0.26 ± 0.03 ms). We measured 30 cells at different cell depths and the acquired τ_d values were then plotted against its depth as shown in Fig. 3.4A. Each point on the graph represents the mean of five individual measurements within the same cell. In general, if the cell is located within 50 µm inside the embryo, the τ_d values are constant within the margins of error and measurements have a small standard deviation (SD). When the cell is located between 50 to 80 µm, the τ_d has a slightly larger average value but a noticeably larger SD. If the cell is located beyond 80 µm, the autocorrelation is lost in almost all measurements and no parameters can be obtained (out of five cells with cell depth over 80 µm measured, only one could be analyzed). Based on these results we conclude that FCS can be applied for accurate measurements as deep as 50 µm inside the embryo using one-photon excitation (OPE). FCS can still provide meaningful data with penetration depth between 50 to 80 µm and sufficient number of measurements should be conducted in this case for statistical analysis. In

addition, the obtained *cps* values were also plotted against cell depth as shown in Fig. 3.4B. As discussed in section **3.3**, *cps* value determines the signal to noise ratio of FCS measurement (Koppel, 1974). Fig 3.4B shows that the average *cps* of measurement within 50 µm is 6 kHz, while beyond 50 µm it drops to only 2 kHz. This again suggests that accurate FCS measurements were limited within 50 µm. The limited working distance is restricted by strong and multiple light scattering and spherical aberrations induced by the heterogeneous refractive index of tissues (Hell et al, 1993), as cells comprise different sub-compartments and macro-molecules which make the cell optically non-homogeneous. Furthermore, light scattering particularly affects the signal to noise ratio in confocal illumination, which achieves optical sectioning with a detection pinhole that rejects out-of-focus light. In scattering tissues, the fluorescence light of interest will be scattered and thus will be partially blocked by the pinhole itself.

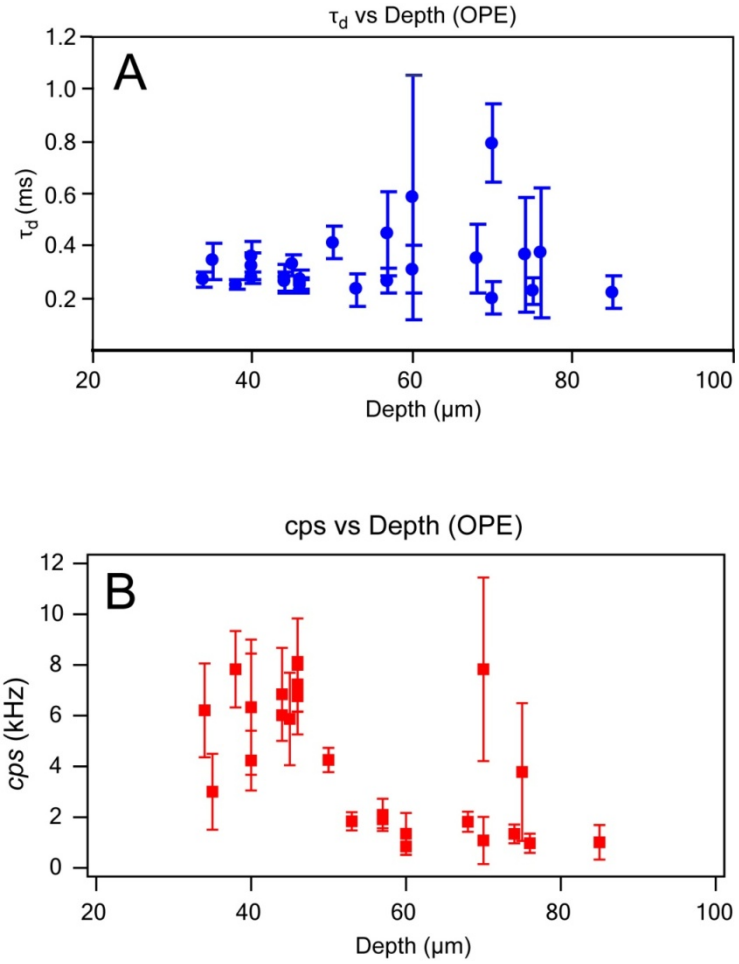

Fig.3.4: FCS penetration depth study using one photon excitation (OPE). FCS measurements were performed on motor neuron cells with different cell depth. A) The obtained diffusion time τ_d is plotted against cell depth. B) The obtained cps values were plotted against cell depth.

3.4.4 Penetration depth of FCS using TPE

Two photon excitation (TPE) describes a nonlinear process in which two photons are absorbed simultaneously (< 10^{-15} s) by a molecule. The molecule is promoted to an excited state and then follows the normal fluorescence emission pathway (Denk et al, 1990). TPE has two major advantages compared to conventional OPE. First,

because two or more photons combine their quantum energies for excitation, the photon generated after emission has higher energies than the excitation light, which is contrary to traditional fluorescence. Thus for commonly used fluorescence marker, TPE occurs in the NIR wavelength range from 700 to 1000 nm. NIR light not only propagates deeper into scattering biological tissue, but is also less phototoxic due to lack of endogenous absorbers at this wavelength range (Svoboda & Block, 1994). The second advantage of TPE is its intrinsically confined excitation volume. The probability of TPE is proportional to the square of the illumination intensity (the probability of OPE is directly proportional to the illumination intensity). When focused through a microscope objective, TPE only occurs at the perifocal region, eliminating the need for a pinhole. This means that all fluorescence photons are known to originate from the focus and thereby can be collected for analysis, which is especially useful when applied in scattering tissue. Consequently, in our setup a maximum pinhole size of 300 µm was used instead of normal 150 µm for better photon collection efficiency. Owing to these advantages, TPE has been rapidly adapted for FCS instrumentation and successfully applied for measurements made on tobacco leaf epidermal tissues with thick cell wall (Schwille et al, 1999a). We decided to evaluate whether TPE could be used for FCS measurements in zebrafish embryo at working distances deeper than 80 µm. We employed a Ti:sapphire laser with 100 fs pulse (Chameleon-XR, Coherent, Santa Clara, USA) in our FCS setup. The system was first calibrated and optimized using a standard fluorescence dye, tetramethylrhodamine (TMR) as shown in Fig. 3.5A. The direct output laser power cannot be tuned thus a continuously variable neutral density filter (NDC-25C-2, Thorlabs, Newton, USA) is employed in the light pathway to adjust the laser power.

The *cps* values of different measurements are plotted against their laser powers, and different colors in Fig. 3.5A represent measurements done with different wavelength. A maximum *cps* of 14 kHz was obtained for TMR calibration with 70 mW laser power at 840 nm, which is similar to other reports (Schwille et al, 1999a). Higher *cps* value can be further achieved by adjusting the temporal and spectral laser pulse width (Mutze et al, 2007), but not carried out in this work due to limited instrumentation. As EGFP is the fluorophore expressed in the zebrafish embryo, the calibration of *cps* value versus wavelength using EGFP buffer solution was then performed (Fig. 3.5B), aiming to find the proper wavelength for EGFP excitation. Excitation wavelengths were tuned from 850 to 950 nm in step of 10 nm. At each wavelength, the laser power was adjusted (50 to 70 mW depending on the wavelength) to achieve maximum *cps*, and the *cps* values are then plotted against their wavelengths. The result shows that highest *cps* value of ~ 2 kHz can be achieved from 880 to 920 nm. In the following experiments, 890 nm was used for EGFP excitation in zebrafish embryos.

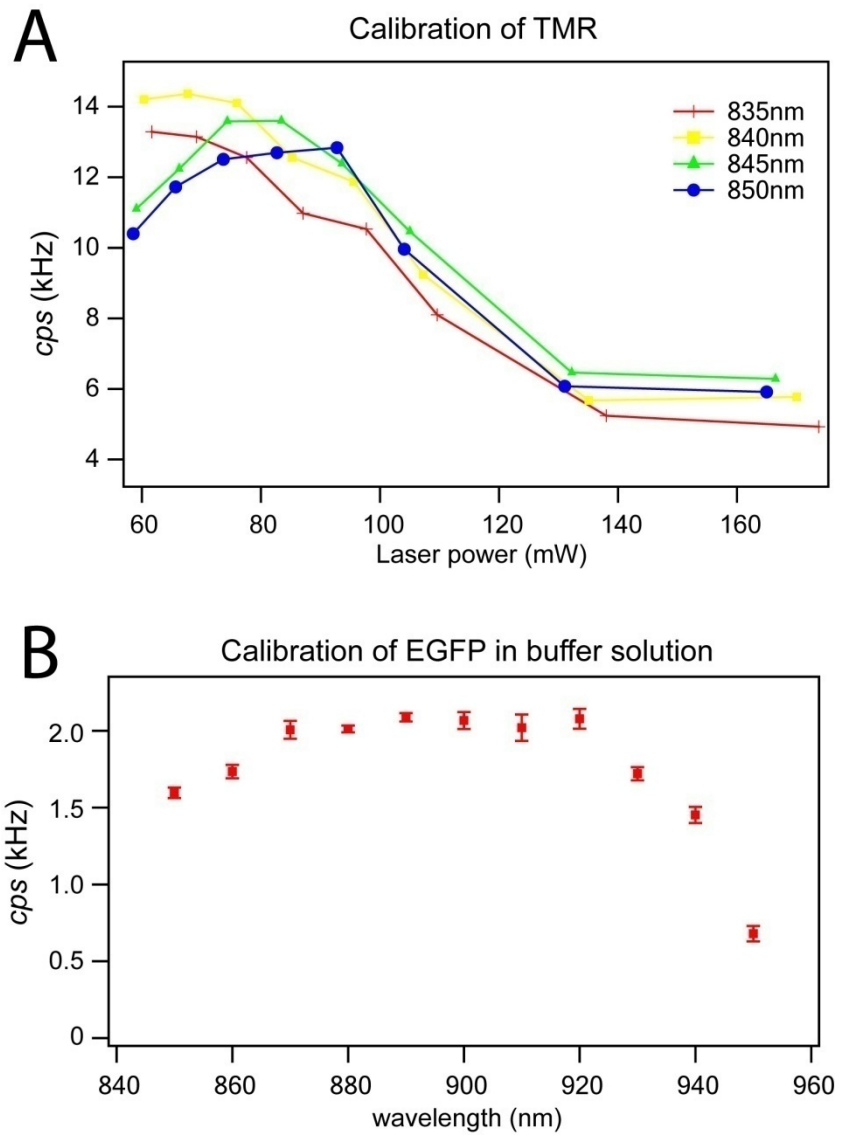

Fig.3.5: Calibration of FCS using two photon excitation (TPE). A) Calibration of TMR using TPE. Obtained *cps* values were plotted against different laser power. Each colored curve represents measurement with a different wavelength. B) Calibration of EGFP in buffer solution using TPE. Obtained *cps* values were plotted against different wavelengths. Each point represents the average value of 4 repeated measurements. At each wavelength, laser power was pre-calibrated to achieve highest *cps*.

After EGFP buffer solution calibration, we repeated the measurement of cytoplasmic EGFP diffusion time versus cell depth in the zebrafish embryo using TPE at 890 nm. However, in the zebrafish embryo measurements we saw strong

photobleaching of EGFP even with halved TPE laser power of 30 mW. This is different from our EGFP buffer solution calibration, and the average *cps* obtained in zebrafish embryo is only 0.5 kHz, compared to 2.1 kHz of EGFP buffer solution. Due to the strong photobleaching, over 80% of our 48 TPE measurements yield no result. The diffusion times obtained from a small portion of the measurements were plotted against their cell depth as shown in Fig. 3.6A. However, TPE did not improve the penetration depth in the case of EGFP. The determination of diffusion times worsened beyond 80 µm. It seems that TPE-FCS did not improve the working distance in living embryos in this case partially owing to two reasons. The first reason is the use of a de-scanned detection scheme. Under de-scanned detection, emission light will be reflected back from the scanning mirrors and pass several lenses and the pinhole before detection. As discussed above, TPE has intrinsically confined excitation volume and no pinhole is required. Thus a non-de-scanned detection scheme (which means photons are directly collected after microscope objective) is usually advised for TPE. In this case, the photon collection efficiency using de-scanned detection scheme is low compared to non-de-scanned detection schemes so the potential of TPE was not fully explored (Le Grand et al, 2008). The second and more important reason is the inefficiency of EGFP as a TPE dye in the zebrafish embryo. The low fluorescence yield of EGFP using TPE dramatically decreased the signal to noise ratio of FCS measurements. The average *cps* of EGFP obtained using TPE is only 0.5 kHz compared to 6.0 kHz using OPE. The low molecular brightness of EGFP using TPE has so far been attributed to photobleaching (Dittrich & Schwille, 2001; Petrasek & Schwille, 2008a) and saturation (Berland & Shen, 2003). In an attempt to improve in this regards, we

injected TMR, a good TPE dye, into the embryo's blood circulation. TPE-FCS measurements were conducted on small vessels ~ 200 µm deep within the head and the signal still generated robust autocorrelation (Fig. 3.6B). The penetration depth in this case was limited by the working distance of the objective (the working distance of the Olympus UPLAPO 60×W objective is 280 µm), rather than limited by the tissue light scattering. Using microscope objective with high NA and longer working distance, i.e. recently launched Olympus XLPlan 25×W with 1.05 NA and 2 mm working distance, TPE-FCS could potentially work even deeper in tissue with TMR. This confirms that TPE provides better penetration depths when using appropriate dyes. It should be noted that the penetration depth is dependent on the opacity of the embryo tissue which itself is variable at different embryonic stages. Using more optically transparent strains of fish such as *albino*, *nacre* or *casper* mutants (Henion et al, 1996; Lister et al, 1999) could also improve penetration depth due to reduced pigmentation.

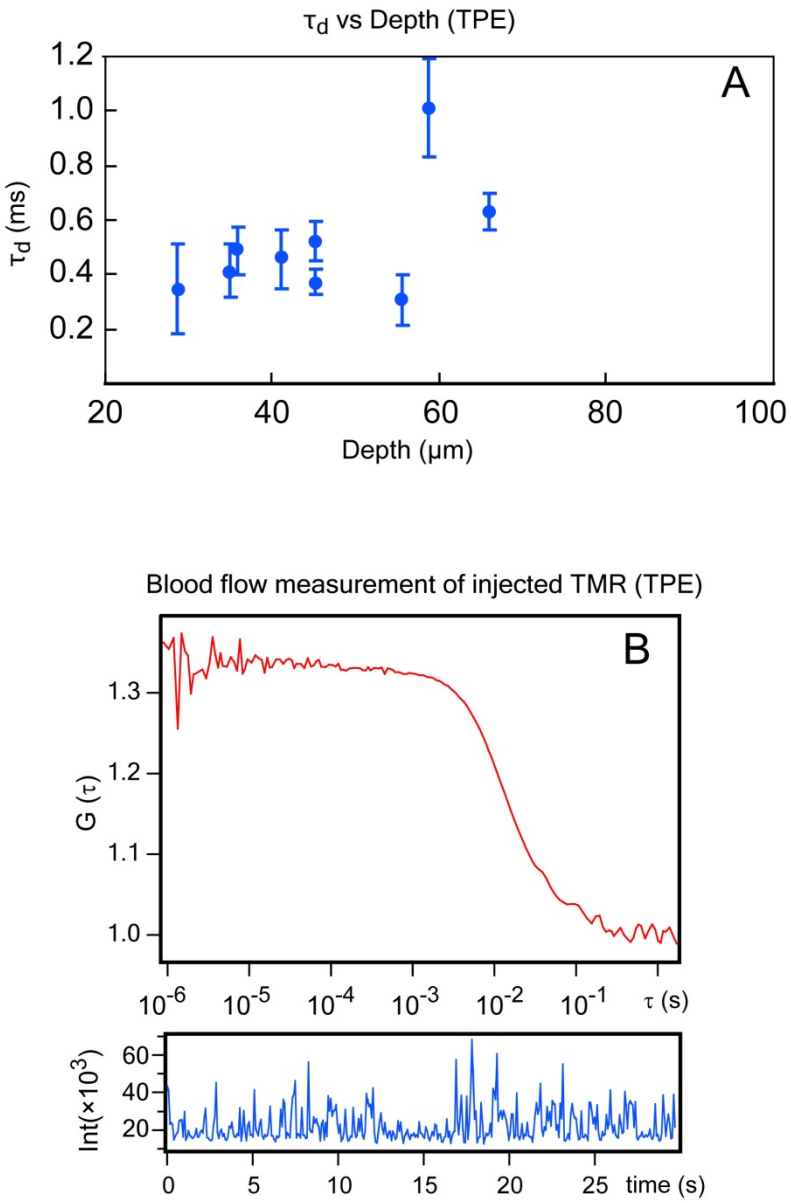

Fig.3.6: FCS penetration depth study using two photon excitation (TPE). A) TPE-FCS measurements were performed on motor neuron cells with different cell depth. The obtained diffusion time τ_d is plotted against cell depth. B) TPE-FCS flow measurements of injected TMR in the blood vessel at 840 nm. This measurement was conducted at cell depth ~ 200 μm. At the bottom is the intensity trance of the measurement.

Chapter 4

Probing Single Molecule Events in Living Zebrafish Embryos with FCS

4.1 Introduction

The recent development of FCS/FCCS has opened new horizons for the study of individual macromolecules under physiological conditions (For reviews see: Dittrich et al, 2001; Haustein & Schwille, 2007; Hwang & Wohland, 2007; Liu et al, 2008b; Medina & Schwille, 2002; Thompson et al, 2002). Internal dynamics, conformational changes and subpopulation characteristics, parameters that have been previously masked in ensemble averages and standard deviations, are now directly accessible in living cells. FCS provides a promising alternative to photobleaching recovery methods for determining biomolecule dynamics at very low concentrations. Photobleaching recovery, which tolerates limited instrumentation and requires higher dye concentration, was established as the first technique to be able to determine diffusion coefficients of fluorescently labelled biomolecules in living cells (Axelrod et al, 1976). It has been proven to be useful in determining biomolecule dynamics in the plasma membrane, cytoplasm, cell nucleus and even mitochondria

(Feder et al, 1996; Lukacs et al, 2000; Partikian et al, 1998; Swaminathan et al, 1997). However, the inherent theory and experimental realization of FRAP restrict its temporal resolution to the millisecond range while some cells show much faster protein activity (Phair & Misteli, 2000). In addition, the invasive dye photobleaching procedure requires a high fluorescent dye concentration and a relative large area to perform, which greatly reduces its sensitivity. FCS, in comparison, utilizes non-invasive fluorescence fluctuation analysis of small ensembles in a diffraction-limited observation volume, and provides a far higher dynamic performance in the submillisecond range to probe protein mobility at their physiological expression levels. Recent publications have demonstrated the precise determination of cytoplasmic, nucleoplasmic and membrane-bound diffusion of different biomolecules at nanomolar concentrations, with a temporal resolution from tens of nanoseconds up to seconds (Dross et al, 2009; Eggeling et al, 2009; Ries & Schwille, 2008; Weiss, 2007). The <1 fL size of the observation volume (approximate 0.5 µm in diameter) also allows the single molecule measurement to be carried out in various subcellular compartments. In addition, applying the concept of anomalous subdiffusion, the steric hindrance of diffusing molecules and the crowdedness of the cytoplasm at the molecular scale can also be investigated (Banks & Fradin, 2005; Schwille et al, 1999b; Weiss et al, 2004). In this chapter, we measured the blood flow velocities with high spatial resolution and determined the diffusion coefficients of cytosolic and membrane-bound EGFP or EGFP labeled proteins in different cell types.

4.2 Blood Flow Measurements in Living Zebrafish Embryo

4.2.1 Introduction

Zebrafish is a widely accepted animal model for studying of development and function of the vascular system (Zhong, 2005), owing to its small size, transparent tissue and genetic similarity to mammals. In particular, quantitative measurements of blood flow play an important role in understanding vascular development, as mechanical signals such as shear stress induced by blood flow is essential for normal development of organs involved in circulation (Hove et al, 2003; Korzh et al, 2008). Currently, several approaches have been implemented to measure flow velocity in microscale systems and small animal blood vessels, i.e. particle imaging velocity (PIV, Santiago et al, 1998), laser speckle imaging (Cheng et al, 2003), NMR imaging (Manz et al, 1995), and laser line scanning velocimetry (Malone et al, 2007). However, those imaging based methods usually require high concentration of large probes which could obstruct flow in microchannels and small vessels. They also provide data characterized by good temporal but low spatial resolution, and a high level of spatial resolution is a key factor to understand the local changes of blood flow in the vessel. Therefore, a method that can probe flow velocity non-invasively, and possesses submicrometer range of spatial resolution is desirable. FCS has been proven to be an attractive alternative to measure flow. Several publications have

demonstrated that FCS can measure transport of large protein units in plant cells (Kohler et al, 2000), EYFP labelled bacteria flowing in a capillary (Kunst et al, 2002), and DNA molecules in a microfluidic channel (Foquet et al, 2002). Firstly, FCS works at extremely low concentrations of small dye molecules in the range of 1 nM, eliminating the problem of vessel obstruction by probes. In living zebrafish embryo, we also found that the autofluorescence present in the serum generates sufficient *cps* for FCS analysis. No additional dye injection into the circulation is required, which makes FCS a truly noninvasive approach. Since this can be accomplished independently of erythrocytes simply based on autofluorescence of serum, FCS can also be used to measure blood flow in small vessels during embryogenesis even in absence of blood cells. Secondly, the spatial resolution of FCS relies on the size of the observation volume, which is about 0.5 µm in diameter, while the width of the zebrafish vessel is usually 15 to 20 µm for the dorsal aorta and cardinal vein and ~ 5 µm for small vessels in the head. FCS thereby allows determination of the spatial flow profile across the vessel and shear stress along the vessel wall could be studied in detail (manuscript in preparation). In this section, we discussed the theory of flow measurements by FCS and demonstrated the accurate determination of blood flow velocities in different zebrafish vessels.

4.2.2 FCS Theory of Flow Measurement

When there is active transport, such as laminar flow, present in the dynamic system, or the observation volume is scanned across the sample in a linearly controlled way, the motion of the fluorophore in and out of the observation volume is now not only controlled by Brownian motion but also by the flow or scan velocity V_f . Making the assumption that the flow or scan is uniform and single-directional in a plane perpendicular to the optical axis, the ACF in the case of single flow component coupled with free diffusion is written as:

$$G(\tau) = \frac{1}{N} \cdot g_{3D} \cdot \exp\left[-\left(\frac{\tau}{\tau_f} \right)^2 \cdot \left(1 + \frac{\tau}{\tau_d} \right)^{-1} \right] + G_\infty \tag{4.1}$$

with:

$$g_{3D} = \left(1 + \frac{\tau}{\tau_d} \right)^{-1} \left(1 + \frac{\tau}{K^2 \tau_d} \right)^{-1/2} \tag{4.2}$$

where $\tau_f = \frac{\omega_0}{V_f}$ is the time required for a molecule to flow through the focal volume (Koppel et al, 1994; Magde et al, 1978).

In the case of blood flow measurement, however, a one-flow model is not adequate for data analysis, as there are alternating slow and fast blood flows in the cardiac cycle stemming from systolic and diastolic periods as shown in Fig. 4.1B. Thus a two-flow model, representing the average systolic and diastolic flow velocities, was used and the normalized ACF is written as:

$$G(\tau) = \frac{1}{\mathrm{N}} \cdot g_{3\mathrm{D}}(\tau) \cdot \left\{ \begin{array}{l} F_{f1} \cdot \exp\left[-\left(\frac{\tau}{\tau_{\mathrm{f1}}} \right)^2 \cdot \left(1 + \frac{\tau}{\tau_{\mathrm{d}}} \right)^{-1} \right] + \\ \left(1 - F_{f1} \right) \cdot \exp\left[-\left(\frac{\tau}{\tau_{\mathrm{f2}}} \right)^2 \cdot \left(1 + \frac{\tau}{\tau_{\mathrm{d}}} \right)^{-1} \right] \end{array} \right\} + G_\infty \tag{4.3}$$

where F_{f1} is the fraction of the first flow component, i.e. the fraction of the time the system exhibits flow rate 1 compared to the time the system spends in flow rate 2. τ_{f1} and τ_{f2} are the first and second characteristic flow times for a molecule through the focal volume (Pan et al, 2009; Pan et al, 2007b).

4.2.3 Flow Velocity Measurement by FCS

The autofluorescence present in the serum generates sufficient *cps* for FCS analysis thus no additional dye injection into the circulation is required. Therefore, a 3 dpf zebraifish embryo was directly mounted in a lateral view, and FCS measurements were performed using 100 µW of the 543 nm laser line in the dorsal aorta and cardinal vein in the trunk region as shown in Fig. 4.1A. Prior to the measurement, the embryo was anesthetized by 500 µM of tricaine to prevent body movement (Westerfield, 2000). However, tricaine at high doses is known to suppress cardiac function and the effect can vary from embryo to embryo. Thus velocity comparison was only conducted within one fish. As the flow velocities are not equal across the vessel and the spatial velocity profile abides by the theoretical model of the parabolic profile of a cylindrical tube (Chien et al, 1977), the observation volume was positioned at the center of the vessel to account for the maximum velocity. A typical FCS measurement in the cardinal vein was shown in Fig. 4.1C. The experiment curves were fitted with a 3D two flow model (Eq. 4.3) as discussed in section **4.1.2**. The fast and slow portions represent the average systolic and diastolic

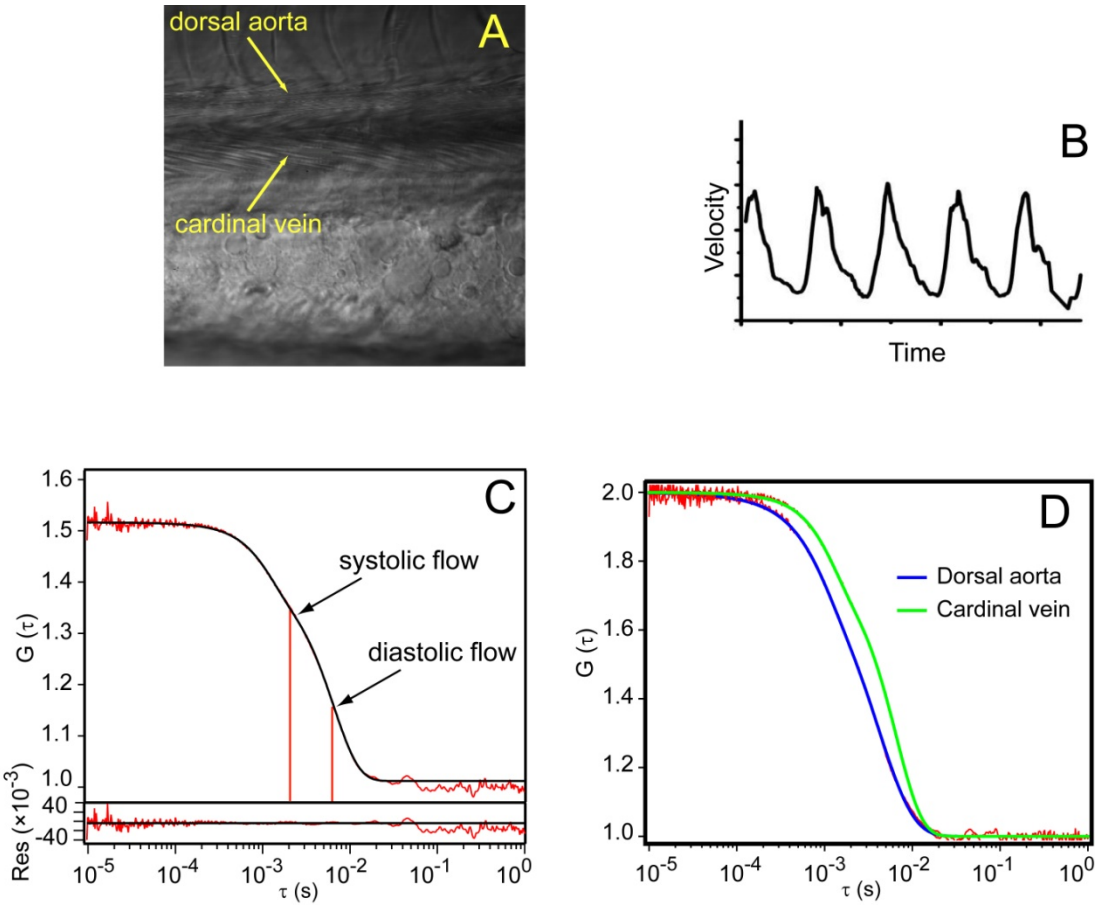

Fig. 4.1: FCS blood flow measurement in living zebrafish embryos. A) A transmission channel confocal image showing the dorsal aorta and cardinal vein of a 3 dpf AB zebrafish embryo. B) A figure showing the real time blood flow velocity. There are alternating fast and slow blood flows in the cardiac cycle stemming from systolic and diastolic periods. C) A typical FCS measurement of blood flow, showing both experimental curve (red) and fitting curve (black). The experimental curve was fitted with a 3D 2 flow model (Eq. 4.3). At the bottom is the fitting residual. D) Normalized FCS blood flow measurements obtained from dorsal aorta and cardinal vein, showing together experimental curves (red) and fitting curves (blue for dorsal aorta and green for cardinal vein).

flow velocities, respectively. FCS measurements were performed in dorsal aorta and cardinal vein and the data were tabulated in Table 4.1. The parameter we get from data fitting is the flow time τ_f. In order to calculate the absolute flow velocity V_f,

one still needs to calibrate the observation volume using 543 nm laser excitation and obtain the radial axis ω_0. The system was calibrated with TMR with a known diffusion coefficient of 3.1×10^{-6} cm^2s^{-1} (Schwille et al, 1999a) and the obtained ω_0 is ~ 0.4 μm. The flow velocity V_f values were calculated accordingly, and the results suggested that the velocities of both systolic and diastolic flow in the dorsal aorta were faster than those in the cardinal vein. This is expected due to the different levels of cardiac-mediated blood pressure in these vessels and their widths (as we have measured, the dorsal aorta is around 15 μm in width and the cardinal vein is around 19 μm). It should be noted that FCS blood flow measurements should be avoided in regions close to the heart as the body movement induced by the heartbeat introduces an additional periodic time trace into the ACF curve, making analysis difficult (Fig. 4.2).

Table 4.1: Blood flow velocities of dorsal aorta and cardinal vein.

Vessel	τ_f (ms)		V_f (μm/s)	
	systolic	diastolic	Systolic	Diastolic
Dorsal aorta	1.3 ± 0.2	6.3 ± 0.5	312 ± 23	64 ± 4
Cardinal vein	1.7 ± 0.2	9.8 ± 1.1	240 ± 18	41 ± 4

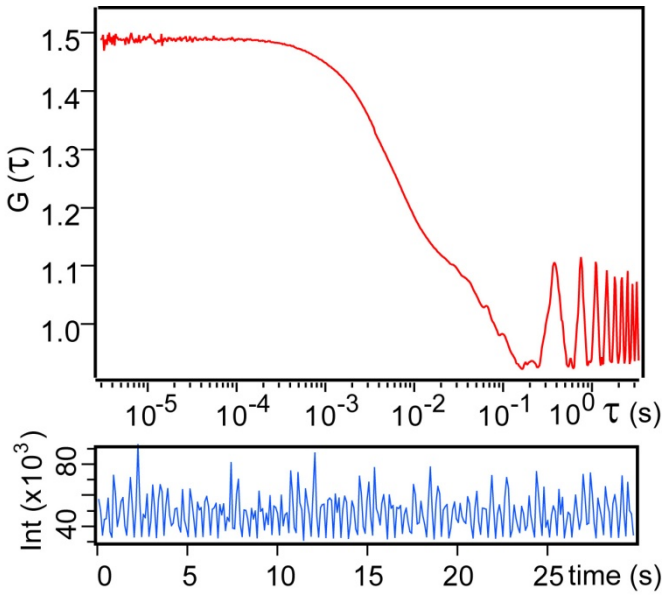

Fig. 4.2: A typical FCS measurement of blood flow in the heart of zebrafish embryo. The body movements induced by the heartbeat introduced a periodic time trace into the ACF curves as seen at the end of the ACF curve.

4.3 Protein Translational Diffusion Measurements in Living Zebrafish Embryo

4.3.1 Introduction

Energy-independent random diffusive motion in the 3D cytoplasm is the most common mechanism for the translocation of intracellular proteins and plays a fundamental role in determining the activity and function of biomolecules, i.e. the formation of cellular patterns and diffusion-limited reactions (Murray, 1993; Politz et al, 2003). For membrane-bound proteins, diffusive motion enables segregation of the plasma membrane into rigid subdomains, also known as rafts, and directs the intermediate transport between endoplasmic reticulum (ER) and Golgi apparatus (Antonny & Schekman, 2001; Storrie & Nilsson, 2002). Accurate determination of the diffusive behaviour of the protein thus provides evidence and insight for better understanding of protein functions. As we discussed, FCS is particularly suitable for characterizing mobility from milliseconds to seconds, which covers the dynamic range of most biomolecules in living cells. In this section, we measured the diffusion coefficients of cytoplasmic EGFP in different subcellular compartments, as well as in different cell types. Next, we expressed the EGFP labelled membrane protein Cxcr4b and measured its diffusion behaviour on a 2D membrane. At last, all FCS data were fitted with the anomalous subdiffusion model (Schwille et al, 1999b; Weiss et al, 2004) and the anomality factor was determined and compared.

4.3.2 Protein Translational Diffusion Measurements in Cytoplasm and Nucleoplasm

The physical structures of cell cytoplasm and nucleoplasm have been an interesting topic for decades (for review see Lamond & Earnshaw, 1998; Luby-Phelps, 1994) and it is clear that cytoplasm and nucleoplasm have distinct substructures. The cytoplasm comprises dissolved solutes and macromolecules in a complex array of microtubules, actin, and intermediate filaments; and it contains various membrane-bound subcompartments. The nucleoplasm, in comparison, is mainly filled with chromatin whose structure is dynamically changing; and it contains no membrane-bound subcompartments. Numerous publications have studied the translational diffusion of fluorescent probes or functional proteins in cytoplasm and nucleoplasm, aiming to investigate the nanoscale viscoelasiticity of intracellular fluids (Guigas et al, 2007b), size-dependent DNA or protein mobilities (Dauty & Verkman, 2005; Seksek et al, 1997), protein distributions and function (Phair & Misteli, 2000), and chromatin density (Dross et al, 2009). In particular, two recent publications by Pack et. al. and Liang et. al. suggest that EGFP diffuses faster in cytoplasm than in nucleoplasm (Liang et al, 2009; Pack et al, 2006). However, in another article by Guigas et. al., it has been shown that the cytoplasm is slightly more crowded than the nucleus, which could lead to slow diffusion in cytoplasm (Guigas et al, 2007a). Those experiments were all performed in commonly used cell lines, e.g. Hela, CHO, and mouse fibroblasts cells but the results were contradicting. In this section, we

carried out the cytoplasm versus nucleoplasm measurements of EGFP diffusion in motor neuron cells in living zebrafish embryos.

We used the *Islet-1*-EGFP transgenic line for this purpose. A 3 dpf embryo was mounted in lateral view and a single motor neuron cell was focused under confocal mode using our custom-built FCM. As the EGFP molecules are evenly distributed in the cytoplasm and nucleoplasm, a point photobleaching was performed to outline the boundary of the cell nucleus. Guided by confocal image, a single point was selected at the center of the motor neuron cell (usually within the nucleus) to perform point scan with 100% laser power. A confocal image was immediately captured after the point scan as shown in Fig. 4.3A and 4.3B. As the EGFP molecules cannot diffuse through the nuclear pores fast enough, the fluorescence intensities in nucleus are then lower than that in the cytoplasm. Three points were then selected in both cytoplasm and nucleoplasm for FCS measurements as marked in Fig. 4.3A and 4.3B, and four measurements were performed in each point. The experimental data were fitted with 3 dimensional 1 particle 1 triplet model (Eq. 2.26) and the obtained diffusion times in the cytoplasm were compared with that in nucleoplasm as shown in Fig. 4.3C and 4.3D. Interestingly, the results showed that EGFP diffused slightly slower in cytoplasm than in nucleoplasm, contrary to Pack et. al. and Liang et. al.'s findings (Liang et al, 2009; Pack et al, 2006). FCS measurements were repeated in several more motor neuron cells in different zebrafish embryos and the average diffusion time obtained in cytoplasm and nucleoplasm is 0.29 ± 0.04 ms and 0.23 ± 0.03 ms, respectively. Our results support Guigas et.al.'s finding that the cytoplasm is more crowded than the nucleus (Guigas et al, 2007a).

Nevertheless, the difference was relatively small and the average values were within each other's standard deviations. It should be noted that cell nucleus can undergo dramatic structural rearrangement during cell division cycle, i.e. at synthesis stage (S phase) DNA replication could increase the chromatin amount and consequently the nucleus may become more crowded. In both Pack et. al. and Liang et. al.'s paper, cell cultures were used but the cell phase was not mentioned. Thus, the slow diffusion of EGFP molecules in the nucleus in their results could be due to measurements in cells at unfavorable phases. In comparison, our FCS measurements were performed in motor neuron cells, which after maturation usually stay indefinitely at G_0 phase and arrest division (Alberts et al, 2002).

The results also suggested that the EGFP molecules diffuse relatively fast in both cytoplasm and nucleoplasm, considering the macromolecular crowding environment within cells. Measurements of EGFP in buffer solution at the same experimental condition yielded a diffusion time of 0.19 ± 0.02 ms, which is only about 40% faster than in the cytoplasm. This could be owing to the small size of EGFP (27 kDa), as organelles, cytoskeleton, and even dissolved macromolecules are less obstructive for small sized probes and the EGFP molecule can still diffuse fast within aqueous voids. In contrast, study of latex beads with diameter of 100 nm showed greatly obstructive diffusion in the cytoplasm (Tseng et al, 2002).

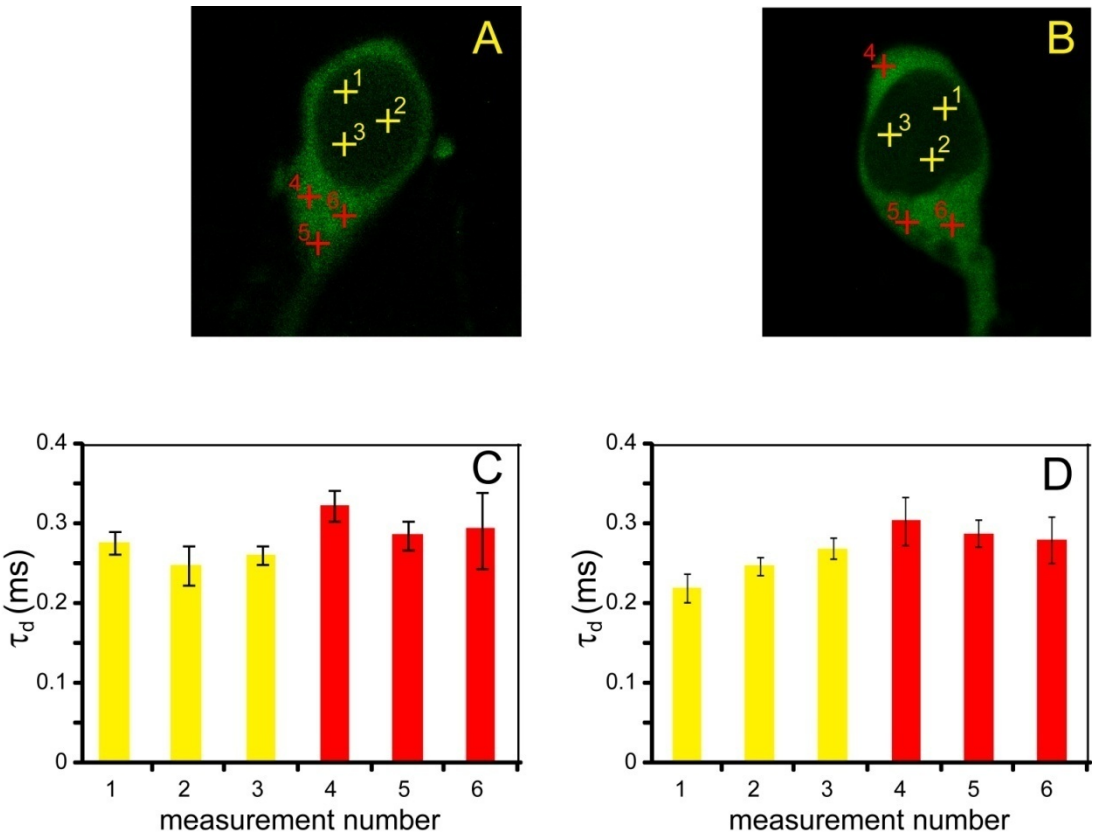

Fig. 4.3: Diffusion time measurements within one cell. FCS measurements were performed in the nucleoplasm and cytoplasm within one cell. The nucleus was outlined by point photobleaching in nucleus. A) and B) are the confocal images captured right after the point photobleaching. As EGFP molecule cannot diffuse through the nuclear pore fast enough, the fluorescence intensitiy in the nucleus is lower than that in the cytoplasm. Three points were selected in both nucleus and cytoplasm for FCS measurements as indicated in the images by yellow and red crosses, and the obtained diffusion time were ploted as shown in C) and D), respectively.

4.3.3 Protein Translational Diffusion Measurements in Motor Neuron Cells and Muscle Fiber Cells

We next examined EGFP diffusion in different cell types. In zebrafish embryos, we injected EGFP plasmid into a single blastomere at the 16-cell stage as described before, and observed fluorescence expression in both muscle fiber cells (Fig. 4.4A, at posterior trunk region) and motor neurons (Fig. 4.4B, at hindbrain/spinal cord junction region). The mosaic distribution of descendants of the injected blastomere provides a range of cell types with different EGFP expression levels to choose from. FCS measurements were performed in both muscle fiber cells and motor neurons cells that were within 50 μm from the body surface. The ACF curves suggested slightly different diffusion behavior (Fig. 4.4C). The average diffusion time τ_d obtained was 0.29 ± 0.06 ms in motor neuron cells and 0.36 ± 0.04 ms in muscle fiber cells. The diffusion time obtained in motor neuron cells in EGFP plasmid injected embryos was exactly the same as that in the motor neuron cells in *Islet-1*-EGFP transgenic line (section **4.2.2**). We next calculated the corresponding diffusion coefficients using methods described in section **2.1.2**. Measurement of the reference dye fluorescein in aqueous solution yielded a τ_d of 43.7 μs. Using 300 $\mu m^2 s^{-1}$ as the diffusion coefficient of fluorescein (Wohland et al, 1999), the corresponding EGFP diffusion coefficients were calculated to be 45.3 ± 9.4 $\mu m^2 s^{-1}$ in motor neurons and 36.5 ± 4.1 $\mu m^2 s^{-1}$ in muscle fibers. Note that the diffusion coefficients for EGFP inside cells represent lower limits since the focal volume is slightly increased due to the refractive index mismatch between water and tissue. However, the values are very close to typical values found in 2D cell cultures. According to the Stokes-Einstein relation ($D=\frac{kT}{6\pi\eta r}$, where k is the Boltzmann constant, T is the absolute temperature, and r is the hydrodynamic radius of the

diffusing molecule), the diffusion coefficient of a molecule is inversely proportional to the viscosity of the medium. Using 2.1 nm as the hydrodynamic radius of EGFP as reported by others (Liang et al, 2009), the relation can be written as $D = 152 \cdot \eta^{-1}$ for 25°C room temperature, and the medium viscosity can be calculated accordingly. In this way, the viscosity of the cytoplasm of a cell can be estimated and compared to others, and our result suggests a higher viscosity of the cytoplasm of muscle fiber cells compared to that of motor neuron cells. It has been shown that cancerous cells have increased cellular elasticity and are considerably "softer" than normal cells (Beil et al, 2003; Darling et al, 2007), which possibly enhances their potential to penetrate tissue and enter lymphatic or blood circulations. Therefore the value of cytoplasm viscosity could be possibly used as a parameter for characterization of cell types and states in mixed cell populations.

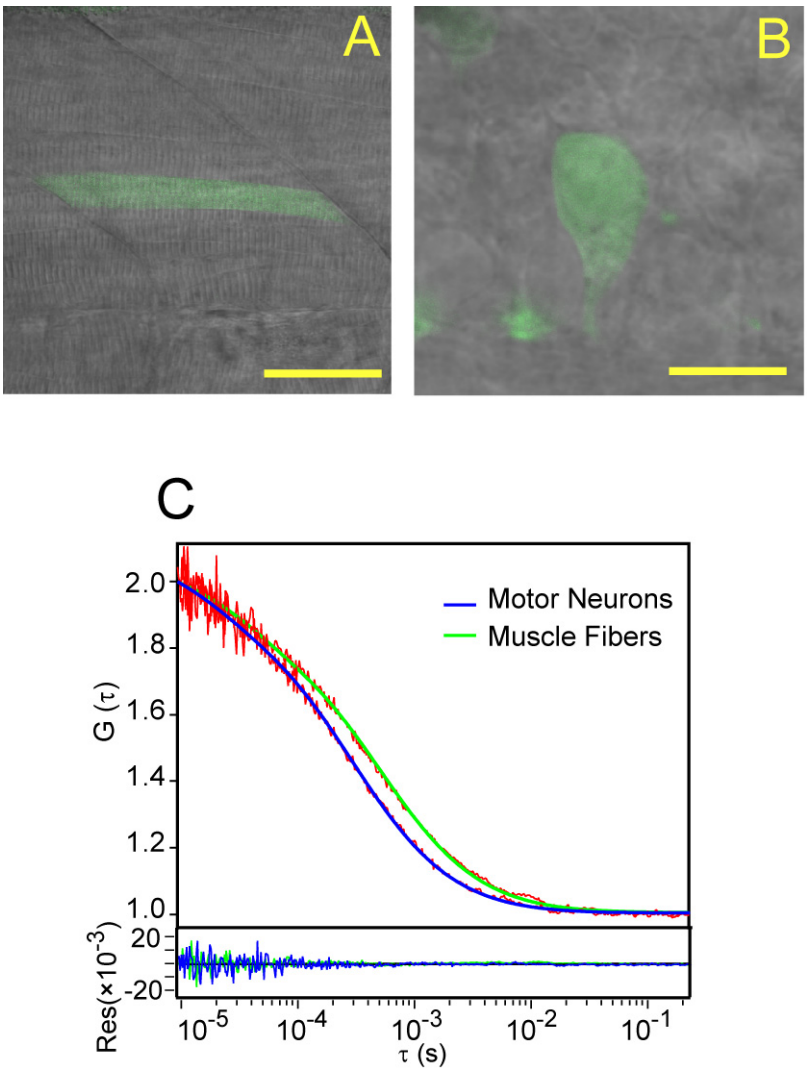

Fig. 4.4: Diffusion time measurements in different cell types. EGFP plasmid was injected at 16-cell stage and fluorescence expression was observed in both A) muscle fiber cells (at posterior trunk region) and B) motor neuron cells (at hindbrain/spinal cord junction region) at late stages. Picutres are shown together with transmission channels and fluorescent channels. Scale bar = 40 µm in A) and 10 µm in B). C) Normalized ACF curves of cytoplasmic EGFP in motor neuron cells and muscle fiber cells, showing together with experimental curves (red) and fitting curves (green and blue). The two ACF cruves shown here are extreme cases to illustrate the difference. At the bottom are the fitting residuals.

4.3.4 Protein Translational Diffusion Measurements of Cxcr4b-EGFP on Membrane

The mobility of membrane proteins is critical in determining their interaction capabilities and protein functions. Quantifying the diffusion coefficient of membrane proteins therefore provides insights in understanding protein behaviour and organization of cell membranes. In this section, we measured the diffusion coefficients of EGFP labelled Cxcr4b on the membrane of muscle fiber cells. The EGFP gene was attached to the Cxcr4b gene (see section **2.4** for detail) and the constructed Cxcr4b-EGFP plasmid was microinjected into a single blastomere at 16-cell stage. The EGFP was attached to the C terminus of Cxcr4b (Fig. 4.6B insert) so that it won't obstruct binding of ligand to Cxcr4b at the N terminus (Babcock et al, 2003). As shown by confocal microscopy the EGFP signal in muscle fibers was found along the membrane (Fig. 4.6A). Lower concentrations of Cxcr4b-EGFP plasmid (40 ng/μL) were injected as it has been shown that overexpression of Cxcr4b leads to developmental abnormalities (Doitsidou et al, 2002). The EGFP-tagged Cxcr4b was found to be uniformly distributed along the muscle fiber plasma membrane. In FCS measurements, the orientation and topography of the cell membrane can greatly influence FCS measurements, thus correct positioning of the observation volume on the membrane is critical for accurate data acquisition (Milon et al, 2003). The most commonly used method is to position the volume on the top or bottom membranes (parallel to the x-y plane) and adjust the height of the volume to achieve highest fluorescence intensity. In this experiment, the FCS observation volume was placed on the bottom membrane of the muscle fiber cell (more close to the embryo

surface) and the z-position was adjusted in steps of 0.1 µm until the maximum fluorescence intensity was observed. A more accurate method is to perform FCS measurements at different height in the proximity of the top or bottom membrane and select measurements with fastest diffusion time and highest *cps* (Milon et al, 2003). However, this method is time-consuming and the long time laser excitation causes irreversible EGFP photobleaching. Thus this method is not adopted here. A typical ACF curve is shown in Fig. 5.6B. The fluorescence intensity trace showed no intensity bursts, suggesting no higher order aggregation of Cxcr4b on the membrane. The fitting yielded a diffusion time of 22.1 ± 7.1 ms for the Cxcr4b-EGFP on the membrane. The corresponding diffusion coefficient was 0.60 ± 0.19 $\mu m^2 s^{-1}$, in agreement with previously published results obtained in cell cultures (Barak et al, 1997). It should be noted that Cxcr4b was shown to form homodimers (Babcock et al, 2003; Percherancier et al, 2005) and heterodimers with Cxcr7 (Levoye et al, 2009) in response to ligand binding. Thus the diffusion coefficient obtained here depicts the diffusion behavior of the homo- and heterodimer complex.

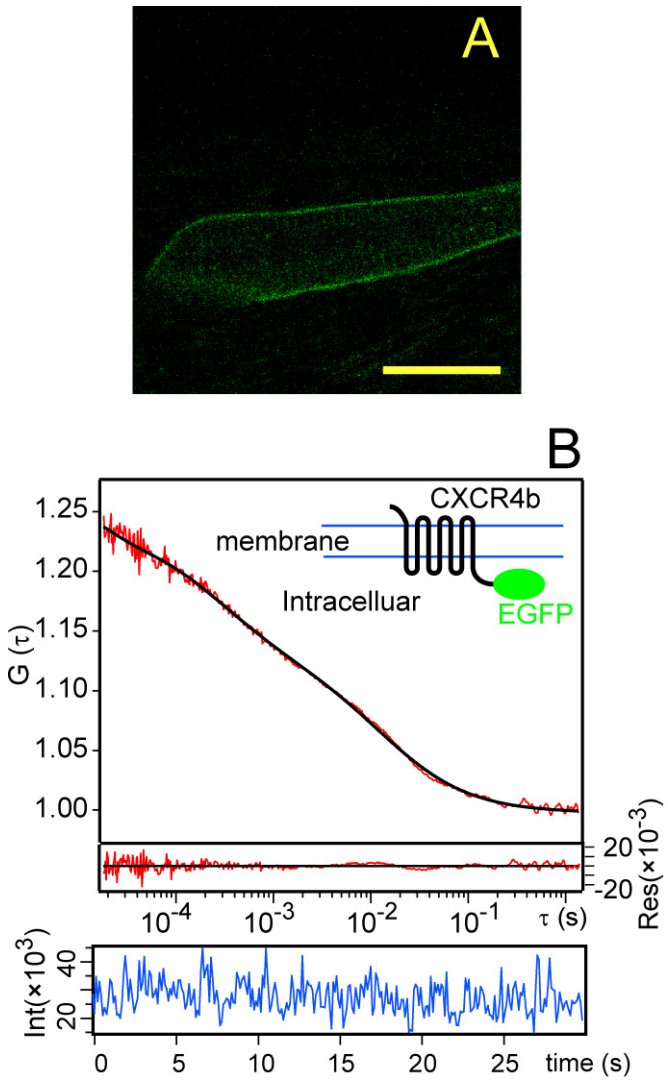

Fig. 4.5: Diffusion time measurements of Cxcr4b-EGFP. A) Confocal image of Cxcr4b-EGFP-expressing muscle fiber, membrane expression pattern was observed. Scale bar = 20 µm. B) FCS measurement of Cxcr4b-EGFP on membrane of muscle fibers, showing experimental curve (red) and fitting curve (black). Insert is the schematic drawing of the construct. Bellows are fitting residuals and fluorescence intensity trace.

4.3.5 Data Analysis Using Anomalous Subdiffusion Model

Anomalous subdiffusion describes an obstructed diffusion where the time dependence of the mean square displacements (MSD) is not linear (Feder et al, 1996; Schwille et al, 1999b), i.e., $\left\langle r^2(t)\right\rangle \sim t^{\alpha}$ with $0<\alpha\leq 1$ (α is the anomality factor; the smaller α, the more anomalous the diffusion. $\alpha=1$ is thereby for normal diffusion). Anomalous subdiffusion is usually found in crowded environments in which the molecular crowding affects the diffusive properties of the probe and reduces its diffusion coefficient. It has been shown that cytoplasm and nucleoplasm both induce anomalous subdiffusion for nanoscale tracer particles (Banks & Fradin, 2005; Wachsmuth et al, 2000; Weiss et al, 2004), and the anomalous subdiffusion affects protein folding and assembly (Weiss, 2003), kinetic rates (Saxton, 2002), and the time course of enzymatic reactions (Berry, 2002). As reported by Schwille et. al., FCS can be use to evaluate the degree of anomality of the diffusion (Schwille et al, 1999b). For a 3 dimensional 1 particle 1 triplet anomalous diffusion model, the ACF is written as:

$$G(\tau)=\frac{1}{N}\cdot g_{trip}\cdot\left[1+\left(\frac{\tau}{\tau_d}\right)^{\alpha}\right]^{-1}\left[1+\frac{1}{K^2}\left(\frac{\tau}{\tau_d}\right)^{\alpha}\right]^{-1/2}+G_{\infty} \tag{4.1}$$

with $g_{trip}=1+\left(\frac{F_{trip}}{1-F_{trip}}\right)\cdot\exp\left(-\tau/\tau_{trip}\right)$ (4.2)

For a 2 dimensional 1 particle 1 triplet anomalous diffusion model, the ACF is written as:

$$G(\tau) = \frac{1}{N} \cdot g_{trip} \cdot \left[1 + \left(\frac{\tau}{\tau_d} \right)^{\alpha} \right]^{-1} + G_{\infty} \qquad (4.3)$$

In this section, we fitted our FCS measurements with the anomalous subdiffusion model and compared the value of the anomality factor α. We first evaluated data from experiments performed in PBS buffer. Both fluorescein and EGFP in PBS buffer yielded α value close to 1 (Table 4.1), confirming that diffusion of molecule in buffer solutions follows the pattern of Brownian motion. We then examined EGFP diffusion in motor neuron cells (including cytoplasm, nucleoplasm and cytoplasm from Cxcr4b-MO motor neuron cells) and muscle fiber cytoplasm. Interestingly, although the diffusion coefficients variance covers a relatively wide range, i.e. EGFP diffuses about 60% slower in muscle fiber cytoplasm than in motor neuron nucleoplasm, the anomality factor α shows little variations between different cell types, different subcellular compartments, and cells in different states (Table 4.1). The obtained α values were close to 0.7 in all cases. The results first verified that the diffusion of soluble protein inside cells is indeed anomalous (α~0.7). It also suggested that the degree of macromolecular crowding in living cells is generally conserved (Guigas et al, 2007a). As shown by Guigas and Weiss via computer simulations, the anomalous subdiffusion actually increases the probability for proteins to find a nearby target (Guigas & Weiss, 2007). The similar anomality factors in living cells thereby suggested a conserved dynamics in intracellular protein reaction networks. At last, we evaluated the FCS data of Cxcr4b-EGFP on

membrane, and the obtained α value was 0.46 ± 0.10. This value is considerably smaller than the cytoplasm and nucleoplasm data, suggesting that the diffusion on a cell membrane is more obstructed. It should be noted that the size of the probe particle greatly affects the obtained anomality factor values (the diameter of EGFP molecule is roughly 2.1 nm (Liang et al, 2009)), as diffusion of larger probes experience more obstruction inside cells. Fluorescently labeled beads with a diameter of ~ 6 nm showed stronger anomalous subdiffusion in Hela cells with α~0.55 (Guigas et al, 2007a).

Table 4.2: Translational diffusion measurements in zebrafish embryos

Sample	τ_d ± SD (ms)	D ± SD (μm^2 s^{-1})	α ± SD	Sample size
Fluorescein in PBS buffer	0.043 ± 0.002	300*	0.97 ± 0.02	10
EGFP in PBS buffer	0.19 ± 0.02	69.1 ± 7.3	0.95 ± 0.02	20
EGFP in motor neuron cytoplasm	0.29 ± 0.06	45.3 ± 9.4	0.71 ± 0.04	60
EGFP in motor neuron nucleoplasm	0.23 ± 0.03	57.1 ± 7.5	0.74 ± 0.06	40
EGFP in Cxcr4b-MO motor neuron cytoplasm	0.35 ± 0.05	37.5 ± 5.4	0.72 ± 0.05	60
EGFP in muscle fiber cytoplasm	0.36 ± 0.04	36.5 ± 4.1	0.76 ± 0.07	80
Cxcr4b-EGFP on muscle fiber membrane	22.1 ± 7.1	0.60 ± 0.19	0.46 ± 0.10	20

*literature value (Wohland et al, 1999)

Chapter 5

Determination of Dissociation Constants in Living Zebrafish Embryos with SW-FCCS

5.1 Introduction

The quantification of biological interactions is very important in life sciences. Recent advances in molecular and cell biology show that protein-protein interactions, at the molecular level, are the essence of most biological processes. Consequently, the protein-protein interaction becomes the main focus in pharmaceutical targeting as a drug is efficient only when it is bound to, and modulates the function of, its macromolecular targets. However, the quantification of biomolecular interactions, at present, is mostly performed *in vitro*, i.e. the protein microarray in scientific research (Stoll et al, 2005) and high throughput screen in pharmaceutical industry (Pereira & Williams, 2007). In the last years, it became apparent, though, that biomolecular interactions are strongly dependent on their environment, the conditions of molecular crowding (Raghunath et al, 2007), concentration of

reactants (Wylie et al, 2007a) and the 3D organization of cells in which measurements are taken. It therefore became increasingly important to quantify biological parameters, in particular biological interactions, in their natural environment within multi-cellular organisms. In this chapter, we demonstrate, for the first time to our knowledge, the measurement of dissociation constants of interacting proteins in living zebrafish embryos, using SW-FCCS.

In this chapter, we investigated the interaction between Cdc42 (cell division cycle 42) and IQGAP1 (IQ motif containing GTPase activating protein 1). Cdc42, a small GTPase that belongs to the Rho/Rac subfamily, regulates various cellular responses including the assembly and disassembly of the actin cytoskeleton. It interacts with over 20 target proteins identified to date, among them IQGAP1 (Hart et al, 1996; Kuroda et al, 1996), a multidomain scaffolding protein that modulates cross-talk among diverse pathways. The interaction of IQGAP1 and Cdc42 plays an important role in modeling microtubule and cytoskeleton during cell polarization and migration (Watanabe et al, 2004).

5.2 System Calibration

As discussed in Section **2.2.2**, in order to quantify concentrations from SW-FCCS measurements, several parameters need to be determined beforehand: the count rate per particle per second (*cps*) of fluorophores in different channels (η_g^g, η_g^r, η_r^g and η_r^r), background intensities in different channels (β^g and β^r), correction factors (q_g and q_r), and effective volume (V_{eff}). A calibration of the SW-FCCS instrument was also performed using Rhodamine 6G (R6G).

5.2.1 Determination of *cps*, background, and correction factors

The *cps* of EGFP tagged particles in green and red channels, η_g^g and η_g^r, was obtained from the division of the average intensity counts in each channel with the number of EGFP tagged particles obtained from curve fitting. This was done in experiments with only EGFP tagged protein and excited with 514 nm laser line. The measured *cps* was corrected for background as it affects the actual number of particles (Schwille et al, 1999a). Similarly, η_r^g and η_r^r was determined in experiments with only mRFP tagged protein with 514 nm excitation. The individual *cps* was an average of at least 20 measurements of such experiments. Depending on different fusion proteins, η_g^g and η_r^r ranged 900-1600 Hz in zebrafish embryos (Table 5.1). The *cps* values in SW-FCCS measurements were considerably lower

compared to that of EGFP excited with 488 nm laser line (~ 6 kHz as shown in section **3.3.4**). This was due to the inefficient excitation of both EGFP and mRFP using single 514 nm laser line, as well as inefficient collection of EGFP fluorescence at 545 nm rather than at emission maximum of 510 nm (Fig. 2.3).

Fluorescence crosstalk is inevitable for the use of FPs. This is especially influential in SW-FCCS measurements as the emission spectra of EGFP and mRFP are not distinctly separated. The crosstalk from the green channel to the red channel is stronger than the crosstalk from the red channel to the green channel due to the long-tailed emission spectra of FPs. In our calibration, the EGFP crosstalk to the red channel η_g^r is about 9-11 % of η_g^g and the mRFP crosstalk to the green channel η_r^g is about 1-2 % of η_r^r. The average background intensities in both channels β^g and β^r are recorded in experiments in wild type zebrafish embryos, and the value obtained using 514 nm excitation are around 500 Hz. In our positive control of tandem mRFP-EGFP experiment (see section **5.3** below for detail), η_g^g was noticeably lower and η_r^r higher than EGFP or mRFP alone (Table 5.1). One possible explanation is due to fluorescence energy transfer as in the positive control EGFP and mRFP are separated with only seven amino acids. Hence correction factors of q_g = 0.7, q_r = 1.3 were used for the positive control. In other binding experiments of mRFP-Cdc42 and EGFP-IQGAP1, we do not see such changes in *cps* and hence q_g and q_r = 1 were used instead.

Table 5.1: Molecular brightness obtained from calibration.

Sample	η_g^g (Hz)	η_r^r (Hz)
mRFP, EGFP	1250	1230
mRFP, EGFP-IQGAP1	1220	1230
mRFP-EGFP	920	1580
mRFP-Cdc42^{G12V}, EGFP-IQGAP1	1220	1180
mRFP-Cdc42^{T17N}, EGFP-IQGAP1	1220	1200

5.2.2 Determination of the Effective Volume

The true value of the effective volume is difficult to measure as it relies on experimental conditions such as refractive index of the solvent, the photophysics of the fluorophore under investigation, and coverglass thickness (Enderlein et al, 2005). Several approaches have been proposed for an estimation, i.e. through FCS analysis of sample with known concentration or known diffusion coefficient, fitting a theoretical curve to the experimental data, or using nanometric fluorescent beads (for a comparison of these methods, see Ruttinger et al, 2008). We used the first approach via FCS measurement and fit of a fluorophore with known diffusion coefficient. Diffusion time τ_d and the geometric ratio of axial to radial dimensions $K = z_0/\omega_0$ can be obtained from curve fittings. According to Eq. 2.19 ($\tau_d = \frac{\omega_0^2}{4D}$)

with known diffusion coefficient, effective volume $V_{eff} = \pi^{3/2}\omega_0^2 z_0$ can thus be calculated. Rhodamine 6G (R6G) with a diffusion coefficient of 426 $\mu m^2/s$, as reported in recent literature (Petrasek & Schwille, 2008b), was used. For a 514 nm laser line excitation the V_{eff} was determined to be 0.56 ± 0.06 fL.

5.2.3 Instrument Calibration

10 nM R6G was also used to calibrate the SW-FCCS system. R6G can be efficiently excited with 514 nm laser line, and due to the broad emission spectrum, the fluorescence can be captured in two channels by filter set used in SW-FCCS measurement (560DCLP, 545AF35 and 615DF45). Fig. 5.1 shows the spectra of R6G together with emission filters, and the SW-FCCS measurements of R6G. The CCF from the two channels reaches a maximum and lies between the green and red ACFs, and the complex percentage calculated is 92% using the green channel data and 110% using the red channel data. A 100% overlap between the three correlation functions is not achieved due to the different molecular brightness, background and detection volumes in the green and red channels.

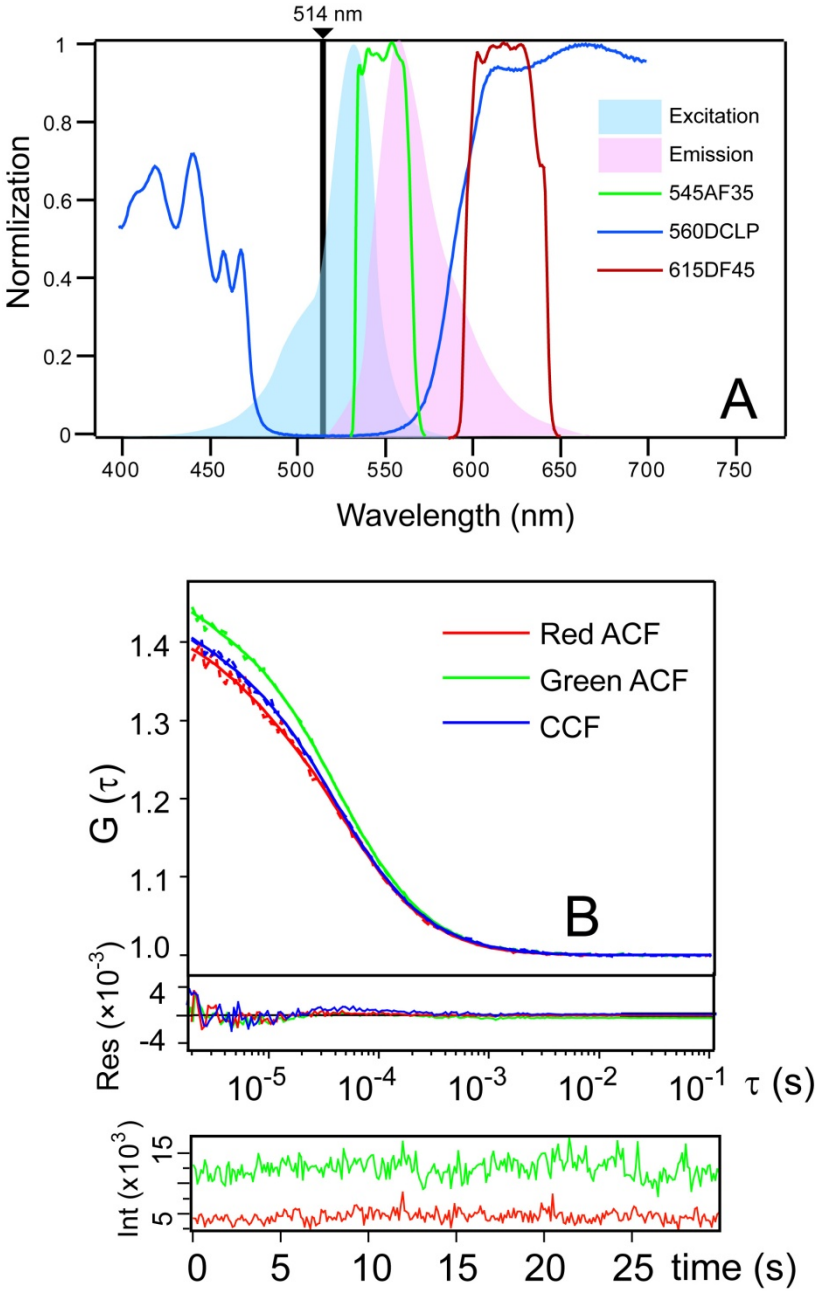

Fig. 5.1: System calibration using Rhodamine 6G. A) Excitation and emission spectra of Rhodamine 6G, showing together with dichroic mirror and emission filters. Rhodamine 6G can be properly excited at 514 nm, and due to the broad emission spectrum, the fluorescence can be split into two channels and detected separately (545 nm and 615 nm as used in our SW-FCCS instrument). B) SW-FCCS results of 10 nM Rhodamine 6G showing both experimental curves (dashed lines) and fitting curves (solid lines). In the middle are the fitting residuals of each curve fitting and at the bottom is the intensity traces.

5.3 Control Measurements

5.3.1 Mixture of mRFP and EGFP as Negative Control

Negative controls were tested first in zebrafish embryos. As a negative control, we injected premixed EGFP and mRFP plasmids into one blastomere at 16-cell stage (see section **2.3.1** for detail). The mRFP and EGFP are individually expressed and molecular binding should not be present. Both plasmids have the same human cytomegalovirus (CMV) immediate early promoter, but the expression efficiency of EGFP is higher than that of mRFP. In order to achieve 1:1 protein expression level, a mixture ratio of 1:3 of EGFP and mRFP was used in the negative control. Due to the mosaic expression patterns, different levels of green and red fluorescence were recorded in various cell types at 48 hours postfertilization (hpf). SW-FCCS measurements were performed in selected muscle fiber cells that express both EGFP and mRFP at a similar level based on imaging. Confocal imaging was also used to select cells with physiological expression level of EGFP and mRFP at nanomolar range (see discussion at section **3.3.4**). As shown in Fig.5.2A, both EGFP and mRFP are homogenously expressed within the whole muscle fiber cells. Noticeably, the mRFP seems to be concentrated in the nucleus due to unknown reason and subsequent SW-FCCS measurements avoided this region. The SW-FCCS results show a flat CCF (Fig. 5.2B), indicating a lack of interaction between individually expressed EGFP and mRFP molecules. As discussed in **2.2.2** and **2.2.3**, the concentrations of each particle can be calculated from SW-FCCS measurements, and the complex percentage obtained for the negative control is 6.2 ± 4.8 %. This

value is not 0 % due to the autofluorescence background producing false-positive cross-correlation amplitudes and this sets a lower limit for the negative control. It should be noted that curve fitting could also influence the calculated complex percentage values. In this work, both green and red ACF experimental curves were fitted with 3 dimension 1 particle 1 triplet state model (3D1P1T), while CCFs were fitted with 3 dimension 1 particle model (3D1P) as triplet states of EGFP and mRFP do not correlate theoretically. However, due to 10% of spectral crosstalk of EGFP to mRFP channel, some CCF curves also possess substantial triplet state and curve fitting in this case gave false-positive number of particles. Taking this into consideration, curve fitting was performed with limited time range from 100 μs to 1s, avoiding the triplet state time range of ~10 μs.

As another negative control, we injected premixed mRFP and EGFP-IQGAP1 plasmids. The ratio between EGFP-IQGAP1 and mRFP was tested and set at 1:1 for similar protein expression level. The molecular mass of EGFP-IQGAP1 is 220 kDa, which is substantially larger than mRFP (32 kDa, Campbell et al, 2002b), and the two proteins are not supposed to bind. Interestingly, the confocal image suggests that EGFP-IQGAP1 is not present in the nucleus, in contrary to mRFP as shown in Fig. 5.2E, possibly due to its large size (There are multiple nuclei within a single muscle fiber cell, which are located in the peripheral aspect of the cell, just under the plasma membrane.) SW-FCCS measurements were conducted in the cytoplasm and one result was shown in Fig. 5.2F. Firstly as expected, The CCF is flat compared to both green and red ACFs, suggesting lack of interaction between the two proteins. The complex percentage calculated is only 2.7 ± 2.0 %, lower than the mRFP and

EGFP pair. Secondly, the SW-FCCS result shows that the green and red ACFs differ substantially in time scale. The diffusion time of mRFP and EGFP-IQGAP1 are 1.01 ± 0.24 ms and 7.0 ± 2.1 ms, respectively. This is another obvious indication of lack of interaction between the two proteins, as interacting partners should possess similar diffusion times.

5.3.2 mRFP-EGFP Tandem Construct as Positive Control

As a positive control, we injected an mRFP-EGFP tandem construct in which mRFP and EGFP are linked by a 7 amino acids linker. The confocal image shows the same homogenous expression of both green and red fluorescence (Fig. 5.2C) as in the negative control. Imaging based analysis of colocalization in this case cannot distinguish negative and positive controls. The cell selection criterion for SW-FCCS measurements was same as in negative control and one SW-FCCS result was shown in Fig. 5.2D. The SW-FCCS result gave elevated CCF amplitudes, indicating the correlated movement of mRFP-EGFP. The complex percentage obtained for positive control was 44.9 ± 5.9 %. This value is considerably higher than the negative control (6.2 ± 4.8%) but much lower compared to the R6G calibration result. It is also noticeable from Fig. 5.2D that the amplitude of red ACF is higher than that of green ACF, indicating fewer particles in red channel than in green channel. One reason is that some of the FPs are non-fluorescent. Hillesheim et al. (Hillesheim et al, 2006) showed that about 60 % of the mRFP can reside in a dark state using dual-color

photon counting histogram and life-time measurements. Maeder et al. (Maeder et al, 2007) also indicated that about 50 % of mCherry is non-maturated during their experiment and mRFP may suffer from similar effects. In addition, photobleaching of FPs (especially mRFP) may, too, lead to a decrease in complex percentage of the positive control. Thus the complex percentage of 44.9 ± 5.9 % sets the upper limit for the EGFP and mRFP pair under the presented conditions. Similar values for tandem FPs have been reported by others (Baudendistel et al, 2005; Kohl et al, 2005; Saito et al, 2004; Slaughter et al, 2007).

It is also interesting to compare the diffusion times obtained in green and red channels. As a tandem construct, the EGFP and mRFP are supposed to have the same diffusion time. But the results suggest that EGFP diffuses 16% faster than mRFP (Table 5.2). This is also observed in the negative control where EGFP diffuses 32% faster than mRFP (Table 5.2), although EGFP (27 kDa, Tsien, 1998) has similar molecular mass as mRFP (32 kDa, Campbell et al, 2002b) and the two share similar structure. This is due to the different sizes of effective volumes of green and red channels. Although a single 514 nm laser was used to excite both EGFP and mRFP, the effective volume V_{eff} is intrinsically wavelength dependant and the V_{eff} in the red channel (645 nm) is theoretically larger than V_{eff} in the green channel (595 nm). In addition, data fitting could also introduce error in obtained diffusion time values, as mRFP possesses higher percentage of triplet state (~45%) than EGFP (~10%) and the fitting of triplet state times can substantially affect the fitting of diffusion times. Nevertheless, the difference is relatively small and a single V_{eff} value was used during quantification as discussed in **2.2.2**.

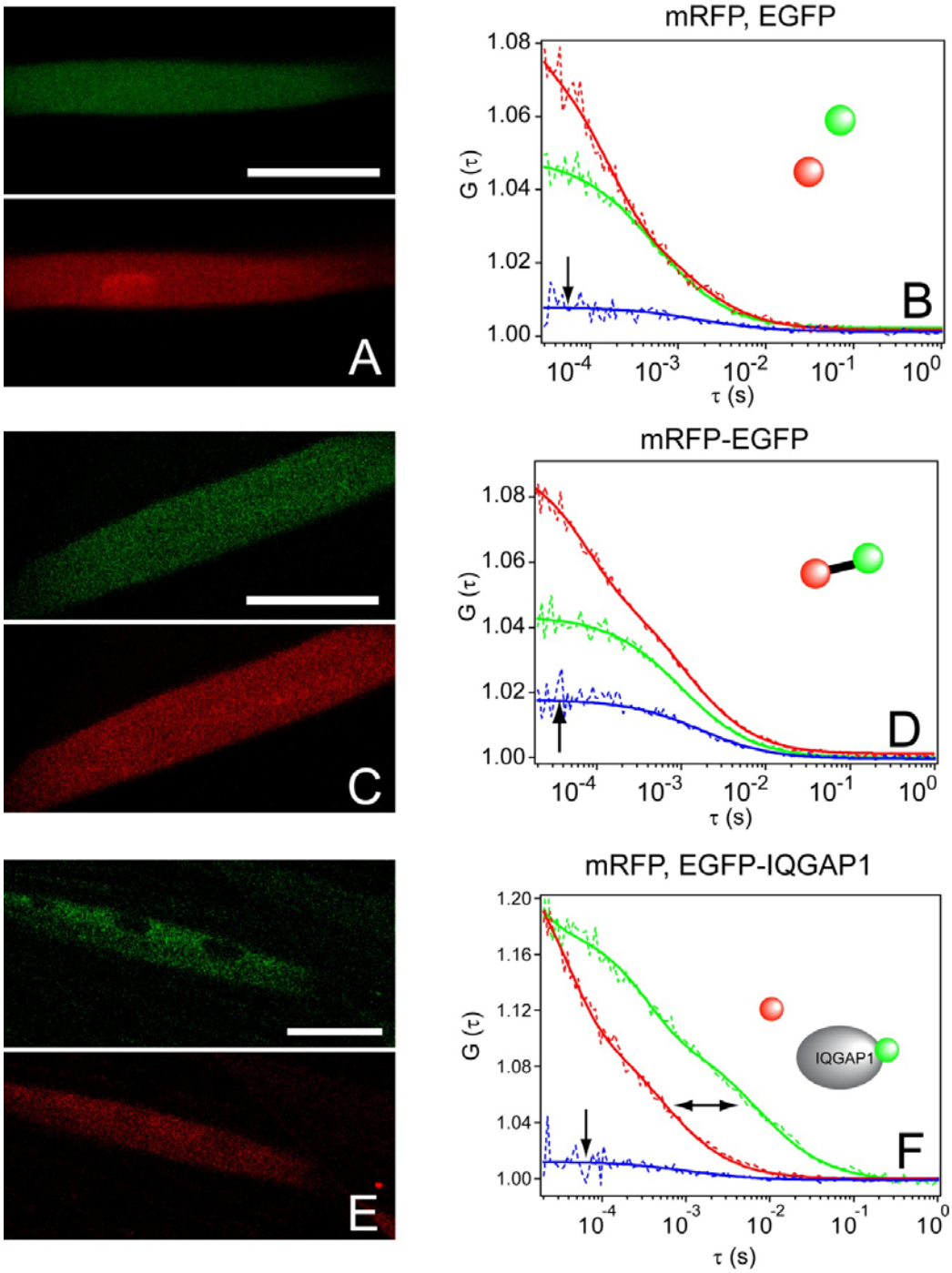

Fig. 5.2: SW-FCCS control measurements in living zebrafish embryos. A) Confocal pictures of green and red channels of one muscle fiber cell that express negative control (individually expressed EGFP and mRFP). B) SW-FCCS results of negative control showing both experimental curves (dashed lines) and fitting curves (solid lines). Inserts are schematic drawing the sample. C) and D) Confocal pictures and SW-FCCS results of positive control (tandem construct of mRFP-EGFP). E) and F) Confocal pictures and SW-FCCS results of another negative control (individually expressed mRFP and EGFP-IQGAP1). Scale bar = 20 µm.

Using concentrations obtained from SW-FCCS measurements, we also showed here the scattering plot of $C_g \times C_r$ vs C_{gr} for both positive and negative controls (Fig. 5.3. C_g, C_r and C_{gr} represent the concentration of the red particle, the green particle and the green-red complex, respectively). The scattering plot method was used in the following sections to calculate the dissociation constants of interacting proteins (See section **5.4.2** for detail). Assuming that a proportion of both EGFP and mRFP are non-florescent, we have simulated the scattering plot for positive and negative controls (unpublished data) and our experimental curves (Fig. 5.3) fit the simulation results.

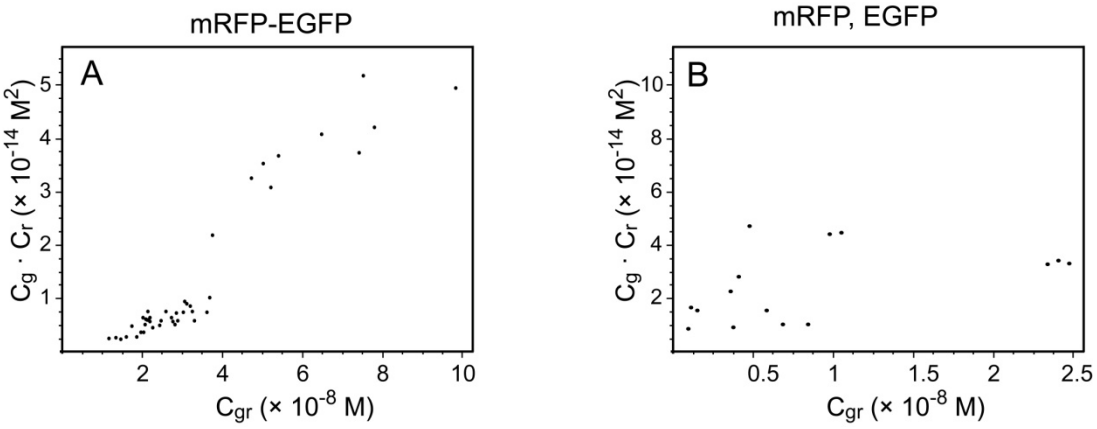

Fig. 5.3: Scattering plot of $C_g \times C_r$ vs C_{gr} for both positive and negative controls. A) Scattering plot for positive control of tandem construct of mRFP-EGFP. The correlation is obvious and the curve fits our simulation results. B) Scattering plot for negative control of individually expressed mRFP and EGFP.

5.4 Interaction of Cdc42 and IQGAP1

5.4.1 Introduction

IQGAP1 is a member of the IQGAP (IQ motif containing GTPase activating protein) family of eukaryotic proteins, which have been found in yeast, worms and mammals. IQGAP1 acts as a scaffolding protein that binds to, and regulates the function of, a diverse array of signalling and structural molecules, including Ca^{2+}/calmodulin signalling, cytoskeletal architecture, Cdc42 signaling, E-cadherin-mediated cell-cell adhesion and β-catenin mediated transcription (for reviews, see Brandt & Grosse, 2007; Briggs & Sacks, 2003a; Briggs & Sacks, 2003b). The 190 kDa human IQGAP1 protein contains five protein-interacting domains (Fig. 5.4). Starting from the N-terminus is the calponin homology domain (CHD) that binds to F-actin (Erickson et al, 1997). Next is the WW domain, an interaction module for proline-rich ligands (Macias et al, 2002). The name of IQGAP comes from the next two motifs, the IQ and Ras GTPase-activating protein (GAP)-related domain. The IQ domain is a tandem repeat of four IQ motifs which bind to calmodulin (Hart et al, 1996). The GAP-related domain (GRD) regulates the binding of Rho GTPases, Cdc42 and Rac (Hart et al, 1996; Ho et al, 1999; Joyal et al, 1997). At the C-terminus is the RasGAP domain which interacts with the microtubule-binding protein, E-cadherin (Kuroda et al, 1998), and β-catenin (Briggs et al, 2002).

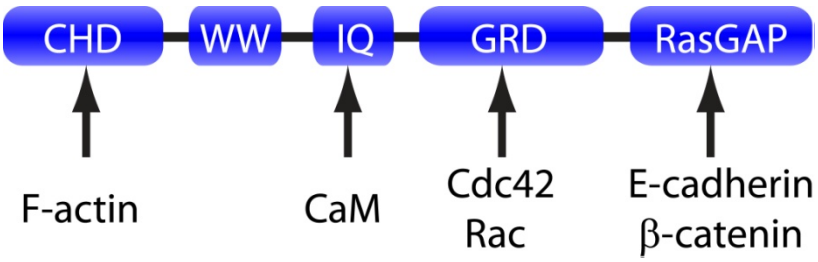

Fig. 5.4: Five protein-interacting domain of IQGAP1. Starting from the N-terminus: the calponin homology domain (CHD) that binds to F-actin; the WW domain; the IQ domain that binds to calmodulin (CaM); the GAP-related domain (GRD) that binds to Cdc42 and Rac; and the RasGAP domain that binds to E-cadherin and β-catenin.

In this work, we aim to quantify the interaction between IQGAP1 and Cdc42, which plays an important role in modelling microtubule and cytoskeleton during cell polarization and migration (Watanabe et al, 2004). Initial study identified IQGAP1 as a putative effector protein for Cdc42 (Hart et al, 1996; Kuroda et al, 1996). Subsequent reports validated the biological significance of this interaction. It has been shown that overexpression of IQGAP1 increases active Cdc42 in cells, leading to the formation filopodia (Swart-Mataraza et al, 2002). In addition, IQGAP1 seems to be necessary for Cdc42 to localize to the plasma membrane, and promotes cell mobility at least part in Cdc42 function (Swart-Mataraza et al, 2002). *In vitro* measurements have already been conducted to determine the dissociation constant between IQGAP1 and Cdc42. In the only example we can find from literature, a K_D of 24 nM was reported for the interaction between $Cdc42^{Q61L}$, a Cdc42 mutant considered as an active form, and the C-terminal half of IQGAP1 that contains only the GRD and RasGAP domains (Owen et al, 2008). However, it became increasingly apparent recently that binding of some partner protein to IQGAP1

affects the binding of other associated proteins, at least *in vitro* (Fig. 5.5). Binding of Ca^{2+}/calmodulin to IQGAP1 has been shown to promote dissociation of F-action from IQGAP1 (Mateer et al, 2002). The increased intracellular Ca^{2+} concentration promote binding of calmodulin to IQGAP1, which leads to conformational change of IQGAP1 and possibly caused the dissociation of F-actin (Fig.5.5). More importantly, it has been shown that the binding of Ca^{2+}/calmodulin also decrease the affinity of Cdc42 to IQGAP1 (Ho et al, 1999). In this case, the study of interaction of Cdc42 and C-terminus IQGAP1 cannot reflect the actual binding affinity between these two proteins in their physiological environment. In this section, we measured the apparent K_D value between Cdc42 and the full length IQGAP1 in living zebrafish embryos and the results are compared to that in CHO cells. Cdc42 and IQGAP1 DNA used in this work are of *Homo sapiens* origin. BLAST analysis against *Danio rerio* RefSeq Protein database reveals proteins with 99% similarity to Cdc42 （Ref: NP_956926.1） and 87% to IQGAP1 (Ref: XP_001920847.1). In particular, the functional domains of IQGAP1 share even higher similarity: 97% of similarity of the GRD domain (Ref: XP_001920847.1), 96% of similarity of the CHD domain, and 83% of similarity of the IQ domain. So we assume that the function of both proteins is conserved in zebrafish. Two Cdc42 mutants were used in this work: the constitutively active $Cdc42^{G12V}$ which is in a predominantly GTP-bound form and the dominant-negative GDP-bound $Cdc42^{T17N}$.

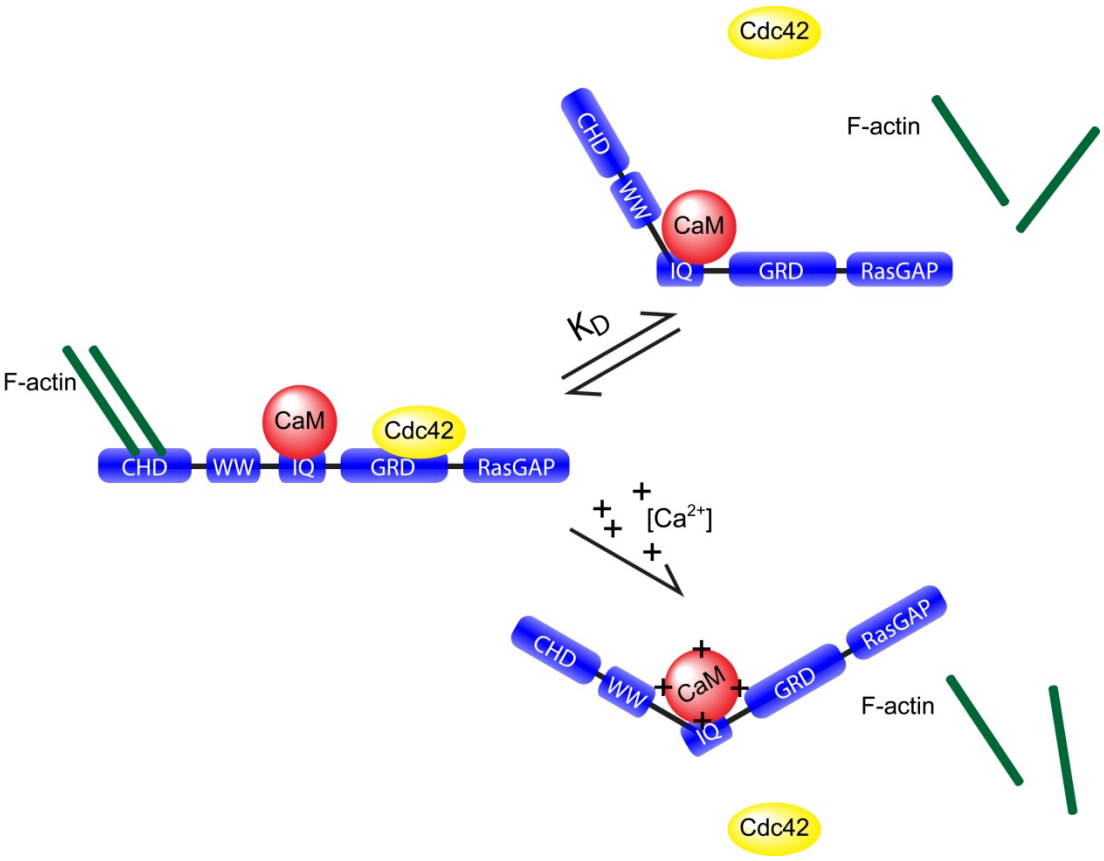

Fig. 5.5: Interaction of IQGAP1 with Cdc42 and F-actin. The N-terminus CHD domain binds to F-action; the IQ domain at the center binds to calmodulin (CaM); and the GRD domain binds to Cdc42. Increased intracellular Ca^{2+} concentration promote binding of calmodulin to IQGAP1, which leads to conformational change of IQGAP1, and possibly dissociation of F-actin and Cdc42 from IQGAP1.

5.4.2 Interaction of $Cdc42^{G12V}$ and IQGAP1

We first examined the protein pair of IQGAP1 and $Cdc42^{G12V}$, a constitutively active mutant that has been shown to bind to IQGAP1 (Kuroda et al, 1996). The G12V mutant inhibits the hydrolysis of GTP hence locking the protein in the active form (Masters et al, 1990). The EGFP and mRFP genes were attached to IQGAP1 and $Cdc42^{G12V}$ DNA respectively and constructed plasmids were co-injected at 16-cell

stage. The DNA mixture ratio of 1:3 of EGFP-IQGAP1 to mRFP-Cdc42^{G12V} was used to obtain 1:1 protein expression ratio. The plasmid injection amount was controlled and muscle fiber cells that express both EGFP-IQGAP1 and mRFP-Cdc42^{G12V} at physiological level (nanomolar range) were selected for SW-FCCS measurements. From the confocal image (Fig. 5.6A), it is clear that both EGFP-IQGAP1 and mRFP-Cdc42^{G12V} were not present in the nucleus due to large protein size, and subsequent SW-FCCS measurements were performed in the cytoplasm. Fig. 5.5B shows one example of such results. It is obvious that the two proteins form complexes, as shown by the elevated CCF amplitude, and the complex percentage calculated is 41.6 ± 9.2 %. This value is very close to the mRFP-EGFP positive control, indicating that the Cdc42^{G12V} binds strongly to IQGAP1 as expected. It should be noted that IQGAP1 might also indirectly bind to another Cdc42 molecule, through neural-Wiskott-Aldrich syndrome protein (N-WASP). Recent studies suggest that IQGAP1 interacts and activates N-WASP to stimulate actin polymerization to generate branched actin filaments *in vitro* (Bensenor et al, 2007; Le Clainche et al, 2007), although which IQGAP1 domains are responsible for the binding is still unclear. The N-WASP protein also possesses a GRD domain that binds to Cdc42, so the IQGAP1 and N-WASP complex might contain two Cdc42 molecules. However, this hypothesis needs to be experimentally verified, and in this work, the 1:1 binding stoichiometry was assumed for quantification.

The relative proportion of molecules forming a complex depends greatly on the relative expression levels of the two fusion proteins and their dissociation constant K_D. The concentrations of both bound (C_{gr}) and free (C_g for EGFP-IQGAP1 and C_r for

mRFP-Cdc42^{G12V}) proteins can be calculated from the ACF and CCF functions as discussed in **2.2.2**. A scattering plot of the product $C_g \times C_r$ against C_{gr} was then generated (Fig. 5.7A) and the K_D value determined using this method is 105 ± 11 nM, also suggesting a strong interaction. It should be noted that this value is an apparent K_D since endogenous proteins, FPs in dark states, FPs photobleaching, and interactions with other cellular proteins can influence concentration of the detected complexes. Nevertheless, the apparent K_D value is a useful measure since it reflects more closely the actual binding between proteins in their physiological environment.

Recently, Maeder et al. have shown that apparent K_D measurements are possible by FCCS in yeast cells using an alternative evaluation scheme (Maeder et al, 2007). The individual K_D values of each measurement were plotted in a histogram and fitted to a log-normal distribution (Fig. 5.7B). The log-normal distribution has been suggested to extract more reliably data for skewed normal distributions, often found in biological samples, when mean values are low, variance is large and values are restricted to positive numbers (Limpert et al, 2001). The K_D obtained using this method is 79 nM, in good agreement with results above. Thus we suggest that the apparent K_D for the interaction of Cdc42^{G12V} and IQGAP1 in muscle fiber cells of living zebrafish embryo is ~100 nM. This value is reasonable compared to the 24 nM *in vitro* measurement between another active form of Cdc42 and C-terminus IQGAP1 (Owen et al, 2008).

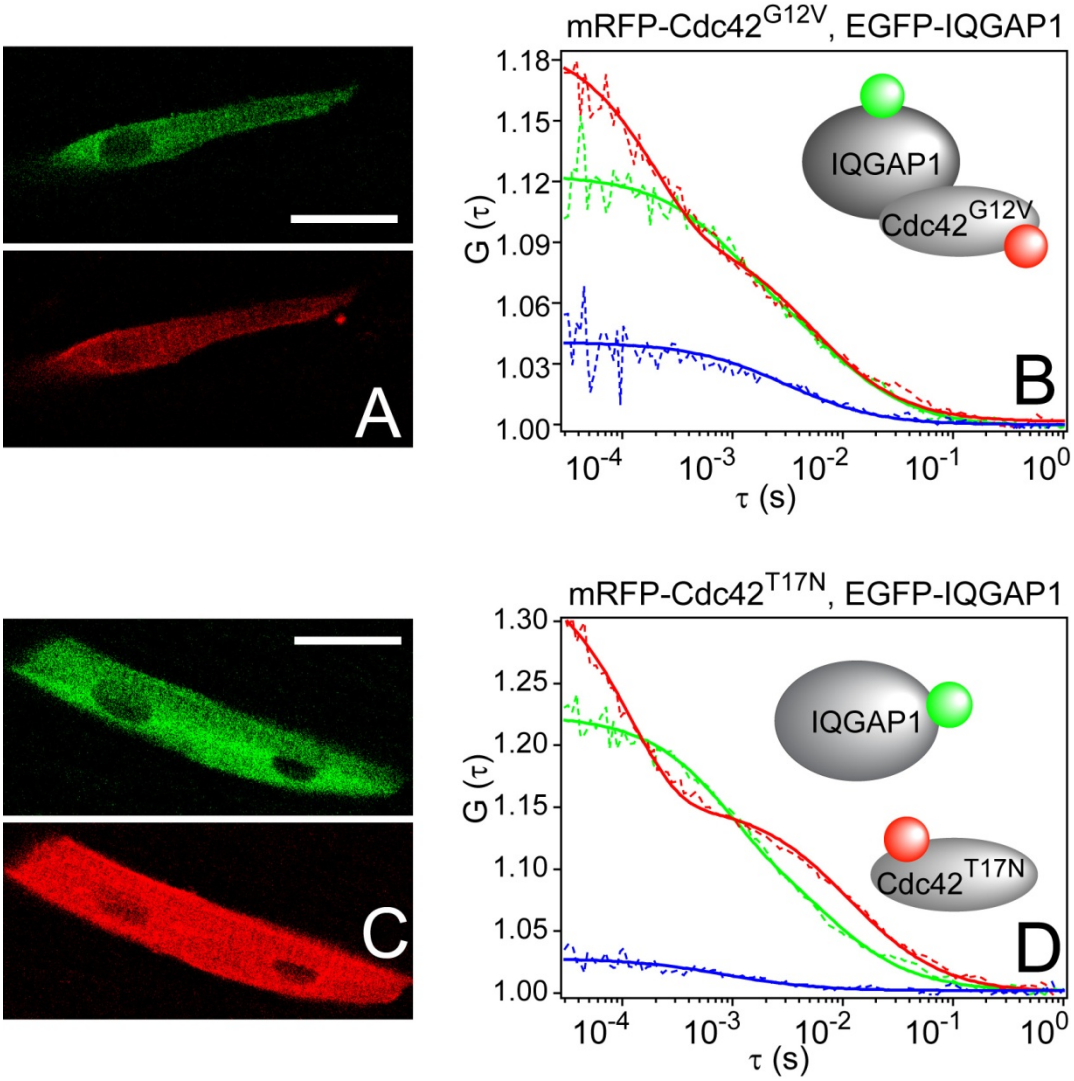

Fig. 5.6: SW-FCCS measurements of Cdc42 and IQGAP1. A) Confocal pictures of one muscle fiber cell that expresses mRFP-Cdc42^{G12V} (red channel), an active mutant of Cdc42, and EGFP-IQGAP1 (green channel). B) SW-FCCS results of the interacting protein pair of mRFP-Cdc42^{G12V} and EGFP-IQGAP1, showing both experimental curves (dashed line) and fitting curves (solid line). Inserts are schematic drawing of the sample. C) and D) Confocal pictures and SW-FCCS result of the protein pair of mRFP-Cdc42^{T17N} and EGFP-IQGAP1. Scale bar = 20 µm.

5.4.3 Interaction of Cdc42^{T17N} and IQGAP1

We next examined the protein pair of IQGAP1 and Cdc42^{T17N}. Cdc42^{T17N}, a frequently used dominant-negative mutant, has been shown to have no interaction with IQGAP1 using *in vitro* methods (Erickson et al, 1997). The DNA mixture ratio of 1:2 of EGFP-IQGAP1 to mRFP-Cdc42^{T17N} was used to obtain 1:1 protein expression ratio. One confocal image and one SW-FCCS result are shown in Fig. 5.6C and Fig. 5.6D, respectively. The confocal image suggests the same expression patterns as in Cdc42^{G12V} and IQGAP1 measurements. However, the SW-FCCS results are noticeably different. The blue CCF curve was basically flat, indicating lack of interaction. Nevertheless, in our measurement of mRFP-Cdc42^{T17N} with EGFP-IQGAP1 in zebrafish embryos, about one third of the measurements show some degree of cross-correlation and the portion of molecules forming a complex was 12.6 ± 12.3 % in this subpopulation. Based on this one third of measurements, K_D determination using a line plot and the log normal distribution histogram were performed as shown in Fig. 5.7C and Fig. 5.7D. However, there is generally no correlation for the line plot and the histogram suggests a random distribution. The scattering line plot and histogram were force fitted and the K_D value determined is 1500 nM, indicating very weak interaction. Considering the large standard deviation of the complex percentage value and that interactions could be seen only in about one third of the measurements, we suggest that Cdc42^{T17N} does not bind to IQGAP1 or binds very weakly. The distinct mobility of mRFP-Cdc42^{T17N} and EGFP-IQGAP1 (Fig. 5.6D and Table 5.2) also indicates that the majority of the two proteins diffuse separately, which is in contrast to the similar diffusion times found for the interacting pair of mRFP-Cdc42^{G12V} and EGFP-IQGAP1. Interestingly, the small size mRFP-Cdc42^{T17N} (~ 55 kDa) diffuses more slowly in the cytoplasm than EGFP-IQGAP1 (~220 kDa), and

even slower than the $Cdc42^{G12V}$-IQGAP1 complex measured in the previous section (Table 5.2), which suggests that the dominant-negative $Cdc42^{T17N}$ interacts and forms complexes with other proteins. One possible target are guanine nucleotide exchange factors (GEFs), which bind strongly to GDP-bound Cdc42 but have low binding affinity to GTP-bound Cdc42 (Rossman et al, 2005). Cdc42, as a Rho-GTPase, functions as bi-molecular switches by adopting different conformational states in response to binding GDP or GTP (for review, see Heasman & Ridley, 2008). Cycling between GDP- and GTP-bound states is controlled primarily by two classes of regulatory molecule: GAPs, which suppress Cdc42 activity, and GEFs, which catalyse the exchange of GDP for GTP and promote Cdc42 activity. Biochemical studies show that, in response to external signals originating from cell surface receptors and cell adhesion molecules, GEFs engage Cdc42 and form macromolecular complexes with scaffolding proteins and/or kinases (Cerione, 2004). Owing to the relative high concentration of intracellular GTP in normal cells, GDP-bound Cdc42 rapidly transferred to GTP-bound form and free GEFs. However, the $Cdc42^{T17N}$ mutants are predominantly in the GDP-bound forms, thus a large proportion is probably still in the form of GEF-Cdc42 complexes, causing slow diffusion of measured mRFP-$Cdc42^{T17N}$.

The dominant-negative T17N mutation in Cdc42 is in analogy to the S17N mutation (Coso et al, 1995) of H-Ras, a Ras-GTPase. In H-Ras, it has been shown that the S17N mutation decreased the affinity for GTP 20 to 40 fold without significantly affecting its affinity for GDP (Feig & Cooper, 1988). Hence the mutant binds preferably to GDP causing it to be in an inactive state. $H\text{-}Ras^{S17N}$ is still able to bind GTP, however

the GTP-bound form fails to activate a model downstream target (Farnsworth & Feig, 1991). The same is assumed to be true for Cdc42^{T17N}. Furthermore, it has been shown that IQGAP1 increases the amount of GTP-bound Cdc42 in mammalian cells and results in filopodia formation (Swart-Mataraza et al, 2002). Thus the possible weak interaction observed between IQGAP1 and Cdc42^{T17N} might be due to the subpopulation of GTP-bound Cdc42^{T17N} being stabilized by IQGAP1.

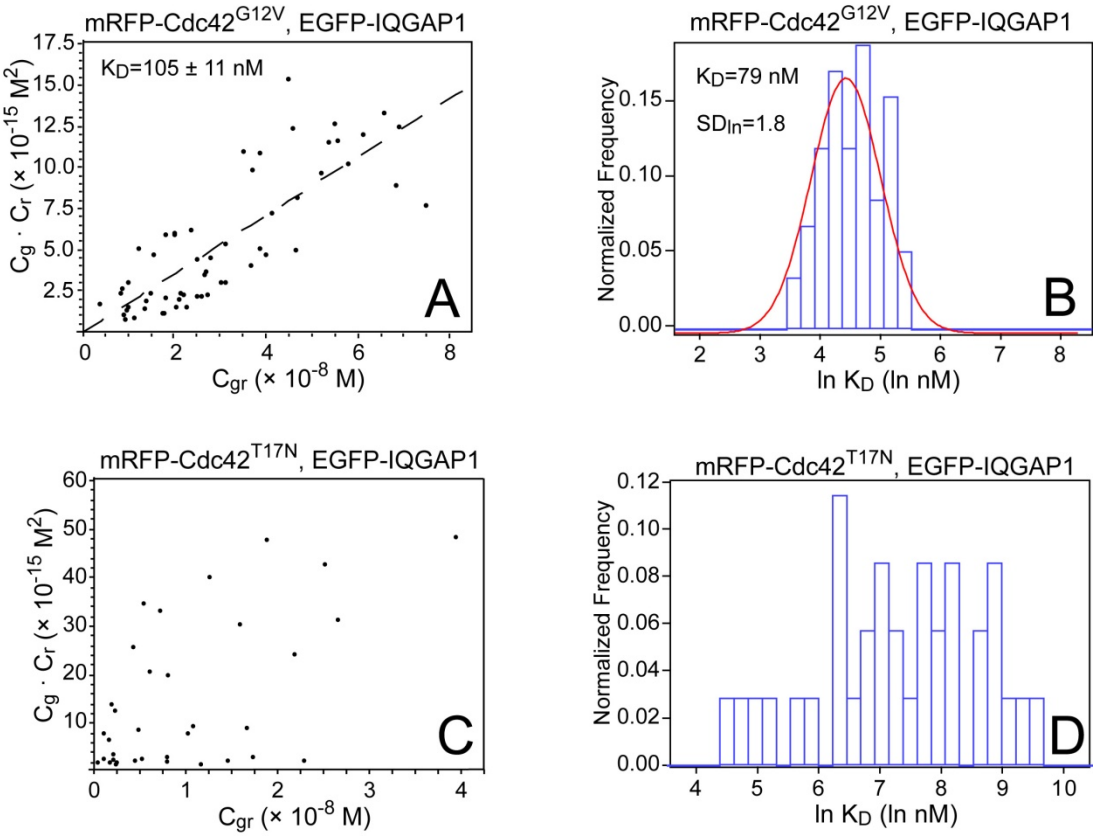

Fig. 5.7: Determination of K_D for the interacting protein pair of Cdc42 and IQGAP1. A). Determination of K_D for Cdc42^{G12V} and IQGAP1 using scattering plot. K_D value obtain by this method is 105 ± 11 nM. B) Determination of K_D for Cdc42^{G12V} and IQGAP1 using log normal distribution histogram. K_D value obtain by this method is 79 nM. C) and D) Determination of K_D for Cdc42^{T17N} and IQGAP1 using scattering plot and log normal distribution histogram, respectively. Data suggest no correlation but force fitted with K_D value ~ 1500 nM.

5.4.4 Comparison of Results from Zebrafish Embryo and CHO cells

The above mentioned measurements were also performed in CHO cells as comparison (Fig. 5.8, the CHO cell measurements were performed by colleague Foo Yong Hwee). The negative control, positive control, and the dominant-negative measurements all gave comparable results as in zebrafish embryo measurements (Table 5.2). However, the K_D value of 1000 nM for the interaction of IQGAP1 and $Cdc42^{G12V}$ was much higher in CHO cells and the portion of molecules forming a complex was considerably lower (12.2 ± 6.8 %), suggesting that even the constitutively active $Cdc42^{G12V}$ interacts weakly with IQGAP1 in CHO cells. The faster diffusion of the protein complex in CHO cells compared to that in embryos also implies that other effectors could be involved in these interactions in embryos but not in CHO cells. One possible explanation is the Ca^{2+} concentration dependent interactions of IQGAP1 with Cdc42 and other effectors such as F-actin. The intracellular cytosolic Ca^{2+} concentration is usually maintained at low level of approximately 0.1 μM (higher Ca^{2+} concentration can be found in intracellular organelles such as endoplasmic reticulum and midtochondria), some four orders of magnitude lower than the extracellular concentration (Ashley et al, 1991). In response to a stimulus, Ca^{2+} influx through Ca^{2+} channels rapidly increases the intracellular concentration some 10 to 100 fold. Such a transient increase is a ubiquitous signal transduction mechanism producing, for example, muscle contraction. In the zebrafish measurements, the embryos were anesthetized to prevent body movement, thus no muscle contraction was present and intracellular

Ca^{2+} concentration in the muscle fiber cells is believed to be maintained at low level. In comparison, the CHO cells were cultured in F-12K Kaighn's modification medium (Invitrogen, Singapore) which includes 1 mM calcium chloride and other calcium containing chemicals, and the intracellular concentration could be higher than that in embryo muscle fiber cells. As discussed in section **5.4.1**, several reports have shown that increased intracellular Ca^{2+} concentration will lead to binding of calmodulin to IQGAP1, which in turn promotes the dissociation of IQGAP1 from both Cdc42 and F-actin (Ho et al, 1999; Mateer et al, 2002). This might explain the weak interaction between $Cdc42^{G12V}$ and IQGAP1 in CHO cells and the faster diffusion of the protein complex. However, this idea needs to be verified experimentally.

It should be noted that SW-FCCS measurements in zebrafish embryos were performed 10 to 50 μm deep into the body tissue. Compared to CHO cells measurements, the deeper penetration results in an enlarged effective volume V_{eff}. Consequently, the EGFP, mRFP, and mRFP-EGFP measurements in embryo all possess longer diffusion times than in CHO cell (Table 1). The enlarged V_{eff} will result in an overestimation of concentrations of all particles. This will change the measured apparent K_D values by the same factor as the V_{eff} (Eq. 11), but will not affect the complex percentage values (Eq. 10). In addition, the distortion of the effective volume is also wavelength-dependent, and the enlargement of V_{eff} in the red channel could be slightly higher than that in the green channel, which leads to a further overestimation of K_D in the embryo. Taking these factors into consideration, the calculated K_D value of ~100 nM is an upper limit and the actual affinity is

possibly stronger (i.e. the K_D value is possibly lower), and the difference between CHO cells and zebrafish embryos could be an underestimation in our measurements.

5.4.5 Summary

The quantification of biomolecular interactions, at present, is mostly performed *in vitro*. In the last years, it became apparent, though, that biomolecular interactions are strongly dependent on their environment, the conditions of molecular crowding (Raghunath et al, 2007), concentration of reactants (Wylie et al, 2007a) and the 3D organization of cells in which measurements are taken. The quantitative determination of interactions is important in many fields of life sciences. It has implications for drug discovery as the direct study of interactions of potential drug molecules with their targets in a relevant environment, e.g. a living organisms, could lead to better prediction of drug efficacy and shorten the drug development process. In addition, in system biology there is a need for a better understanding of biological interactions under physiological conditions and to obtain physiologically relevant data for the simulation of biological networks. It therefore became increasingly important to quantify biological parameters, in particular biological interactions, in their natural environment within multi-cellular organisms. Here we demonstrate for the first time the measurement of dissociation constants of interacting proteins in living zebrafish embryos, using SW-FCCS. Furthermore, a substantial difference was detected between the level of these interactions in CHO

cells and muscle fiber cells within the embryos, which could be due to different intracellular Ca^{2+} concentrations. In the future we expect that new labeling strategies, and better fluorescent proteins with larger Stokes shifts, reduced dark states, and higher photostability will improve the technique considerably by providing a wider dynamic range for the measurements of interactions by SW-FCCS.

Table 5.2: Data obtained from muscle fiber cells in embryo and CHO cell

sample	Muscle fiber cell in embryo			CHO cell		
	$_D$ ± SD [ms]	complex ± SD [%]	sample size*	$_D$ ± SD [ms]	complex ± SD [%]	sample size
EGFP mRFP	G: 0.72 ± 0.21 R: 0.99 ± 0.24	6.2 ± 4.8	34	G: 0.50 ± 0.11 R: 0.65 ± 0.25	3.5 ± 2.8	29
mRFP-EGFP	G: 0.96 ± 0.15 R: 1.11 ± 0.21	44.9 ± 5.9	58	G: 0.64 ± 0.07 R: 0.75 ± 0.13	45.4 ± 4.8	28
EGFP-IQGAP1 mRFP-Cdc42^{G12V}	G: 7.0 ± 3.1 R: 10.2 ± 5.4	41.6 ± 9.2	62	G: 2.3 ± 0.8 R: 2.6 ± 0.8	12.2 ± 6.8	75
EGFP-IQGAP1 mRFP-Cdc42^{T17N}	G: 7.4 ± 2.9 R: 21.1 ± 8.0	12.6 ± 12.3	35†	G: 3.44 ± 1.76 R: 17.07 ± 9.69	8.7 ± 4.7	81

*each number represents a single measurement from one muscle fiber cell and generally 3 to 5 fibers were chosen from one embryo.

†number of measurements that exhibit some degree of cross-correlation. The corresponding complex percentage value is the average of these 35 measurements while another 78 measurements show no cross-correlation.

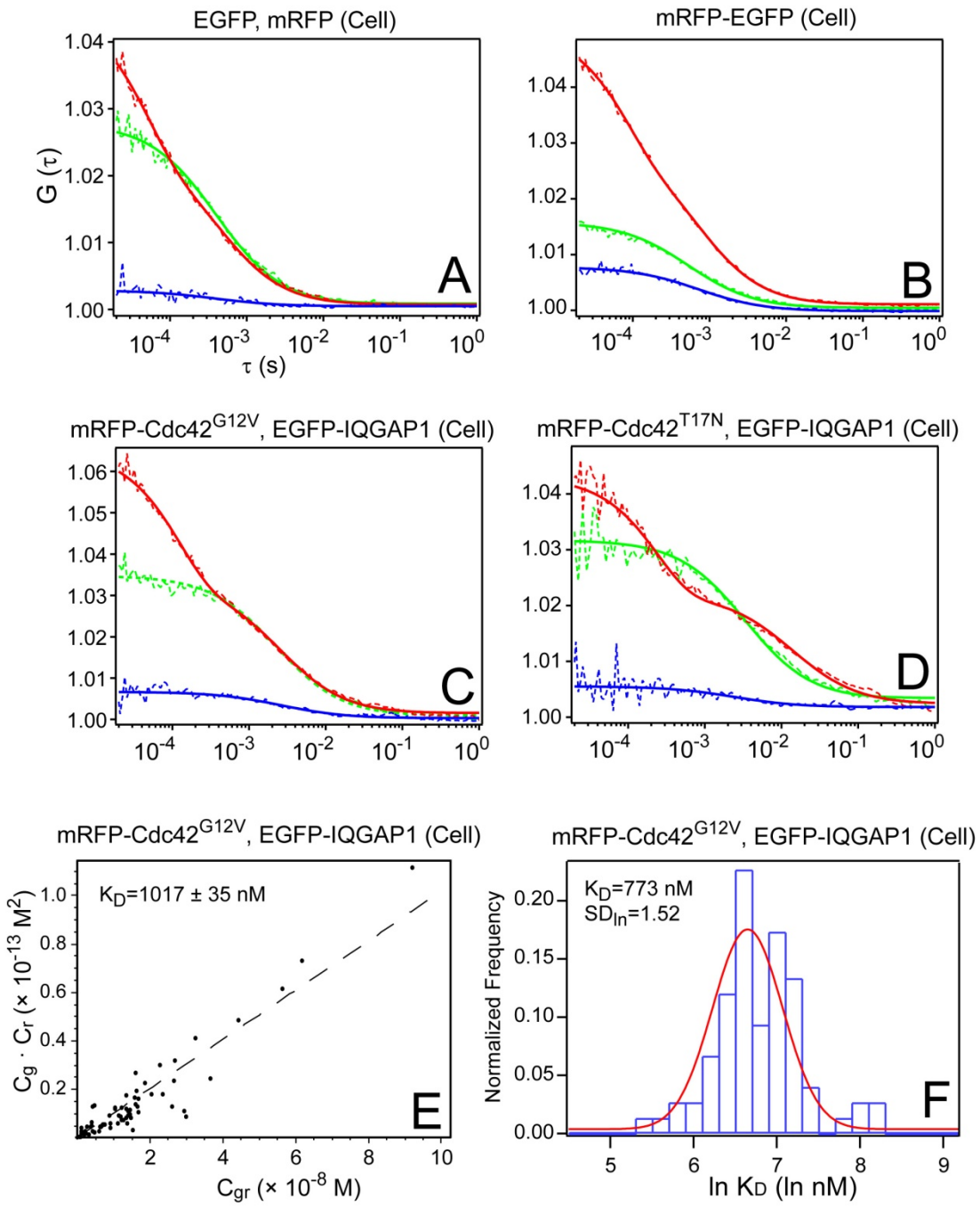

Fig. 5.8: SW-FCCS results obtained in CHO cell culture. A) SW-FCCS result of negative control of individually expressed EGFP and mRFP, showing both experimental curves (dashed line) and fitting curves (solid line). B) to D) SW-FCCS results of positive control (tandem mRFP-EGFP construct), $Cdc42^{G12V}$ with IQGAP1, and $Cdc42^{T17N}$ with IQGAP1, respectively. E) Determination of K_D for $Cdc42^{G12V}$ and IQGAP1 using scattering plot. K_D value obtained from this method is 1017 ± 35 nM. F) Determination of K_D for $Cdc42^{G12V}$ and IQGAP1 using log normal distribution histogram. K_D value obtained from this method is 773 nM.

Chapter 6

Conclusion and Outlook

6.1 Conclusion

The objective of this work was to quantify protein dynamics and interactions in a multicellular living organism. For this purpose, we extended existing biophysical methods, FCS and SW-FCCS, into living zebrafish embryos.

Recently, fluorescence-based biophysical techniques, i.e. FRAP, FRET, FLIM and FCS, have been established as routine tools to probe biomolecule dynamics and interactions in Petri dish-based cell cultures. However, how authentic those *in vitro* findings reflect *in vivo* biological processes is unclear, and more and more publications were proving otherwise. It is therefore desirable to be able to directly study biomolecules in an *in vivo* system. In this work, zebrafish was chosen as a model organism for this purpose, as the transparent tissue aids fluorescence-based applications. Less light blockage at the visible light range from 380 to 750 nm enables FCS/SW-FCCS studies of cells deep beneath skin.

We examined how and to what extend FCS measurements can be realized in zebrafish embryos. In order to label the protein-of-interest with a fluorescent tag, we attached the EGFP DNA to the zebrafish genes and microinjected the constructs

into one blastomere at 16 cell stage zebrafish embryos. The mosaic expression of injected DNA provided cells with different protein expression level to choose from and cells with low fluorescence level were chosen for subsequent FCS/SW-FCCS measurements. We then examined the autofluorescence expression of zebrafish embryo, the distribution of autofluorescence in the embryo body and the autofluorescence emission spectrum, aiming to minimize the background interference. We chose the less-autofluorescent trunk region to perform FCS/SW-FCCS measurements and proved that our filter set can efficiently block most autofluorescence intensity. In addition, we observed that autofluorescence from zebrafish embryo (excludes blood vessel fluid and skin) didn't generate autocorrelations and it served only as a steady background. The autofluorescence therefore led to an overestimation of the concentration of the target molecule but didn't affect the temporal information, and the contribution of autofluorescence to the overall fluorescence intensity is less than 10%. At last, we studied the working distance of FCS in zebrafish tissue. Using OPE, we showed that FCS can efficiently determine diffusion coefficients of cytoplasmic EGFP in cells at least 50 µm, and possibly up to 80 µm deep within tissue. By adjusting the orientation of the embryo, 80 µm of working distance covers most of the tissues and organs within the embryo. We further demonstrated that the working distance of FCS can be improved by using optimized TPE and suitable TPE dyes. By injecting TMR into the blood circulation, we showed that blood flow velocities can be accurately determined up to 200 µm within tissue. Nevertheless, TPE didn't improve the working distance when EGFP was used as the fluorophore, mainly due to the poor fluorescent property of EGFP as a TPE dye.

The applicability of FCS to study molecular processes in zebrafish embryos was shown by the determination of blood flow velocities with high spatial resolution and the determination of diffusion coefficients of cytosolic and membrane-bound EGFP labeled proteins in different cell types. We first showed that using autofluorescence from blood serum, systolic and diastolic blood flow velocities can be accurately determined with spatial resolution of 0.5 μm. FCS can therefore be used as a true noninvasive method to measure blood flow in small vessels during embryogenesis even in absence of red blood cells. We next measured and compared the diffusion coefficients of EGFP and EGFP labeled proteins in various conditions in living zebrafish embryos. We found that (1) EGFP diffuses slightly faster in nucleoplasm than in cytoplasm in motor neuron cells; (2) Cytoplasm of muscle fiber cells have higher viscosity than that of motor neuron cells; (3) knockdown of Cxcr4b can alter the property of cytoplasm of motor neuron cells and small proteins diffuse less efficiently within it; and (4) Cxcr4b distributes evenly on the membrane of muscle fiber cells and the diffusion coefficient is roughly 0.6 $\mu m^2 s^{-1}$.

At last, we showed that protein-protein interaction can be directly quantified in living zebrafish embryos using SW-FCCS, a method developed in our lab. SW-FCCS requires dual-color labeling of interacting proteins and excitation of both fluorophores by a single wavelength. We have previously shown that by using EGFP and mRFP as fluorophores and exciting both at 514 nm, protein-protein interaction can be quantified in CHO cells. In this research, we first calibrated our instrument with R6G and showed that a complex percentage of ~ 100% can be obtained. We then performed FCS measurements in positive and negative controls. We

microinjected the EGFP-mRFP tandem construct as a positive control, and the measurements yielded a complex percentage of ~ 45%. This value was not ideally 100% mainly because of non-fluorescent FPs and photobleaching of FPs. In comparison, the negative control of individually expressed EGFP and mRFP gave complex percentage of ~ 6%, which was caused by the autofluorescence background induced false-positive cross-correlation amplitudes. The values of 45% and 6% therefore set the upper and lower limits of the SW-FCCS measurements in this case. We then studied the interaction between Cdc42, a small GTPase that belongs to the Rho/Rac subfamily, and IQGAP1, a multidomain scaffolding protein. The interaction between Cdc42 and IQGAP1 plays an important role in modeling microtubule and cytoskeleton during cell polarization and migration. We used two mutants of Cdc42 in this work: $Cdc42^{T17N}$, a GDP-bound dominant-negative mutant, and $Cdc42^{G12V}$, a constitutively active mutant which is in a predominantly GTP-bound form. While the measurements of EGFP-IQGAP1 and mRFP-$Cdc42^{G12V}$ yielded a complex percentage of 41.6 ± 9.2 % and a dissociation constant K_D of ~ 100 nM, the measurements of EGFP-IQGAP1 and mRFP-$Cdc42^{T17N}$ showed that only ~30% of the results generated positive CCF and the subpopulation gave a complex percentage of 12.6 ± 12.3 % and a dissociation constant K_D of ~ 1500 nM, confirming the active and inactive functions of the two mutants. In comparison, we measured the same protein-protein interactions in CHO cells cultures but observed significant differences in protein mobility and K_D from the zebrafish measurements. The measurements of EGFP-IQGAP1 and mRFP-$Cdc42^{G12V}$ yielded a complex percentage of only 12.2 ± 6.8 % and a dissociation constant K_D of ~ 1000 nM, suggesting that even constitutively active mutants interact weakly with its partner in CHO cells. The

faster diffusion of the protein complex in CHO cells compared to that in embryos also implies that other effectors could be involved in these interactions in embryos but not in CHO cells. This result supports the notion that bimolecular interactions depend on the biological system under investigation and are best performed under physiologically relevant conditions.

In summary, this research, for the first time to our knowledge, experimentally explored the viability of direct quantification of protein dynamics and interactions in living zebrafish embryos. This work provides cell and molecular biologists a more physiologically relevant platform to study biological processes, and at the same time provides developmental biologists a new tool to study biomolecules *in vivo*. Recently, we have already seen several more publications using fluorescence based single molecule techniques to answer developmental biology quenstions, in particular, combining total internal reflection (TIR) microscopy and single particle tracking (SPT), Schaaf et al. measured the diffusion properties of membrane proteins in epidermal cells in the skin of 2 dpf zebrafish embryos and revealed the different membrane microdomain organizations of cells in living embryos from that observed in cultured cells (Schaaf et al, 2009). Using FCS in living zebrafish embryos, Yu et al. successfully examined the formation of morphogen Fgf8 gradient in early tissue with high precision (Yu et al, 2009). In addition, the binding affinity between Fgf8 and its receptor was also quantitatively measured in early stage zebrafish embryos by dual-color scanning FCS as reported by Ries et al. (Ries et al, 2009). In the future, we expect to see more application of cell-biological based methods, in particular F-techniques, in embryo-based living organisms.

6.2 Outlook

The application of FCS in living zebrafish embryos can be further improved in two directions: to improve sensitivity, and to extend applicability. Firstly, the signal-to-noise ratio of FCS, especially SW-FCCS, relies heavily on the molecular brightness and photostability of the fluorophores. In this regard, new FPs with high quantum yields, improved photostability and large Stokes shift, or new protein labeling techniques coupled with more photostable organic dyes can be used to improve the sensitivity of FCS in general. Secondly, the application of FCS in this work was limited to embryos with microinjected foreign DNAs, protein interaction involving two partners, and measurements of single point at a time. New methodology and instrumentation will enable FCS/SW-FCCS to study embryos with endogenously fluorescent-labeled proteins in transgenic animals, protein interactions involving three or more protein partners, and simultaneous multi-points measurements.

The discovery and development of fluorescence proteins (Chalfie et al, 1994; Ormo et al, 1996; Shimomura et al, 1962) opened up the possibility of direct visualization of biomolecule activities in living cells, and since then FPs have been extensively used as biomarkers in life sciences. However, compared to conventional organic dyes, FPs have in general a lower molecular brightness. Using FCS, we have shown that measurements of EGFP yield a *cps* of ~ 6 kHz, and using SW-FCCS, this value is only ~ 1 kHz due to inefficient excitation and photon collection. In comparison, measurements of organic dye such as atto488 (www.atto-tec.com) generates *cps* of

>200 kHz under the same measurement condition. The use of EGFP and mRFP as fluorophores in this work limited the sensitivity of FCS/SW-FCCS measurements in living cells. Nevertheless, the efficiency of coupling, the controlled labeling ratio, and the specificity of the labeling process outweigh the disadvantage of the less optimal fluorescent properties of FPs. In recent years, a range of improved FPs have been reported (Matz et al, 1999; Xia et al, 2002) with reduced dark states, higher photostability, and improved PH stability (see table 6.1). The signal-to-noise ratio of intracellular FCS/SW-FCCS measurement is therefore bound to improve following these developments. For example, the complex percentage of the positive control of tandem EGFP-mRFP in our SW-FCCS measurements is ~ 45%. By replacing the mRFP with mCherry, which exhibits similar emission spectrum but improved photostability (Shaner et al, 2004), the complex percentage increases slightly to ~48% (unpublished data). In addition, new protein labeling techniques, e.g. SNAP-tag (Keppler et al, 2003), nowadays allow specific attachment of virtually any molecule to a protein of interest. The SNAP-tag can be genetically encoded to a target protein and it specifically forms a covalent thioether bond with its substrates. By synthesizing fluorescent dye molecule to the SNAP-tag substrate, protein labeling with optimal organic dyes can be achieved and the sensitivity can be further improved.

On the other hand, the signal-to-noise ratio of SW-FCCS relies not only on the molecular brightness and photostability of the fluorophore, but also on its fluorescence spectra. The realization of dual color single wavelength excitation requires FP pairs with similar excitation spectra but distinct emission spectra. The FP pairs of EGFP and mRFP, as well as EGFP and mCherry merely fulfill this

requirement (Fig. 2.3). Therefore, the development of FPs and organic dyes with large Stokes shift will be ideal for SW-FCCS applications. Newly developed far red FPs, e.g. TagFP635 (Shcherbo et al, 2007), FPs with large Stokes shifts, e.g. mKeima (Kogure et al, 2006) and Megastokes organic dyes coupled with SNAP-tag technique, e.g. DY-480XL (www.dyomics.com), could be used to improve the excitation and detection efficiencies of SW-FCCS measurements. As examples, we show the spectra of FP pair of EGFP and TagFP635, and fluorophore pair of EGFP and DY-480XL in Fig. 6.1. Taking together the improved molecular brightnesses and photostabilities (Table 6.1), these new flurophores could provide a wider dynamic range for the measurements of interactions by SW-FCCS.

Table 6.1: fluorescent properties of some fluorophores

fluorophore	Excitation (nm)	Emission (nm)	Extinction coefficient ($M^{-1}cm^{-1}$)	Quantum yield
EGFP	489	509	55,000	0.60
mRFP	584	607	44,000	0.25
mcherry	587	615	72,000	0.22
TagFP635	588	635	45,000	0.33
DY-480XL	500	630	50,000	unknown
mKeima	440	620	14,400	0.24

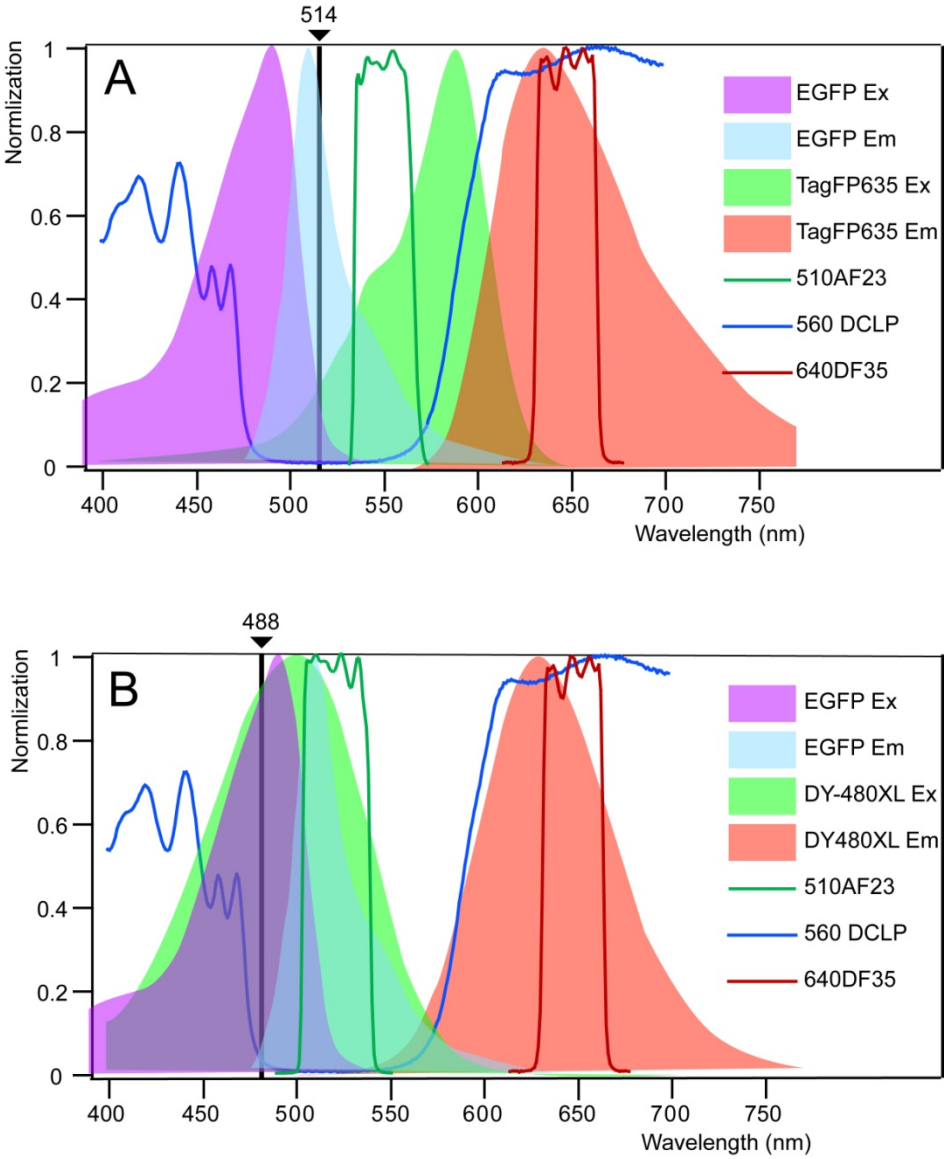

Fig. 6.1: Excitation and emission spectra of two fluorophore pairs. A) Excitation and emission spectra of EGFP and TagFP635. It is feasible to excite both at 514 nm and separately collect fluorescence signal at 545 nm and 640 nm. The dashed lines are the excitation spectra and the solid lines are emission spectra. B) Excitation and emission spectra of EGFP and DY-480XL. It is feasible to excite both at 488 nm and separately collect fluorescence signal at 510 nm and 640 nm.

The applicability of FCS/SW-FCCS in embryos can be extended with new zebrafish transgenic lines and new FCS modalities. Firstly, DNA microinjection was used in this work to introduce fluorescence labels in zebrafish embryos. One drawback of this

method is the difficulty in controlling the exact gene expression levels. It has been shown that the concentration of a biomolecule is critical in determining its functions in living cells (Wylie et al, 2007b). Hence a zebrafish transgenic line that expresses endogenously fluorescent-labeled proteins at physiological level would be advantageous. This could greatly reduce the workload of microinjection and cell selection, and at the same time provides more physiologically relevant data. Two-color transgenic zebrafish can also be generated by crossing single color lines and the embryos can be used for protein-protein interaction measurements. In this work of SW-FCCS measurements, unlabeled endogenous protein may also compete in the interactions between FP-fusion proteins and affect the dissociation constant value. The above mentioned transgenic lines can thereby eliminate this concern. Secondly, a dual-color SW-FCCS was demonstrated in this work but protein interactions often involve more than two components. It is therefore necessary to develop multi-color SW-FCCS in cells and embryos. To detect higher order molecular interactions *in vitro,* multi-color SW-FCCS has been demonstrated by Hwang (Hwang et al, 2006a; Hwang et al, 2006b). Considering the fast development of FPs and labeling strategies, it is reasonable to expect *in vivo* multi-color SW-FCCS applications in the near future. Thirdly, the confocal setup in this work restricted measurements to single point at a time and the data was characterized with limited spatial information. It is therefore difficult, for example, to map protein activities in different subcellular compartments, or study protein active transport within a whole cell. In recent years, the development of electron multiplying charge-coupled device (EMCCD)-based FCS, which provides an array of detectors, has reached a stage where protein diffusion can be simultaneously measured in an

entire cell membrane (Kannan et al, 2007; Sisan et al, 2006). EMCCD cameras were characterized with single-photon sensitivity, over 90% quantum efficiency and read-out speeds in the microsecond to millisecond range, features that are suitable for FCS applications (Burkhardt & Schwille, 2006; Kannan et al, 2006). Taken together with a high speed excitation scheme, e.g. spinning disk confocal microscopy (Sisan et al, 2006) or scanned light sheet microscopy (Keller et al, 2008), FCS imaging could be realized in living zebrafish embryo which facilitates the combination of spatial and temporal correlations that tremendously increase the information accessible from a single experiment. At last, FCS is and will be more often used in combination with other complementary spectroscopic techniques, e.g. photon counting histogram (PCH, Chen et al, 1999) and FRET (Sudhaharan et al, 2009), to create customized systems for the solution of particular problems. This could also benefit the embryo-based studies.

References:

Alberts B, Bray D, Lewis J, Raff M, Roberts K, Watson JD (2002) *Molecular biology of the cell*, 4 edn.: Garland.

Anders M, Hansen R, Ding RX, Rauen KA, Bissell MJ, Korn WM 2003. Disruption of 3D tissue integrity facilitates adenovirus infection by deregulating the coxsackievirus and adenovirus receptor. *Proceedings of the National Academy of Sciences of the United States of America* 100(4)**:** 1943-1948

Andersson H, Baechi T, Hoechl M, Richter C 1998. Autofluorescence of living cells. *Journal of microscopy* 191(Pt 1)**:** 1-7

Antonny B, Schekman R 2001. ER export: public transportation by the COPII coach. *Curr Opin Cell Biol* 13(4)**:** 438-443

Ashley CC, Mulligan IP, Lea TJ 1991. Ca2+ and activation mechanisms in skeletal muscle. *Q Rev Biophys* 24(1)**:** 1-73

Axelrod D, Koppel DE, Schlessinger J, Elson E, Webb WW 1976. Mobility measurement by analysis of fluorescence photobleaching recovery kinetics. *Biophysical journal* 16(9)**:** 1055-1069

Babcock GJ, Farzan M, Sodroski J 2003. Ligand-independent dimerization of CXCR4, a principal HIV-1 coreceptor. *The Journal of biological chemistry* 278(5)**:** 3378-3385

Bacia K, Kim SA, Schwille P 2006. Fluorescence cross-correlation spectroscopy in living cells. *Nature methods* 3(2)**:** 83-89

Bacia K, Majoul IV, Schwille P 2002. Probing the endocytic pathway in live cells using dual-color fluorescence cross-correlation analysis. *Biophysical journal* 83(2)**:** 1184-1193

Bacia K, Schwille P 2007. Practical guidelines for dual-color fluorescence cross-correlation spectroscopy. *Nature protocols* 2(11)**:** 2842-2856

Banks DS, Fradin C 2005. Anomalous diffusion of proteins due to molecular crowding. *Biophysical journal* 89(5)**:** 2960-2971

Barak LS, Ferguson SS, Zhang J, Martenson C, Meyer T, Caron MG 1997. Internal trafficking and surface mobility of a functionally intact beta2-adrenergic receptor-green fluorescent protein conjugate. *Molecular pharmacology* 51(2)**:** 177-184

Baudendistel N, Muller G, Waldeck W, Angel P, Langowski J 2005. Two-hybrid fluorescence cross-correlation spectroscopy detects protein-protein interactions in vivo. *Chemphyschem* 6(5)**:** 984-990

Beil M, Micoulet A, von Wichert G, Paschke S, Walther P, Omary MB, Van Veldhoven PP, Gern U, Wolff-Hieber E, Eggermann J, Waltenberger J, Adler G, Spatz J, Seufferlein T 2003. Sphingosylphosphorylcholine regulates keratin network

architecture and visco-elastic properties of human cancer cells. *Nat Cell Biol* 5(9)**:** 803-811

Beis D, Stainier DY 2006. In vivo cell biology: following the zebrafish trend. *Trends in cell biology* 16(2)**:** 105-112

Bensenor LB, Kan HM, Wang N, Wallrabe H, Davidson LA, Cai Y, Schafer DA, Bloom GS 2007. IQGAP1 regulates cell motility by linking growth factor signaling to actin assembly. *J Cell Sci* 120(Pt 4)**:** 658-669

Berghmans S, Jette C, Langenau D, Hsu K, Stewart R, Look T, Kanki JP 2005. Making waves in cancer research: new models in the zebrafish. *BioTechniques* 39(2)**:** 227-237

Berland K, Shen G 2003. Excitation saturation in two-photon fluorescence correlation spectroscopy. *Applied optics* 42(27)**:** 5566-5576

Berne BJ, Pecora R (2000) *Dynamic Light Scattering: With Applications to Chemistry, Biology, and Physics*: Courier Dover Publications.

Berry H 2002. Monte carlo simulations of enzyme reactions in two dimensions: fractal kinetics and spatial segregation. *Biophysical journal* 83(4)**:** 1891-1901

Bevington P, Robinson D (1992) *Data Reduction and Error Analysis for the Physical Sciences (2d ed.; New York*: McGraw-Hill.

Bolin F, Preuss L, Taylor R, Ference R 1989. Refractive index of some mammalian tissues using a fiber optic cladding method. *Applied Optics* 28(12)**:** 2297-2303

Brandt DT, Grosse R 2007. Get to grips: steering local actin dynamics with IQGAPs. *EMBO reports* 8(11)**:** 1019-1023

Briggs MW, Li Z, Sacks DB 2002. IQGAP1-mediated stimulation of transcriptional co-activation by beta-catenin is modulated by calmodulin. *The Journal of biological chemistry* 277(9)**:** 7453-7465

Briggs MW, Sacks DB 2003a. IQGAP1 as signal integrator: Ca2+, calmodulin, Cdc42 and the cytoskeleton. *FEBS letters* 542(1-3)**:** 7-11

Briggs MW, Sacks DB 2003b. IQGAP proteins are integral components of cytoskeletal regulation. *EMBO reports* 4(6)**:** 571-574

Brock R, Hink MA, Jovin TM 1998. Fluorescence correlation microscopy of cells in the presence of autofluorescence. *Biophysical journal* 75(5)**:** 2547-2557

Brock R, Jovin TM 1998. Fluorescence correlation microscopy (FCM)-fluorescence correlation spectroscopy (FCS) taken into the cell. *Cellular and molecular biology (Noisy-le-Grand, France)* 44(5)**:** 847-856

Burkhardt M, Schwille P 2006. Electron multiplying CCD based detection for spatially resolved fluorescence correlation spectroscopy. *Optics Express* 14(12)**:** 5013-5020

Camacho A, Korn K, Damond M, Cajot JF, Litborn E, Liao B, Thyberg P, Winter H, Honegger A, Gardellin P, Rigler R 2004. Direct quantification of mRNA expression levels using single molecule detection. *Journal of biotechnology* 107(2)**:** 107-114

Campbell RE, Tour O, Palmer AE, Steinbach PA, Baird GS, Zacharias DA, Tsien RY 2002a. A monomeric red fluorescent protein. *Proceedings of the National Academy of Sciences of the United States of America* 99(12)**:** 7877-7882

Campbell RE, Tour O, Palmer AE, Steinbach PA, Baird GS, Zacharias DA, Tsien RY 2002b. A monomeric red fluorescent protein. *Proc Natl Acad Sci USA* 99(12)**:** 7877-7882

Cerione RA 2004. Cdc42: new roads to travel. *Trends Cell Biol* 14(3)**:** 127-132

Chakrabarti S, Streisinger G, Singer F, Walker C 1983. Frequency of gamma-Ray Induced Specific Locus and Recessive Lethal Mutations in Mature Germ Cells of the Zebrafish, BRACHYDANIO RERIO. *Genetics* 103(1)**:** 109-123

Chalfie M, Tu Y, Euskirchen G, Ward WW, Prasher DC 1994. Green fluorescent protein as a marker for gene expression. *Science* 263(5148)**:** 802-805

Chen Y, Muller JD, So PT, Gratton E 1999. The photon counting histogram in fluorescence fluctuation spectroscopy. *Biophysical journal* 77(1)**:** 553-567

Cheng H, Luo Q, Zeng S, Chen S, Cen J, Gong H 2003. Modified laser speckle imaging method with improved spatial resolution. *J Biomed Opt* 8(3)**:** 559-564

Cheong WF, Prahl SA, Welch AJ 1990. A review of the optical properties of biological tissues. *IEEE J Quantum Electron* 26(12)**:** 2166-2185

Chien S, Usami S, Skalak R (1977) Blood flow in small tubes. In *Handbook of physiology: A Critical, Comprehensive Presentation of Physiological Knowledge and Concepts*, Geiger SR (ed), Vol. 1000, p 217. Bethesda: American Physiological Society

Chong SW, Emelyanov A, Gong Z, Korzh V 2001. Expression pattern of two zebrafish genes, cxcr4a and cxcr4b. *Mechanisms of development* 109(2)**:** 347-354

Chong SW, Korzh V, Jiang YJ 2009. Myogenesis and Molecules - insight from zebrafish. *J Fish Biol* (in press)

Chong SW, Nguyet LM, Jiang YJ, Korzh V 2007. The chemokine Sdf-1 and its receptor Cxcr4 are required for formation of muscle in zebrafish. *BMC Dev Biol* 7**:** 54

Coso OA, Chiariello M, Yu JC, Teramoto H, Crespo P, Xu N, Miki T, Gutkind JS 1995. The small GTP-binding proteins Rac1 and Cdc42 regulate the activity of the JNK/SAPK signaling pathway. *Cell* 81(7)**:** 1137-1146

Darling EM, Zauscher S, Block JA, Guilak F 2007. A thin-layer model for viscoelastic, stress-relaxation testing of cells using atomic force microscopy: do cell properties reflect metastatic potential? *Biophysical journal* 92(5)**:** 1784-1791

Dauty E, Verkman AS 2005. Actin cytoskeleton as the principal determinant of size-dependent DNA mobility in cytoplasm: a new barrier for non-viral gene delivery. *The Journal of biological chemistry* 280(9)**:** 7823-7828

Denk W, Strickler JH, Webb WW 1990. Two-photon laser scanning fluorescence microscopy. *Science* 248(4951)**:** 73-76

Dittrich P, Malvezzi-Campeggi F, Jahnz M, Schwille P 2001. Accessing molecular dynamics in cells by fluorescence correlation spectroscopy. *Biological chemistry* 382(3)**:** 491-494

Dittrich PS, Schwille P 2001. Photobleaching and stabilization of. fluorophores used for single-molecule analysis. with one-and two-photon excitation. *Appl Phys B* 73(8)**:** 829-837

Doitsidou M, Reichman-Fried M, Stebler J, Koprunner M, Dorries J, Meyer D, Esguerra CV, Leung T, Raz E 2002. Guidance of primordial germ cell migration by the chemokine SDF-1. *Cell* 111(5)**:** 647-659

Dross N, Spriet C, Zwerger M, Muller G, Waldeck W, Langowski J 2009. Mapping eGFP oligomer mobility in living cell nuclei. *PLoS ONE* 4(4)**:** e5041

Eggeling C, Ringemann C, Medda R, Schwarzmann G, Sandhoff K, Polyakova S, Belov VN, Hein B, von Middendorff C, Schonle A, Hell SW 2009. Direct observation of the nanoscale dynamics of membrane lipids in a living cell. *Nature* 457(7233)**:** 1159-1162

Eigen M, Rigler R 1994. Sorting Single Molecules: Application to Diagnostics and Evolutionary Biotechnology. *Proceedings of the National Academy of Sciences of the United States of America* 91(13)**:** 5740-5747

Eisen JS 1996. Zebrafish make a big splash. *Cell* 87(6)**:** 969-977

Elson EL, Magde D 1974. Fluorescence correlation spectroscopy. I. Conceptual basis and theory. *Biopolymers* 13(1)**:** 1-27

Enderlein J, Gregor I, Patra D, Dertinger T, Kaupp UB 2005. Performance of fluorescence correlation spectroscopy for measuring diffusion and concentration. *Chemphyschem* 6(11)**:** 2324-2336

Erickson JW, Cerione RA, Hart MJ 1997. Identification of an actin cytoskeletal complex that includes IQGAP and the Cdc42 GTPase. *The Journal of biological chemistry* 272(39)**:** 24443-24447

Farnsworth CL, Feig LA 1991. Dominant inhibitory mutations in the Mg(2+)-binding site of RasH prevent its activation by GTP. *Molecular and cellular biology* 11(10)**:** 4822-4829

Feder TJ, Brust-Mascher I, Slattery JP, Baird B, Webb WW 1996. Constrained diffusion or immobile fraction on cell surfaces: a new interpretation. *Biophysical journal* 70(6)**:** 2767-2773

Feig LA, Cooper GM 1988. Inhibition of NIH 3T3 cell proliferation by a mutant ras protein with preferential affinity for GDP. *Molecular and cellular biology* 8(8)**:** 3235-3243

Fetcho JR, Higashijima S, McLean DL 2008. Zebrafish and motor control over the last decade. *Brain Res Rev* 57(1)**:** 86-93

Foldes-Papp Z, Rigler R 2001. Quantitative two-color fluorescence cross-correlation spectroscopy in the analysis of polymerase chain reaction. *Biological chemistry* 382(3)**:** 473-478

Foquet M, Korlach J, Zipfel W, Webb WW, Craighead HG 2002. DNA fragment sizing by single molecule detection in submicrometer-sized closed fluidic channels. *Anal Chem* 74(6)**:** 1415-1422

Gilmour D, Knaut H, Maischein HM, Nusslein-Volhard C 2004. Towing of sensory axons by their migrating target cells in vivo. *Nat Neurosci* 7(5)**:** 491-492

Gosch M, Blom H, Holm J, Heino T, Rigler R 2000. Hydrodynamic flow profiling in microchannel structures by single molecule fluorescence correlation spectroscopy. *Anal Chem* 72(14)**:** 3260-3265

Guigas G, Kalla C, Weiss M 2007a. The degree of macromolecular crowding in the cytoplasm and nucleoplasm of mammalian cells is conserved. *FEBS letters* 581(26)**:** 5094-5098

Guigas G, Kalla C, Weiss M 2007b. Probing the nano-scale viscoelasticity of intracellular fluids in living cells. *Biophysical journal*

Guigas G, Weiss M 2007. Sampling the cell with anomalous diffusion - the discovery of slowness. *Biophysical journal*

Hart MJ, Callow MG, Souza B, Polakis P 1996. IQGAP1, a calmodulin-binding protein with a rasGAP-related domain, is a potential effector for cdc42Hs. *EMBO J* 15(12)**:** 2997-3005

Haupts U, Maiti S, Schwille P, Webb WW 1998. Dynamics of fluorescence fluctuations in green fluorescent protein observed by fluorescence correlation spectroscopy. *Proc Natl Acad Sci USA* 95(23)**:** 13573-13578

Haustein E, Schwille P 2007. Fluorescence correlation spectroscopy: novel variations of an established technique. *Annual review of biophysics and biomolecular structure* 36**:** 151-169

Heasman J 2002. Morpholino oligos: making sense of antisense? *Developmental biology* 243(2)**:** 209-214

Heasman SJ, Ridley AJ 2008. Mammalian Rho GTPases: new insights into their functions from in vivo studies. *Nat Rev Mol Cell Biol* 9(9)**:** 690-701

Hell S, Reiner G, Cremer C, Stelzer EHK 1993. Aberrations in Confocal Fluorescence Microscopy Induced by Mismatches in Refractive Index. *Journal of microscopy* 169(3)**:** 341-405

Helmchen F, Denk W 2005. Deep tissue two-photon microscopy. *Nature methods* 2(12)**:** 932-940

Henion PD, Raible DW, Beattie CE, Stoesser KL, Weston JA, Eisen JS 1996. Screen for mutations affecting development of Zebrafish neural crest. *Dev Genet* 18(1)**:** 11-17

Higashijima S, Hotta Y, Okamoto H 2000. Visualization of cranial motor neurons in live transgenic zebrafish expressing green fluorescent protein under the control of the islet-1 promoter/enhancer. *J Neurosci* 20(1)**:** 206-218

Hillesheim LN, Chen Y, Muller JD 2006. Dual-Color Photon Counting Histogram Analysis of mRFP1 and EGFP in Living Cells. *Biophysical journal* 91(11)**:** 4273-4284

Hirschfeld T 1976. Optical microscopic observation of single small molecules. *Applied optics* 15(12)**:** 2965-2966

Ho YD, Joyal JL, Li Z, Sacks DB 1999. IQGAP1 integrates Ca2+/calmodulin and Cdc42 signaling. *The Journal of biological chemistry* 274(1)**:** 464-470

Hollway GE, Bryson-Richardson RJ, Berger S, Cole NJ, Hall TE, Currie PD 2007. Whole-somite rotation generates muscle progenitor cell compartments in the developing zebrafish embryo. *Dev Cell* 12(2)**:** 207-219

Hove JR, Koster RW, Forouhar AS, Acevedo-Bolton G, Fraser SE, Gharib M 2003. Intracardiac fluid forces are an essential epigenetic factor for embryonic cardiogenesis. *Nature* 421(6919)**:** 172-177

Hwang LC, Gosch M, Lasser T, Wohland T 2006a. Simultaneous multicolor fluorescence cross-correlation spectroscopy to detect higher order molecular interactions using single wavelength laser excitation. *Biophysical journal* 91(2)**:** 715-727

Hwang LC, Leutenegger M, Gosch M, Lasser T, Rigler P, Meier W, Wohland T 2006b. Prism-based multicolor fluorescence correlation spectrometer. *Optics letters* 31(9)**:** 1310-1312

Hwang LC, Wohland T 2004. Dual-color fluorescence cross-correlation spectroscopy using single laser wavelength excitation. *Chemphyschem* 5(4)**:** 549-551

Hwang LC, Wohland T 2005. Single wavelength excitation fluorescence cross-correlation spectroscopy with spectrally similar fluorophores: resolution for binding studies. *The Journal of chemical physics* 122(11)**:** 114708

Hwang LC, Wohland T 2007. Recent advances in fluorescence cross-correlation spectroscopy. *Cell biochemistry and biophysics* 49(1)**:** 1-13

Joyal JL, Annan RS, Ho YD, Huddleston ME, Carr SA, Hart MJ, Sacks DB 1997. Calmodulin modulates the interaction between IQGAP1 and Cdc42. Identification of IQGAP1 by nanoelectrospray tandem mass spectrometry. *The Journal of biological chemistry* 272(24)**:** 15419-15425

Kannan B, Guo L, Sudhaharan T, Ahmed S, Maruyama I, Wohland T 2007. Spatially resolved total internal reflection fluorescence correlation microscopy using an electron multiplying charge-coupled device camera. *Analytical chemistry* 79(12)**:** 4463-4470

Kannan B, Har JY, Liu P, Maruyama I, Ding JL, Wohland T 2006. Electron multiplying charge-coupled device camera based fluorescence correlation spectroscopy. *Analytical chemistry* 78(10)**:** 3444-3451

Kask P, Gunther R, Axhausen P 1997. Statistical accuracy in fluorescence fluctuation experiments. *European Biophysics Journal* 25(3)**:** 163-169

Keller PJ, Schmidt AD, Wittbrodt J, Stelzer EH 2008. Reconstruction of zebrafish early embryonic development by scanned light sheet microscopy. *Science* 322(5904)**:** 1065-1069

Keppler A, Gendreizig S, Gronemeyer T, Pick H, Vogel H, Johnsson K 2003. A general method for the covalent labeling of fusion proteins with small molecules in vivo. *Nat Biotechnol* 21(1)**:** 86-89

Kettling U, Koltermann A, Schwille P, Eigen M 1998. Real-time enzyme kinetics monitored by dual-color fluorescence cross-correlation spectroscopy. *Proceedings of the National Academy of Sciences of the United States of America* 95(4)**:** 1416-1420

Kim SA, Heinze KG, Schwille P 2007. Fluorescence correlation spectroscopy in living cells. *Nature methods* 4(11)**:** 963-973

Kogure T, Karasawa S, Araki T, Saito K, Kinjo M, Miyawaki A 2006. A fluorescent variant of a protein from the stony coral Montipora facilitates dual-color single-laser fluorescence cross-correlation spectroscopy. *Nature biotechnology* 24(5)**:** 577-581

Kohl T, Haustein E, Schwille P 2005. Determining protease activity in vivo by fluorescence cross-correlation analysis. *Biophysical journal* 89(4)**:** 2770-2782

Kohler RH, Schwille P, Webb WW, Hanson MR 2000. Active protein transport through plastid tubules: velocity quantified by fluorescence correlation spectroscopy. *J Cell Sci* 113 (Pt 22)**:** 3921-3930

Kolin DL, Wiseman PW 2007. Advances in image correlation spectroscopy: measuring number densities, aggregation states, and dynamics of fluorescently labeled macromolecules in cells. *Cell biochemistry and biophysics* 49(3)**:** 141-164

Koppel D 1974. Statistical accuracy in fluorescence correlation spectroscopy. *Physical Review A* 10(6)**:** 1938-1945

Koppel DE, Morgan F, Cowan AE, Carson JH 1994. Scanning concentration correlation spectroscopy using the confocal laser microscope. *Biophysical journal* 66(2 Pt 1)**:** 502-507

Korn K, Gardellin P, Liao B, Amacker M, Bergstrom A, Bjorkman H, Camacho A, Dorhofer S, Dorre K, Enstrom J, Ericson T, Favez T, Gosch M, Honegger A, Jaccoud S, Lapczyna M, Litborn E, Thyberg P, Winter H, Rigler R 2003. Gene expression analysis using single molecule detection. *Nucleic acids research* 31(16)**:** e89

Korzh S, Pan X, Garcia-Lecea M, Winata CL, Wohland T, Korzh V, Gong Z 2008. Requirement of vasculogenesis and blood circulation in late stages of liver growth in zebrafish. *BMC Dev Biol* 8**:** 84

Korzh V 2007. Transposons as tools for enhancer trap screens in vertebrates. *Genome Biology* 8(Suppl 1)**:** S8

Kunst BH, Schots A, Visser AJ 2002. Detection of flowing fluorescent particles in a microcapillary using fluorescence correlation spectroscopy. *Anal Chem* 74(20)**:** 5350-5357

Kuroda S, Fukata M, Kobayashi K, Nakafuku M, Nomura N, Iwamatsu A, Kaibuchi K 1996. Identification of IQGAP as a putative target for the small GTPases, Cdc42 and Rac1. *The Journal of biological chemistry* 271(38)**:** 23363-23367

Kuroda S, Fukata M, Nakagawa M, Fujii K, Nakamura T, Ookubo T, Izawa I, Nagase T, Nomura N, Tani H, Shoji I, Matsuura Y, Yonehara S, Kaibuchi K 1998. Role of IQGAP1, a target of the small GTPases Cdc42 and Rac1, in regulation of E-cadherin- mediated cell-cell adhesion. *Science* 281(5378)**:** 832-835

Lamond AI, Earnshaw WC 1998. Structure and function in the nucleus. *Science* 280(5363)**:** 547-553

Le Clainche C, Schlaepfer D, Ferrari A, Klingauf M, Grohmanova K, Veligodskiy A, Didry D, Le D, Egile C, Carlier M 2007. IQGAP1 stimulates actin assembly through the N-WASP-Arp2/3 pathway. *Journal of Biological Chemistry* 282(1)**:** 426

Le Grand Y, Leray A, Guilbert T, Odin C 2008. Non-descanned versus descanned epifluorescence collection in two-photon microscopy: Experiments and Monte Carlo simulations. *Optics Communications* 281(21)**:** 5480-5486

Levoye A, Balabanian K, Baleux F, Bachelerie F, Lagane B 2009. CXCR7 heterodimerizes with CXCR4 and regulates CXCL12-mediated G protein signalling. *Blood*

Liang L, Wang X, Xing D, Chen T, Chen WR 2009. Noninvasive determination of cell nucleoplasmic viscosity by fluorescence correlation spectroscopy. *Journal of biomedical optics* 14(2)**:** 024013

Lieschke GJ, Currie PD 2007. Animal models of human disease: zebrafish swim into view. *Nature reviews* 8(5)**:** 353-367

Limpert E, Stahel WA, Abbt M 2001. Log-normal Distributions across the Sciences: Keys and Clues. *BioScience* 51(5)**:** 341-352

Lister JA, Robertson CP, Lepage T, Johnson SL, Raible DW 1999. nacre encodes a zebrafish microphthalmia-related protein that regulates neural-crest-derived pigment cell fate. *Development* 126(17)**:** 3757-3767

Liu P, Ahmed S, Wohland T 2008a. The F-techniques: advances in receptor protein studies. *Trends in endocrinology and metabolism: TEM*

Liu P, Ahmed S, Wohland T 2008b. The F-techniques: advances in receptor protein studies. *Trends in endocrinology and metabolism: TEM* 19(5)**:** 181-190

Liu P, Sudhaharan T, Koh RM, Hwang LC, Ahmed S, Maruyama IN, Wohland T 2007. Investigation of the dimerization of proteins from the epidermal growth factor receptor family by single wavelength fluorescence cross-correlation spectroscopy. *Biophysical journal* 93(2)**:** 684-698

Llopis J, McCaffery JM, Miyawaki A, Farquhar MG, Tsien RY 1998. Measurement of cytosolic, mitochondrial, and Golgi pH in single living cells with green fluorescent proteins. *Proceedings of the National Academy of Sciences of the United States of America* 95(12)**:** 6803-6808

Luby-Phelps K 1994. Physical properties of cytoplasm. *Curr Opin Cell Biol* 6(1)**:** 3-9

Lukacs GL, Haggie P, Seksek O, Lechardeur D, Freedman N, Verkman AS 2000. Size-dependent DNA mobility in cytoplasm and nucleus. *The Journal of biological chemistry* 275(3)**:** 1625-1629

Macias MJ, Wiesner S, Sudol M 2002. WW and SH3 domains, two different scaffolds to recognize proline-rich ligands. *FEBS letters* 513(1)**:** 30-37

Maeder CI, Hink MA, Kinkhabwala A, Mayr R, Bastiaens PI, Knop M 2007. Spatial regulation of Fus3 MAP kinase activity through a reaction-diffusion mechanism in yeast pheromone signalling. *Nature cell biology* 9(11)**:** 1319-1326

Magde D, Elson E, Webb WW 1972. Thermodynamic Fluctuations in a Reacting System-Measurement by Fluorescence Correlation Spectroscopy. *Phys Rev Lett* 29(11)**:** 705-708

Magde D, Webb WW, Elson EL 1978. Fluorescence correlation spectroscopy. III. Uniform translation and laminar flow. *Biopolymers* 17(2)**:** 361-376

Malone MH, Sciaky N, Stalheim L, Hahn KM, Linney E, Johnson GL 2007. Laser-scanning velocimetry: a confocal microscopy method for quantitative measurement of cardiovascular performance in zebrafish embryos and larvae. *BMC Biotechnol* 7**:** 40

Manz B, Stilbs P, Joensson B, Soederman O, Callaghan P, Srivastava A, Singh S, Krishnamoorthy G, Etheridge H, Averitt R 1995. NMR imaging of the time evolution of electroosmotic flow in a capillary. *Journal of Physical Chemistry* 99**:** 11297-11297

Masters SB, Landis CA, Bourne HR 1990. Mutational analysis of the structure and function of GTP-binding proteins. *Advances in enzyme regulation* 30**:** 75-87

Mateer SC, McDaniel AE, Nicolas V, Habermacher GM, Lin MJ, Cromer DA, King ME, Bloom GS 2002. The mechanism for regulation of the F-actin binding activity of IQGAP1 by calcium/calmodulin. *The Journal of biological chemistry* 277(14)**:** 12324-12333

Matz MV, Fradkov AF, Labas YA, Savitsky AP, Zaraisky AG, Markelov ML, Lukyanov SA 1999. Fluorescent proteins from nonbioluminescent Anthozoa species. *Nat Biotechnol* 17(10)**:** 969-973

Medina MA, Schwille P 2002. Fluorescence correlation spectroscopy for the detection and study of single molecules in biology. *Bioessays* 24(8)**:** 758-764

Meglinski IV, Matcher SJ 2002. Quantitative assessment of skin layers absorption and skin reflectance spectra simulation in the visible and near-infrared spectral regions. *Physiol Meas* 23(4)**:** 741-753

Meseth U, Wohland T, Rigler R, Vogel H 1999. Resolution of fluorescence correlation measurements. *Biophysical journal* 76(3)**:** 1619-1631

Milon S, Hovius R, Vogel H, Wohland T 2003. Factors influencing fluorescence correlation spectroscopy measurements on membranes: simulations and experiments. *Chemical Physics* 288**:** 171-186

Mooney D, Hansen L, Vacanti J, Langer R, Farmer S, Ingber D 1992. Switching from differentiation to growth in hepatocytes: control by extracellular matrix. *Journal of cellular physiology* 151(3)**:** 497-505

Mourant JR, Canpolat M, Brocker C, Esponda-Ramos O, Johnson TM, Matanock A, Stetter K, Freyer JP 2000. Light scattering from cells: the contribution of the nucleus and the effects of proliferative status. *J Biomed Opt* 5(2)**:** 131-137

Mourant JR, Freyer JP, Hielscher AH, Eick AA, Shen D, Johnson TM 1998. Mechanisms of light scattering from biological cells relevant to noninvasive optical-tissue diagnostics. *Appl Opt* 37(16)**:** 3586-3593

Murray J (1993) *Mathematical Biology*, Vol. 19, Heidelberg, Germany: Springer.

Muto H, Nagao I, Demura T, Fukuda H, Kinjo M, Yamamoto KT 2006. Fluorescence cross-correlation analyses of the molecular interaction between an Aux/IAA protein, MSG2/IAA19, and protein-protein interaction domains of auxin response factors of arabidopsis expressed in HeLa cells. *Plant & cell physiology* 47(8)**:** 1095-1101

Mutze J, Petrasek Z, Schwille P 2007. Independence of Maximum Single Molecule Fluorescence Count Rate on the Temporal and Spectral Laser Pulse Width in Two-Photon FCS. *J Fluoresc*

Nagao I, Aoki Y, Tanaka M, Kinjo M 2008. Analysis of the molecular dynamics of medaka nuage proteins by fluorescence correlation spectroscopy and fluorescence recovery after photobleaching. *The FEBS journal* 275(2)**:** 341-349

Nasevicius A, Ekker SC 2000. Effective targeted gene 'knockdown' in zebrafish. *Nat Genet* 26(2)**:** 216-220

Ormo M, Cubitt AB, Kallio K, Gross LA, Tsien RY, Remington SJ 1996. Crystal structure of the Aequorea victoria green fluorescent protein. *Science* 273(5280)**:** 1392-1395

Owen D, Campbell LJ, Littlefield K, Evetts KA, Li Z, Sacks DB, Lowe PN, Mott HR 2008. The IQGAP1-Rac1 and IQGAP1-Cdc42 interactions: interfaces differ between the complexes. *The Journal of biological chemistry* 283(3)**:** 1692-1704

Pack C, Saito K, Tamura M, Kinjo M 2006. Microenvironment and effect of energy depletion in the nucleus analyzed by mobility of multiple oligomeric EGFPs. *Biophysical journal* 91(10)**:** 3921-3936

Pan X, Foo W, Lim W, Fok MH, Liu P, Yu H, Maruyama I, Wohland T 2007a. Multifunctional fluorescence correlation microscope for intracellular and microfluidic measurements. *The Review of scientific instruments* 78(5)**:** 053711

Pan X, Shi X, Korzh V, Yu H, Wohland T 2009. Line scan fluorescence correlation spectroscopy for three-dimensional microfluidic flow velocity measurements. *Journal of biomedical optics* 14(2)**:** 024049

Pan X, Yu H, Shi X, Korzh V, Wohland T 2007b. Characterization of flow direction in microchannels and zebrafish blood vessels by scanning fluorescence correlation spectroscopy. *J Biomed Opt* 12(1)**:** 014034

Partikian A, Olveczky B, Swaminathan R, Li Y, Verkman AS 1998. Rapid diffusion of green fluorescent protein in the mitochondrial matrix. *J Cell Biol* 140(4)**:** 821-829

Percherancier Y, Berchiche YA, Slight I, Volkmer-Engert R, Tamamura H, Fujii N, Bouvier M, Heveker N 2005. Bioluminescence resonance energy transfer reveals ligand-induced conformational changes in CXCR4 homo- and heterodimers. *The Journal of biological chemistry* 280(11)**:** 9895-9903

Pereira DA, Williams JA 2007. Origin and evolution of high throughput screening. *Br J Pharmacol* 152(1)**:** 53-61

Petrasek Z, Hoege C, Hyman A, Schwille P 2008. Two-photon fluorescence imaging and correlation analysis applied to protein dynamics in C. elegans embryo. *Proceedings of SPIE* 6860**:** 68601L

Petrasek Z, Schwille P 2008a. Photobleaching in two-photon scanning fluorescence correlation spectroscopy. *Chemphyschem* 9(1)**:** 147-158

Petrasek Z, Schwille P 2008b. Precise measurement of diffusion coefficients using scanning fluorescence correlation spectroscopy. *Biophysical journal* 94(4)**:** 1437-1448

Phair RD, Misteli T 2000. High mobility of proteins in the mammalian cell nucleus. *Nature* 404(6778)**:** 604-609

Politz JC, Tuft RA, Pederson T 2003. Diffusion-based transport of nascent ribosomes in the nucleus. *Mol Biol Cell* 14(12)**:** 4805-4812

Pyati UJ, Look AT, Hammerschmidt M 2007. Zebrafish as a powerful vertebrate model system for in vivo studies of cell death. *Seminars in cancer biology* 17(2)**:** 154-165

Raghunath J, Rollo J, Sales KM, Butler PE, Seifalian AM 2007. Biomaterials and scaffold design: key to tissue-engineering cartilage. *Biotechnology and applied biochemistry* 46(Pt 2)**:** 73-84

Rao R, Langoju R, Gosch M, Rigler P, Serov A, Lasser T 2006. Stochastic Approach to Data Analysis in Fluorescence Correlation Spectroscopy. *J Phys Chem A Mol Spectrosc Kinet Environ Gen Theory* 110(37)**:** 10674-10682

Rauer B, Neumann E, Widengren J, Rigler R 1996. Fluorescence correlation spectrometry of the interaction kinetics of tetramethylrhodamin alpha-bungarotoxin with Torpedo californica acetylcholine receptor. *Biophysical chemistry* 58(1-2)**:** 3-12

Ries J, Schwille P 2008. New concepts for fluorescence correlation spectroscopy on membranes. *Phys Chem Chem Phys* 10(24)**:** 3487-3497

Ries J, Yu SR, Burkhardt M, Brand M, Schwille P 2009. Modular scanning FCS quantifies receptor-ligand interactions in living multicellular organisms. *Nature methods*

Rigler R, Mets, Widengren J, Kask P 1993a. Fluorescence correlation spectroscopy with high count rate and low background: analysis of translational diffusion. *Eur Biophys J* 22(3)**:** 169-175

Rigler R, Mets U, Widengren J, Kask P 1993b. Fluorescence correlation spectroscopy with high count rate and low background: analysis of translational diffusion. *Eur Biophys J* 22(3)**:** 169-175

Rika J, Binkert T 1989. Direct measurement of a distinct correlation function by fluorescence cross correlation. *Phys Rev A* 39(5)**:** 2646-2652

Rossman KL, Der CJ, Sondek J 2005. GEF means go: turning on RHO GTPases with guanine nucleotide-exchange factors. *Nat Rev Mol Cell Biol* 6(2)**:** 167-180

Ruttinger S, Buschmann V, Kramer B, Erdmann R, Macdonald R, Koberling F 2008. Comparison and accuracy of methods to determine the confocal volume for quantitative fluorescence correlation spectroscopy. *Journal of microscopy* 232(2)**:** 343-352

Saito K, Wada I, Tamura M, Kinjo M 2004. Direct detection of caspase-3 activation in single live cells by cross-correlation analysis. *Biochemical and biophysical research communications* 324(2)**:** 849-854

Saleh BEA, Teich MC (1991) *Fundamentals of photonics*, New York: Wiley-Interscience.

Santiago J, Wereley S, Meinhart C, Beebe D, Adrian R 1998. A particle image velocimetry system for microfluidics. *Experiments in Fluids* 25(4)**:** 316-319

Saxton M 2002. Chemically limited reactions on a percolation cluster. *The Journal of Chemical Physics* 116**:** 203

Schaaf MJ, Koopmans WJ, Meckel T, van Noort J, Snaar-Jagalska BE, Schmidt TS, Spaink HP 2009. Single-molecule microscopy reveals membrane microdomain organization of cells in a living vertebrate. *Biophysical journal* 97(4)**:** 1206-1214

Schatzel K, Drewel M, Stimac S 1988. Photon Correlation Measurements at Large Lag Times: Improving Statistical Accuracy. *J Mod Opt* 35(4)**:** 711-718

Schwille P 2001. Fluorescence correlation spectroscopy and its potential for intracellular applications. *Cell biochemistry and biophysics* 34(3)**:** 383-408

Schwille P, Haupts U, Maiti S, Webb WW 1999a. Molecular dynamics in living cells observed by fluorescence correlation spectroscopy with one- and two-photon excitation. *Biophysical journal* 77(4)**:** 2251-2265

Schwille P, Korlach J, Webb WW 1999b. Fluorescence correlation spectroscopy with single-molecule sensitivity on cell and model membranes. *Cytometry* 36(3)**:** 176-182

Schwille P, Kummer S, Heikal AA, Moerner WE, Webb WW 2000. Fluorescence correlation spectroscopy reveals fast optical excitation-driven intramolecular dynamics of yellow fluorescent proteins. *Proceedings of the National Academy of Sciences of the United States of America* 97(1)**:** 151-156

Schwille P, Meyer-Almes FJ, Rigler R 1997. Dual-color fluorescence cross-correlation spectroscopy for multicomponent diffusional analysis in solution. *Biophysical journal* 72(4)**:** 1878-1886

Seksek O, Biwersi J, Verkman AS 1997. Translational diffusion of macromolecule-sized solutes in cytoplasm and nucleus. *The Journal of cell biology* 138(1)**:** 131-142

Shaner NC, Campbell RE, Steinbach PA, Giepmans BN, Palmer AE, Tsien RY 2004. Improved monomeric red, orange and yellow fluorescent proteins derived from Discosoma sp. red fluorescent protein. *Nature biotechnology* 22(12)**:** 1567-1572

Shcherbo D, Merzlyak EM, Chepurnykh TV, Fradkov AF, Ermakova GV, Solovieva EA, Lukyanov KA, Bogdanova EA, Zaraisky AG, Lukyanov S, Chudakov DM 2007. Bright far-red fluorescent protein for whole-body imaging. *Nature methods* 4(9)**:** 741-746

Shimomura O, Johnson FH, Saiga Y 1962. Extraction, purification and properties of aequorin, a bioluminescent protein from the luminous hydromedusan, Aequorea. *J Cell Comp Physiol* 59**:** 223-239

Shin JT, Fishman MC 2002. From Zebrafish to human: modular medical models. *Annual review of genomics and human genetics* 3**:** 311-340

Sisan DR, Arevalo R, Graves C, McAllister R, Urbach JS 2006. Spatially resolved fluorescence correlation spectroscopy using a spinning disk confocal microscope. *Biophysical journal* 91(11)**:** 4241-4252

Skakun VV, Hink MA, Digris AV, Engel R, Novikov EG, Apanasovich VV, Visser AJ 2005. Global analysis of fluorescence fluctuation data. *Eur Biophys J* 34(4)**:** 323-334

Slaughter BD, Schwartz JW, Li R 2007. Mapping dynamic protein interactions in MAP kinase signaling using live-cell fluorescence fluctuation spectroscopy and imaging. *Proc Natl Acad Sci USA* 104(51)**:** 20320-20325

Stoll D, Templin MF, Bachmann J, Joos TO 2005. Protein microarrays: applications and future challenges. *Curr Opin Drug Discov Devel* 8(2)**:** 239-252

Storrie B, Nilsson T 2002. The Golgi apparatus: balancing new with old. *Traffic* 3(8)**:** 521-529

Strahle U, Korzh V (2004) Development of the primary nervous system of the zebrafish embryo. In *Molecular Aspects of Fish and Marine Biology, v. 2, Fish Development and Genetics: zebrafish and medaka models*, Gong Z, Korzh V (eds), pp 185-215. Singapore: World Scientific

Streisinger G, Walker C, Dower N, Knauber D, Singer F 1981. Production of clones of homozygous diploid zebra fish (Brachydanio rerio). *Nature* 291(5813)**:** 293-296

Stuart GW, McMurray JV, Westerfield M 1988. Replication, integration and stable germ-line transmission of foreign sequences injected into early zebrafish embryos. *Development (Cambridge, England)* 103(2)**:** 403-412

Sudhaharan T, Liu P, Foo YH, Bu W, Lim KB, Wohland T, Ahmed S 2009. Determination of in vivo dissociation constant, Kd, of CDC42-effector complexes in live mammalian cells using single wavelength fluorescence cross-correlation spectroscopy(SW-FCCS). *The Journal of biological chemistry*

Svoboda K, Block SM 1994. Biological applications of optical forces. *Annu Rev Biophys Biomol Struct* 23**:** 247-285

Swaminathan R, Hoang CP, Verkman AS 1997. Photobleaching recovery and anisotropy decay of green fluorescent protein GFP-S65T in solution and cells: cytoplasmic viscosity probed by green fluorescent protein translational and rotational diffusion. *Biophysical journal* 72(4)**:** 1900-1907

Swart-Mataraza JM, Li Z, Sacks DB 2002. IQGAP1 is a component of Cdc42 signaling to the cytoskeleton. *The Journal of biological chemistry* 277(27)**:** 24753-24763

Teh C, Chong SW, Korzh V 2003. DNA delivery into anterior neural tube of zebrafish embryos by electroporation. *BioTechniques* 35(5)**:** 950-954

Terry BR, Matthews EK, Haseloff J 1995. Molecular characterisation of recombinant green fluorescent protein by fluorescence correlation microscopy. *Biochemical and biophysical research communications* 217(1)**:** 21-27

Thompson NL (1991) Fluorescence Correlation Spectroscopy In *Topics in Fluorescence Spectroscopy Vol 1: Techniques*, J.R. L (ed), Vol. 1, pp 337-378. New York: Plenum Press

Thompson NL, Lieto AM, Allen NW 2002. Recent advances in fluorescence correlation spectroscopy. *Current opinion in structural biology* 12(5)**:** 634-641

Tseng Y, Kole TP, Wirtz D 2002. Micromechanical mapping of live cells by multiple-particle-tracking microrheology. *Biophysical journal* 83(6)**:** 3162-3176

Tsien RY 1998. the Green Fluorescent Protein. *Annu Rev Biochem* 67**:** 509-544

Van Craenenbroeck E, Engelborghs Y 1999. Quantitative characterization of the binding of fluorescently labeled colchicine to tubulin in vitro using fluorescence correlation spectroscopy. *Biochemistry* 38(16)**:** 5082-5088

Wachsmuth M, Waldeck W, Langowski J 2000. Anomalous diffusion of fluorescent probes inside living cell nuclei investigated by spatially-resolved fluorescence correlation spectroscopy. *Journal of molecular biology* 298(4)**:** 677-689

Watanabe T, Wang S, Noritake J, Sato K, Fukata M, Takefuji M, Nakagawa M, Izumi N, Akiyama T, Kaibuchi K 2004. Interaction with IQGAP1 links APC to Rac1, Cdc42, and actin filaments during cell polarization and migration. *Dev Cell* 7(6)**:** 871-883

Weaver VM, Petersen OW, Wang F, Larabell CA, Briand P, Damsky C, Bissell MJ 1997. Reversion of the malignant phenotype of human breast cells in three-dimensional culture and in vivo by integrin blocking antibodies. *J Cell Biol* 137(1)**:** 231-245

Weidemann T, Wachsmuth M, Tewes M, Rippe K, Langowski J 2002. Analysis of Ligand Binding by Two-Colour Fluorescence Cross-Correlation Spectroscopy. *Single Molecules* 3(1)**:** 49-61

Weiss M 2003. Stabilizing Turing patterns with subdiffusion in systems with low particle numbers. *Phys Rev E Stat Nonlin Soft Matter Phys* 68(3 Pt 2)**:** 036213

Weiss M 2007. Probing the interior of living cells with fluorescence correlation spectroscopy. *Ann N Y Acad Sci*

Weiss M, Elsner M, Kartberg F, Nilsson T 2004. Anomalous subdiffusion is a measure for cytoplasmic crowding in living cells. *Biophysical journal* 87(5)**:** 3518-3524

Westerfield M (2000) *The Zebrafish Book. A Guide for the Laboratory Use of Zebrafish (Danio Rerio)*, 4th edn. Eugene: Univ. of Oregon Press.

Widengren J, Mets U, Rigler R 1995. Fluorescence correlation spectroscopy of triplet states in solution: a theoretical and experimental study. *J Phys Chem* 99(36)**:** 13368-13379

Widengren J, Rigler R 1995. Fluorescence Correlation Spectroscopy of Triplet States in Solution: A Theoretical and Experimental Study. *J Phy Chem* 99**:** 13368-13379

Widengren J, Rigler R 1998. Fluorescence correlation spectroscopy as a tool to investigate chemical reactions in solutions and on cell surfaces. *Cellular and molecular biology (Noisy-le-Grand, France)* 44(5)**:** 857-879

Widengren J, Rigler R, Mets 1994. Triplet-state monitoring by fluorescence correlation spectroscopy. *J Fluoresc* 4(3)**:** 255-258

Widengren J, Schwilles P 2000. Characterization of photoinduced isomerization and back-isomerization of the cyanine dye Cy5 by fluorescence correlation spectroscopy. *J Phys Chem A* 104(27)**:** 6416-6428

Wohland T, Friedrich K, Hovius R, Vogel H 1999. Study of ligand-receptor interactions by fluorescence correlation spectroscopy with different fluorophores: evidence that the homopentameric 5-hydroxytryptamine type 3As receptor binds only one ligand. *Biochemistry* 38(27)**:** 8671-8681

Wohland T, Rigler R, Vogel H 2001. The standard deviation in fluorescence correlation spectroscopy. *Biophysical journal* 80(6)**:** 2987-2999

Wruss J, Runzler D, Steiger C, Chiba P, Kohler G, Blaas D 2007. Attachment of VLDL receptors to an icosahedral virus along the 5-fold symmetry axis: multiple binding modes evidenced by fluorescence correlation spectroscopy. *Biochemistry* 46(21)**:** 6331-6339

Wylie DC, Das J, Chakraborty AK 2007a. Sensitivity of T cells to antigen and antagonism emerges from differential regulation of the same molecular signaling module. *Proc Natl Acad Sci USA* 104(13)**:** 5533-5538

Wylie DC, Das J, Chakraborty AK 2007b. Sensitivity of T cells to antigen and antagonism emerges from differential regulation of the same molecular signaling module. *Proceedings of the National Academy of Sciences of the United States of America* 104(13)**:** 5533-5538

Xia NS, Luo WX, Zhang J, Xie XY, Yang HJ, Li SW, Chen M, Ng MH 2002. Bioluminescence of Aequorea macrodactyla, a common jellyfish species in the East China Sea. *Mar Biotechnol (NY)* 4(2)**:** 155-162

Yu J, Xiao J, Ren X, Lao K, Xie XS 2006. Probing gene expression in live cells, one protein molecule at a time. *Science* 311(5767)**:** 1600-1603

Yu L, Tan M, Hob B, Ding JL, Wohland T 2005. Determination of critical micelle concentrations and aggregation numbers by fluorescence correlation spectroscopy: Aggregation of a lipopolysaccharide. *Analytica Chimica Acta*(556)**:** 216-225

Yu SR, Burkhardt M, Nowak M, Ries J, Petrasek Z, Scholpp S, Schwille P, Brand M 2009. Fgf8 morphogen gradient forms by a source-sink mechanism with freely diffusing molecules. *Nature*

Zemanova L, Schenk A, Hunt N, Nienhaus GU, Heilker R 2004. Endothelin receptor in virus-like particles: ligand binding observed by fluorescence fluctuation spectroscopy. *Biochemistry* 43(28)**:** 9021-9028

Zhong TP 2005. Zebrafish genetics and formation of embryonic vasculature. *Curr Top Dev Biol* 71**:** 53-81

Zon LI, Peterson RT 2005. In vivo drug discovery in the zebrafish. *Nat Rev Drug Discov* 4(1)**:** 35-44